THE UNIVERSITY OF CHICAGO

FROM BASIC CONCEPTS TO EMERGING DEVICES: MERCURY TELLURIDE COLLOIDAL QUANTUM DOT INFRARED PHOTODIODES FOR 1 - 5 MICRONS DETECTION

A DISSERTATION SUBMITTED TO

THE FACULTY OF THE DIVISION OF THE PHYSICAL SCIENCES

IN CANDIDACY FOR THE DEGREE OF

DOCTOR OF PHILOSOPHY

DEPARTMENT OF CHEMISTRY

BY

MATTHEW MICHAEL ACKERMAN

CHICAGO, ILLINOIS

JUNE 2020

Table of Contents

List of Figures

List of Tables

Acknowledgements

I would like to thank my advisor, Professor Philippe Guyot-Sionnest, for his support and guidance during my graduate work. It is my great fortune to have had a mentor so accessible and open to discussion with great physical insight to guide me to the completion of this work. For this, I am immensely grateful. I would like to thank and acknowledge my colleague, Dr. Xin Tang, whose microfabrication expertise and endless creativity elevated this work beyond what I could have expected. It was Xin's vision that helped turn a scientific breakthrough into an awe-inspiring technology. I would like to thank Dr. Justin Jureller and Dr. Qiti Guo for their training and support on the necessary instrumentation that is made available by the Materials Research Science and Engineering Center with support by the National Science Foundation. I would like to thank Dr. Alexander Filatov for his contributions at the X-ray research facilities and discussion of results. I would like to thank Dr. Wook Jun Nam, manager of the Searle Cleanroom and Nanofabrication facility, for providing trainings and resources for device fabrication. I would like to thank Dr. Edward Malochovsky, Dr. Yuval Yifat, Dr. Guohua Shen, and Dr. Sean Keuleyan for their discussions early on and throughout the course of this work. I am grateful to the members of the Guyot-Sionnest lab, Menglu Chen, Chris Melnychuk, Ananth Kamath, Haozhi Zhang, for excellent weekly discussions and challenging questions that forced me to improve my comprehension of this field of work. Finally, I would like to thank my friends and family for their unending support and encouragement throughout the duration of my graduate experience.

Abstract

HgTe colloidal quantum dots (CQDs) are an emerging technology important for the development of low-cost, next-generation infrared technologies. However, photodetectors based on HgTe CQDs must also be capable of delivering performances equivalent to or better than the epitaxial technologies to compete commercially. Here, concepts and methods are described for designing emerging HgTe CQD photodiodes with detection in the shortwave and mid-wave infrared spectral regions and figures-of-merit rapidly approaching the commercial epitaxial technologies. The concepts investigated for the design of HgTe CQD photodiodes included heterojunction diodes with charge-selective transport layers and homojunction diodes with thin films of doped HgTe CQDs. The former likely suffer from unfavorable heterojunction band alignment that is detrimental to device operation and challenging to control in narrow-gap CQDs. Doping thin films of HgTe CQDs, however, is successful, following the introduction of a solid-state cation exchange process. Heterojunctions of HgTe CQDs and doped semiconductor nanoparticles were also essential to the concept and design of inverted-polarity HgTe CQD photodiodes. Finally, the designs developed within this work culminate in the demonstration of a SWIR/MWIR dual-band infrared photodetector. Further developments of the HgTe CQD photodiodes will follow from addressing design and material challenges for enhancing the charge collection efficiency, absorption, and operating temperature of these photodiodes. Today, the shortwave infrared HgTe CQD photodiodes demonstrate the most promise, and mid-wave HgTe CQD detectors with high temperature operation are under development. The designs here may also extend to the HgTe CQDs with absorption in the long-wave infrared and position HgTe CQDs as an emerging technology for the future of infrared detectors.

Chapter 1 Introduction

This chapter introduces concepts relevant to the discussion of HgTe colloidal quantum dot infrared photodiodes. The concepts in the following sections include infrared photodetection, HgTe colloidal quantum dots, types of photodetectors, and characteristics for describing the performance of a photodetector.

1.1 Infrared Detection and Imaging

The infrared spectrum is from 1 μm, beyond the detection of silicon, up to 14 μm. This spectral range is practically divided into three spectral regions carved out by the transparency of Earth's atmosphere, which are the short-wave infrared from 1-2.5 μm, mid-wave infrared from 3-5 μm, and long-wave infrared from 8-14 μm. Fig. 1-1 shows the infrared transparency of Earth's atmosphere with windows of transparency that define each of these spectral ranges. The classification of infrared technologies is defined by their absorption in each of these specific spectral regions.

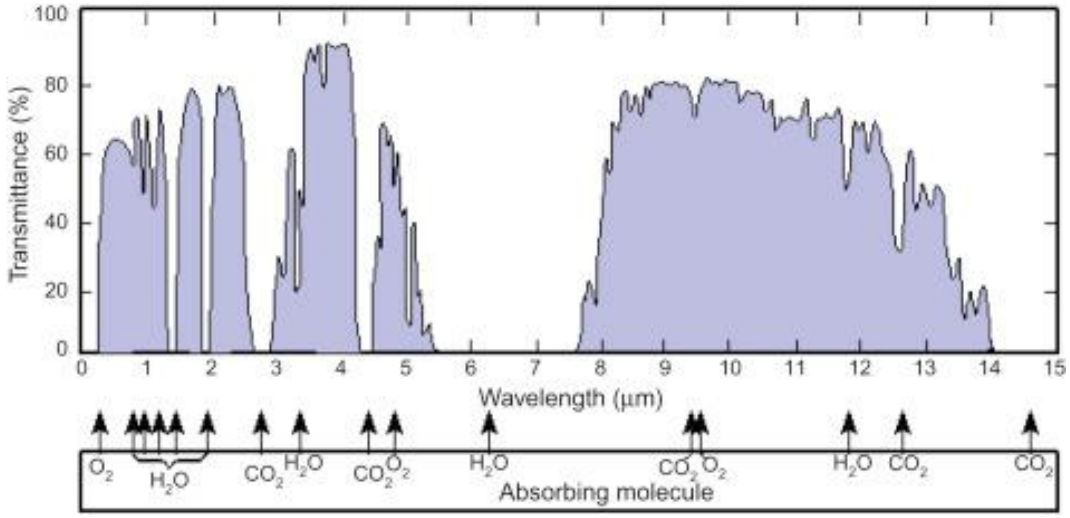

Figure 1-1 *Atmospheric transparency in the infrared spectrum.*

Historically, the development of infrared photodetectors and imaging capabilities has been driven by astronomy and defense applications. Semiconductors were first used for infrared photodetection following the discovery of the thallium sulfide, Tl_2S,[1,2] and lead sulfide, PbS, photoconductors just before the start of World War II.[3] In 1959, the ternary alloy HgCdTe was discovered with a tunable infrared absorption from 0.8 μm up to 13 μm and was demonstrated for use as an infrared photodetector.[4] Naturally, for the advantage of night vision and long-range detection, the military adopted infrared technology and significantly advanced its development for imaging capabilities. Three decades worth of research on HgCdTe[5,6] have made it one of the most advantageous semiconductor alloys for infrared photodetection and imaging for its spectral range up to 15 μm and state-of-the-art performance.[7]

As early as the 1960s, development on III-V semiconductor alloys such as InSb[8] was started. In the 1980s, germanium would be replaced with epitaxially grown InGaAs for short-wave infrared detection.[9–11] More recently, the type-II strained layer superlattice has also been adopted by the industry for its compatibility with existing III-V processing infrastructure and spectral tunability in the mid-wave and long-wave infrared spectral regions compared to traditional III-V semiconductor alloys.[12]

While developments in infrared technology are primarily directed by military interests,[13] there is an increasing understanding that such technologies can provide useful information to the commercial sector. Affordable long-wave infrared cameras are on the market today and developments in the short-wave infrared are following suit.[14] With increasing automation and advancements in machine vision and image processing capabilities, the potential for infrared

photodetection and imaging to solve problems in product evaluation, surveillance, and medical diagnosis is gaining recognition.[5,6,15–17]

Still, factors such as low-temperature operation and limitations on epitaxial manufacturing lead to significant size, weight, power and cost requirements that restrict the commercial viability of infrared technologies. Therefore, several low-dimensional materials have emerged in the last decade including quantum dots,[18,19] nanowires,[20] and 2D semiconductors[21] in an effort to address these challenges. Among them, HgTe colloidal quantum dots provide unique advantages and will be the focus of this thesis.

1.2 Colloidal quantum dots for infrared photodetection

Colloidal quantum dots are solution-processed, quantum-confined semiconductor nanocrystals where the spatial confinement of the charge carrier results in discrete, allowed energy levels that define the optical transitions for the absorption and emission of light.[22] Due to their small size, colloidal quantum dots have a large surface-to-volume ratio and, consequently, the surface chemistry dictates many of the properties. Dangling bonds due to un-passivated atoms on the surface can lead to charge carrier trapping and photoluminescence quenching. Variations in the dipole moment of the surface ligands can shift the colloidal quantum dot energy levels as much as 1 eV with respect to vacuum, and the surface stoichiometry will determine the doping nature of the colloidal quantum dot. Therefore, careful control of the colloidal quantum dot growth and processing is required to obtain the desirable optical and electrical properties. The most commonly utilized technique for the synthesis of colloidal quantum dots is the hot-injection method where the shape and size of the colloidal quantum dots depend on temperature, reaction time, reagent

reactivity, and the ligand/solvent environment. The liquid nature of the colloidal quantum dots is an advantage that enables solution processing capabilities for the production of semiconductor technologies including photodetectors, flexible electronics, and next generation solar cells.[23]

Colloidal quantum dots based on lead (Pb) chalcogenides and mercury (Hg) chalcogenides are well-suited for infrared photodetection. In the bulk, PbS, PbSe, and PbTe have band gap energies of 0.41, 0.27, and 0.31 eV, respectively.[24] PbS and PbSe colloidal quantum dots have been most widely developed for near-infrared photovoltaics and short-wave infrared sensing with limits on the detection range set by the bulk band gap. The opportunity for low-cost near- and short-wave infrared detection afforded by Pb chalcogenide colloidal quantum dots has spurred commercial development efforts.

Full coverage of the infrared spectrum requires the quantum confinement of a zero-band gap semimetal such as HgSe and HgTe.[25] In the case of HgTe, the optically tunable absorption extends from 1 μm up to 12 μm and beyond into the terahertz.[26–28] In addition to the practical advantage of low-cost solution processes, HgTe colloidal quantum dots were shown to have lower Auger coefficients than the bulk semiconductor alloy HgCdTe;[29] this means that HgTe colloidal quantum dot-based detectors would, in principle, operate at higher temperatures than existing bulk semiconductors for infrared detection and reduce the prohibitive cooling requirements. With broad infrared spectral tunability, low-cost production, and the potential for higher temperature operation, HgTe colloidal quantum dots have the potential to address the challenges of size, weight, power, and cost that prohibit the proliferation of infrared technologies into the commercial market.

1.3 Types of Photodetectors

A variety of photodetector geometries have been developed for the detection of light including photoconductors, photodiodes, and phototransistors. Variations of the photoconductor and photodiode geometries are most widely available and used for photodetection. Therefore, a basic description of the photoconductor and the operating principle of the photodiode is presented here with emphasis on relevant characteristics for the discussion in the following chapters. A more thorough discussion of photodetectors can be found in semiconductor physics texts such as *Physics of Semiconductor Devices* by S. M. Sze.

1.3.1 Photoconductor

The photoconductor is the simplest photodetector concept, consisting of an absorber semiconductor placed laterally between two electrodes under an external bias. As incident radiation is absorbed, the conductance changes due to the increase in photogenerated free carriers that are transported under the influence of the external bias. The response of a photoconductor to incident radiation can be increased by either increasing the absorption of light or increasing the bias on the conductor. The current in a conductor under bias is due to drift of the mobile charge carriers induced by the electric field, and therefore increases proportional to the field strength. The transit time of the charge carrier across the conductor also decreases under strong electric fields and can become much shorter than the charge carrier lifetime. For sufficiently short transit times, the charge carrier "makes many trips" across the conductor before recombining, thus enhancing the signal of the detector by a multiplicative factor. This effect is referred to as photoconductive gain, G, in a conductor and expressed by the ratio of the lifetime to the transit time that depends on the applied bias. The effect of photoconductive gain applies to both the light and dark currents

of the photoconductor and, therefore, simply increasing *G* in a photoconductor will not improve the signal to noise of a photoconductive detector.

To maximize the sensitivity of a photoconductor, the semiconductor absorber should be intrinsic to keep the dark conductance low. However, for narrow band gap semiconductors, even an intrinsic semiconductor will suffer from thermally generated free carriers and cooling the detector to lower operating temperatures is required to enhance the detector sensitivity. The noise in a photoconductor is due to shot noise, Johnson noise, and *1/f* noise. Johnson noise is a random noise due to the fluctuations in the thermal motion of the charge carriers and, therefore, present in any conductor. The shot noise is due to the quantized nature of light and charge where the random variations between the arrival of photons at the absorber or electrons at the electrode over a given interval of time determines the temporal fluctuation in the current density. For any device with a DC bias, the *1/f* noise phenomenon[30] will be present and limit the sensitivity, especially at low frequency operation. The advantage of the photodiode, discussed next, over the photoconductor is that an external bias is not required and, therefore, the *1/f* noise can be eliminated.

1.3.2 Photodiode

Different types of photodiodes include the metal-semiconductor (or Schottky junction) diode, p-n homojunction, p-i-n homojunction, and analogous doped semiconductor heterojunction diodes. In contrast with photoconductors, photodiodes are designed with an internal potential that drives the separation and transport of photogenerated carriers, which results in an external voltage or current. The magnitude of this internal, or built-in, potential is dependent upon the difference in the work functions, or doping densities, of the materials that make up the photodiode junction.

At thermal equilibrium, majority charge carriers from each material will diffuse toward the junction and recombine, leaving behind exposed charged donor and acceptor dopant atoms that contribute to the magnitude of the internal electric field. This region of unscreened charged dopants, known as the space-charge region or depletion region, grows until the internal electric field can sufficiently oppose the diffusion current and prevent further recombination of majority carriers.

The width of the depletion region depends on the doping of the semiconductor regions as expressed in Eq. (1.1) for a pn-homojunction diode where the depletion width is inversely proportional to the semiconductor dopant density.

$$W = \sqrt{\frac{2\epsilon\epsilon_0}{q}\left(\frac{n+p}{np}\right)(V_{bi} - V_{ext})} \tag{1.1}$$

Here, W is the depletion region width, ϵ is the dielectric constant of the semiconductor, ϵ_0 is the vacuum permittivity constant, q is the elementary charge, n is the electron majority carrier density in the n-type semiconductor, p is the hole majority carrier density in the p-type region, V_{bi} is the built-in potential, and V_{ext} is the external applied potential that is negative for reverse bias operation and positive for forward bias operation. Reverse bias refers to the application of an external potential with (+)V applied to the cathode while forward biasing refers to a (+)V applied to the anode.

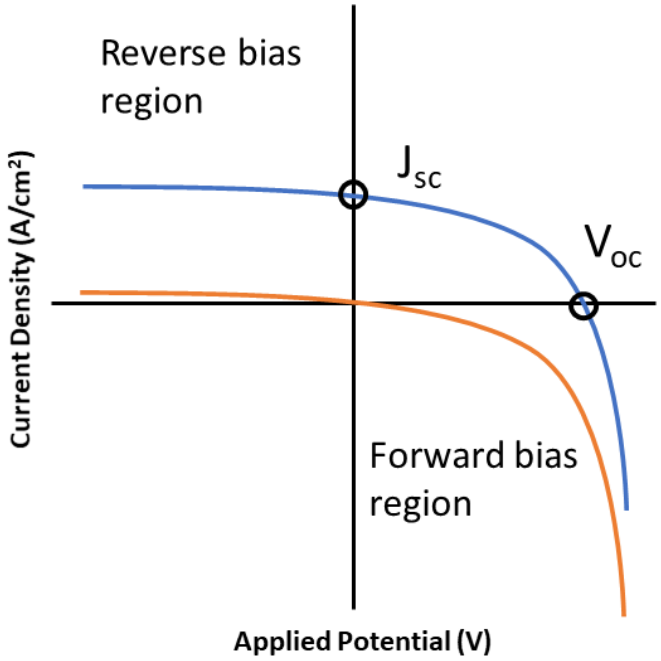

Figure 1-2 *Current density-voltage (JV) behavior of a photodiode with representative curves for the dark current (orange) and photocurrent (blue) densities.*

Operation under a reverse bias increases the depletion region width and further inhibits a current from passing through the diode. Therefore, as shown in Fig. 1-2, the reverse bias current is small and has a weak dependence on the applied potential. In forward bias operation, the external potential cancels the internal potential and the depletion region width goes to zero. Therefore, the current is no longer inhibited by the internal electric field and flows through the diode. The effect is apparent by the strong voltage dependence of the current as shown in the forward bias region of Fig. 1-2. Finally, operating the photodiode under short-circuit, *i.e.* at zero applied bias, is desirable to eliminate *1/f* noise and improve detector sensitivity. The short-circuit current density, J_{SC}, is measured and indicated by the point where the blue line crosses the y-axis in Fig. 1-2. A photodiode can be operated in either short-circuit mode, wherein no bias is applied, or under a

reverse bias. The application of a reverse bias increases the depletion width, photodetector speed, and collection efficiency but must be balanced with the bias dependence of the noise.

In addition to J_{SC}, a photodiode is also described with its open-circuit voltage, V_{OC}, which is the voltage on the photodiode when the current goes to zero and indicated by the point in Fig. 1-2 where the blue line crosses the x-axis. The band-gap dependent maximum of the open-circuit voltage has been derived by the Shockley-Quiesser limit for a pn-homojunction diode.[31] For a near infrared band gap of 1 eV down to a long-wave infrared band gap energy of 0.1 eV, the maximum open-circuit voltages at room temperature are ~800 meV and 50 meV, respectively. In practice, the value is often smaller than the maximum and limited by the non-radiative processes due to semiconductor defects, disorder, and fast energy transfer to the environment. Therefore, the measure of the Voc can be a useful metric for assessing the quality of the photodiode. Finally, the V_{OC} is only as large as the built-in potential and, therefore, depends on the doping of the semiconductor(s) in the junction.

The electric field across the depletion region rectifies the current through the diode, *i.e.* current flows only in the direction of the internal electric field. This is important for mitigating dark current and noise current that reduce the sensitivity of the photodiode detector. Generally, strongly rectifying photodiodes have a high shunt resistance; this is an important metric for the quality of the photodiode and proportional to the detector sensitivity discussed later. The shunt resistance, R_0 or R_{sh}, is expressed as in Eq. (1.2),

$$R_0 = \left(\frac{dI}{dV}\right)^{-1}|_{V=0} \tag{1.2}$$

and described as the slope of the current-voltage behavior evaluated at zero applied potential. The shunt resistance is the internal resistance of the photodiode and determines the thermal (Johnson) noise, which is typically the dominant noise source over shot noise in a photodiode. The product of R_0 and the area, referred to as the resistance-area product or R_0A, is a commonly used metric for comparing the sensitivities of different infrared detector technologies.

1.4 Characteristics of the infrared photodetector

The following characteristics allow the comparison of photodetectors based on HgTe CQDs with other emerging and commercially available materials for infrared detection. General characteristics such as the cut-off wavelength, operating temperature, response speed, and noise-equivalent power are defined. Figures-of-merit such as responsivity, quantum efficiency, and specific detectivity are also defined.

1.4.1 Cut-off wavelength and operating temperature

The cut-off wavelength is the longest wavelength at which the detector operates above a specified sensitivity. Therefore, the definition of the photodetector cut-off wavelength is somewhat arbitrary and should be specified accordingly. Here, the cut-off wavelength will be defined as that wavelength at which the detector responsivity falls below 50% of the peak responsivity. For comparing photodetector performance, it is important to compare only detectors of similar cutoff wavelengths that have been defined in the same way or to directly compare the responsivity spectra when available.

To improve the sensitivity, infrared photodetectors are operated at reduced temperatures to minimize the thermally generated noise. Semiconductors and their alloys exhibit a temperature-

dependent shift in the band gap and correspondingly their spectral absorption cut-off energy. Therefore, when reporting detector performances, the operating temperature should be clearly specified and equivalent when comparing figures-of-merit.

1.4.2 Responsivity and quantum efficiency

The first figure of merit for an infrared photodetector is the responsivity, which is defined as the photocurrent normalized to the incident power on the photodetector and expressed as in Eq. (1.3).

$$\mathcal{R} = \frac{i_{ph}}{P_{in}} \tag{1.3}$$

Here, i_{ph} is the photocurrent in amps and P_{in} is the power incident on the photodetector in Watts such that $\mathscr{R}$ has the unit A/W. For reporting photodetectors, the responsivity should be specified as either a blackbody responsivity with the temperature of the blackbody provided or a monochromatic responsivity with the specific wavelength indicated. Equally important as the responsivity is the quantum efficiency that relates the conversion efficiency of incident photons into photocurrent, which is related to $\mathscr{R}$ by Eq. (1.4).

$$EQE = \mathcal{R}_\lambda * \frac{hc}{\lambda} \tag{1.4}$$

Specifically, Eq. (1.4) refers to the external quantum efficiency (EQE) where h is Planck's constant, c is the speed of light, and λ is the wavelength of the incident radiation. The external quantum efficiency is the ratio of the total number of electrons collected against the total number of incident photons regardless of how much light is absorbed by the photodetector. Another

quantity called the internal quantum efficiency (IQE) refers to the total number of electrons collected against only the fraction of the incident photons absorbed by the photodetector. This is a useful quantity for expressing whether the efficiency of the photodetector is limited by carrier collection or photon absorption. Often in thin film photodetectors, the absorption is the limiting factor. For example, all of the photogenerated charge carriers could be collected and the IQE would be unity but the EQE may be less than 1 due to the low absorption in the thin film. In this situation, increasing the absorption using micro-lenses, optical nanostructures, or plasmonic structures can lead to higher EQE. When the absorption in the photodiode is unity, IQE is equivalent to EQE and the photodiode efficiency is limited by carrier collection and recombination in the photodiode.

1.4.3 Noise equivalent power and specific detectivity

Important for defining the sensitivity of the photodetector is the noise-equivalent power, *i.e.* the minimum power at which the photocurrent signal is equivalent to the noise limit of the photodiode and expressed in Eq. (1.5) where i_n is the noise current in amps.

$$NEP = \frac{i_n}{\mathcal{R}} \tag{1.5}$$

However, the photodetector performance also depends on the bandwidth of the integrated detector noise and the detector area specific to the configuration. Therefore, a normalized value called the specific detectivity, D^*, is the second figure of merit that allows for direct comparison of different detectors materials and geometries. D^* is expressed as in Eq. (1.6) and related to NEP,

$$D^* = \frac{\sqrt{A_d \Delta f}}{NEP} = \frac{\mathcal{R}\sqrt{A_d \Delta f}}{i_n} \tag{1.6}$$

where A_d is the detector area in cm^2, Δf is the noise equivalent bandwidth in Hz, and the units on D^* are $\sqrt{Hz}\ cm/W$, or Jones. The significance of D^* can be understood as the maximum signal-to-noise ratio for a photodetector of area 1 cm^2 and incident power of 1 W. When comparing and reporting the specific detectivity, the operating temperature and either the wavelength for a monochromatic source or the cutoff-wavelength for a blackbody source should be indicated.

1.4.4 Detector response speed

The detector response speed determines the high-frequency operating limit of the photodetector and the practical limitations for imaging applications. The carrier transit, trapping, and RC circuit time constants contribute to the response speed of the photodetector.[32]

$$\frac{1}{\tau_d} = \frac{1}{\tau_{transit}} + \frac{1}{\tau_{eff}} + \frac{1}{\tau_{RC}} \tag{1.7}$$

In Eq. (1.7), τ_d is the device response time, $\tau_{transit}$ is the time required for carriers to travel to the contacts, τ_{eff} is the effective lifetime of charge carriers accounting for radiative and non-radiative recombination lifetimes, and τ_{RC} is the circuit RC time constant. The τ_{eff} can become negligible for high-quality semiconductor materials, and for well-passivated colloidal quantum dots. The $\tau_{transit}$ is determined by the geometry of the photodetector. For photodiodes, this is generally between ns-µs due to the large built-in electric field and becomes faster as the device becomes fully depleted. The τ_{RC} is set by the resistance and capacitance in the circuit, often limited by the equivalent characteristic RC values for the photodetector. The slowest process limits the response speed of the photodetector and sets the frequency bandwidth for operation as in Eq. (1.8).

$$f = \frac{1}{2\tau_d} \tag{1.8}$$

The response speed of a photodetector is measured using a fast-pulsed laser, *i.e.* faster than the response speed of the detector. The rise time is reported as the time required for the signal to reach 67% of the peak response. One advantage of a semiconductor photodiode over other types of infrared photodetectors is that the response speed of the detector is generally much faster and enables high-speed and high frame rate imaging, important for both military and industrial applications.

1.5 Summary

Infrared photodetection and imaging has historically been a military and research technology, however applications for infrared are emerging in the commercial space. HgCdTe, InGaAs, InSb, and the type-II strained layer superlattice are epitaxially manufactured bulk semiconductors alloys used by the industry and in research today. Infrared photodetectors most commonly come as photoconductors or photodiodes where the latter have advantages of inherently lower noise and faster detector response speeds. The figures of merit for the infrared photodetectors are the responsivity and specific detectivity, which can be used to compare the performance of photodetectors based on different materials at specified wavelengths and operating temperatures. These figures of merit will be used throughout this text to compare colloidal quantum dot infrared photodetectors with traditional epitaxial-based photodetectors.

Colloidal quantum dots, specifically PbS and HgTe CQDs, are leading the development of solution-processed materials for infrared photodetection with their advantages of scalable solution processing and low-cost production. Colloidal quantum dots are still relatively new compared to

the many decades of research on epitaxial semiconductor alloys. The following chapters detail the development of the HgTe CQD photodiodes for short-wave and mid-wave infrared photodetection.

Chapter 2 Design and Fabrication of HgTe CQD Photodetectors

Designing narrow-gap HgTe colloidal quantum dot photodiodes is challenging because small changes in the surface chemistry of either the quantum dots or the junction material interfaces can lead to undesirable energy offsets and variations in the CQD doping level, both of which lead to unreliable and inferior photodetectors. This chapter describes the strategy to improve the quality of the HgTe colloidal quantum dot photodiodes as measured by their current rectifying behavior and figures-of-merit. Improving the rectification will lead to lower noise current densities and increased current collection efficiency. Therefore, designing strongly rectifying photodiodes leads to improvements in the figures-of-merit. The methods for realizing the goal of a strongly rectifying HgTe photodiode include using charge selective transport layers, forming a HgTe colloidal quantum dot pn-homojunction, and the use of extrinsic dopants to create a built-in potential. The latter method is reserved as the topic of Chapter 3 to follow. The former two of the three methods are discussed in this chapter, and the extent to which these methods failed or succeeded is detailed in each of the following sections.

2.1 Development of HgTe Colloidal Quantum Dot Photodetectors

The earliest work on HgTe colloidal quantum dots was an aqueous synthesis reported by Rogach *et al.* in 1999 for near-infrared HgTe CQDs.[33] In 2003, the photoconductive detection of infrared light up to 1.1 μm was demonstrated with thioglycerol-capped HgTe CQDs following the aqueous synthesis.[34] In 2006, Kim *et al.* demonstrated photoconductor detection up to 1.5 μm, of interest for telecommunications, with thioglycerol-capped HgTe CQDs.[35] Inspired by solar cell photovoltaic designs, Gunes *et al.* introduced a variation on nanoparticle-sensitized and polymer-nanoparticle blends with a HgTe colloidal quantum dot near-infrared absorbing HgTe CQDs-

sensitized TiO2, using a poly(3-hexathiophene), or P3HT, hole transport layer.[36] Boberl *et al.* then demonstrated detectivity as high as 3×10^{10} Jones at 1.5 μm and room temperature operation with an HgTe CQD photoconductor fabricated by inkjet printing.[37]

The photodetection was first extended up to 3 μm with a post-synthetic Oswald ripening process where the HgTe CQDs are transferred from an aqueous phase to an organic phase and heated.[38] In 2011, Keuleyan *et al.* used an inorganic Hg salt and a mixture of alcohol-pyridine to extend the HgTe CQD synthesis, demonstrating photoconductive detection of infrared light with response up to 5 μm.[39] In an extension of their work, Keuleyan *et al.* developed an all-organic synthesis of HgTe CQD by using a $HgCl_2$ salt in oleylamine and trioctylphosphine telluride (TOPTe) precursor with tunable infrared absorption beyond 10 μm and photodetection up to 12 μm.[27,40] In 2016, Buurma *et al.* fabricated a photoconductive mid-infrared focal plane array imager using HgTe colloidal quantum dots dropcast onto a commercial readout integrated circuit, which demonstrated the ease of processing colloidal quantum dots for infrared imaging applications.

A significant limitation of the photoconductive detector is the presence of *1/f* noise due to the DC-bias (as described in Chapter 1) that determines the noise limit and reduces the sensitivity for photodetection. Lhuillier *et al.* characterized the photoconductor behavior and showed that nanocrystal conductors were subject to low-frequency *1/f* noise that limits device sensitivity.[41] In addition to the *1/f* noise limit, the large surface-to-volume ratio of the mid infrared HgTe colloidal quantum dots means that the surface dictates the physical properties of the nanocrystal including doping density. Consequently, the doping of the nanocrystal is very sensitive to changes in the surface chemistry due to adsorption of water, oxygen, or other ambient species or contaminants

during processing. These changes in surface chemistry can dramatically shift the Fermi level, conduction, and valence band edge energies. In photoconductive devices, small changes in the doping can lead to significant changes in the conductivity and, therefore, the dark current density of the device. Deviations from an intrinsic nanocrystal film then result in larger noise and dark currents due to the increasing thermally generated carrier densities, thus imposing significant cooling requirements to eliminate these contributions to detector noise.

A photodiode has inherent advantages over a photoconductive detector. First, operation of a photodiode under short-circuit conditions, *i.e.* no applied DC bias, can mitigate the *1/f* noise and improve the sensitivity. In terms of doping, the photodiode is less sensitive to small changes during processing. At thermal equilibrium, the photodiode has a depletion region that is intrinsic and will largely determine the noise process of the photodiode. Generally, at high temperatures, a narrow gap semiconductor will be limited by space charge generation noise.[42] Here, this means that the photodiode, being nearly intrinsic in the space charge region, by design will have either less noise than photoconductors at the same operating temperature or an equivalent sensitivity but at higher operating temperatures.

To realize the advantages of the photodiode for HgTe CQDs sensing, Guyot-Sionnest and Roberts demonstrated a background-limited HgTe CQD photodiode operating at 90 K and zero applied bias for mid-wave infrared photodetection with an infrared spectral cutoff at 5 μm.[43] The work described in this section builds upon the photodiode introduced by Guyot-Sionnest and Roberts with the goal of improving the photodiode rectification and figures-of-merit, especially for operation near room temperature.

2.2 Carrier Transport and Blocking Layers

The charge transport layers (CTLs) act as buffers between the absorber and the electrodes, as shown in Fig. 2-1, to minimize deleterious effects such as charge carrier recombination at the electrode interfaces. An electron transport layer (ETL) is generally a wide-gap semiconductor or doped insulator that selectively transports electrons while blocking hole transport, therefore spatially separating the charge carriers away from the cathode. Similarly, a hole transport layer (HTL) selectively facilitates the collection of holes while blocking electrons and spatially separates charge carriers away from the anode. In this way, electron and hole transport layers reduce charge recombination events, which leads to improvements in the rectification and carrier collection efficiency of photodiodes. The alignment of the ETL and HTL energy levels to the semiconductor conduction and valence bands, respectively, is critical to the effectiveness of the transport layer.

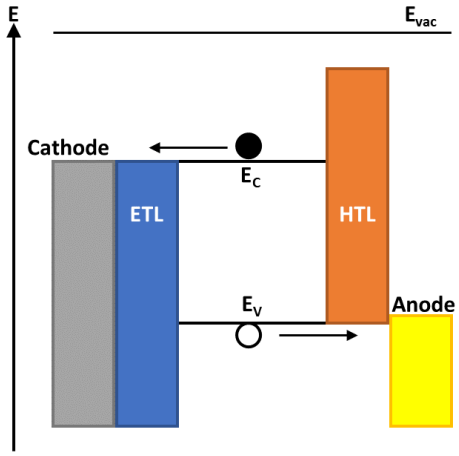

Figure 2-1 *Representative flat band energy diagram with respect to vacuum energy level (Evac) for a photodiode consisting of a cathode, an electron transport layer (ETL), semiconductor absorber with conduction band energy Ec and valence band energy Ev, a hole transport layer (HTL), and an anode.*

Practical requirements for electron and hole transport layers include good conductivity, matching to the desired charge carrier energy level, blocking the transport of the undesired charge carrier, and, for infrared photodetection, transparency to the infrared wavelengths of interest for detection. Additionally, it is required that these materials be processable at low temperatures to avoid damage to the CQD thin film as well as insensitive to moisture and oxygen to act as a passivating layer and ensure consistent device operation.

For narrow band gap HgTe CQDs, three complications make finding the right ETL and HTL particularly challenging. First, the high electron affinity of HgTe CQD conduction band level[25] immediately disqualifies many ETLs that typically have work functions and electron affinities much lower in energy. Second, many HTLs have relatively high ionization energies, much higher than the HgTe CQD valence level, that would introduce a large offset in energy and block hole transport. Third, the conduction and valence levels of CQDs can shift in energy as much as 1 eV due to the net dipole between the quantum dot surface and passivating ligands.[44] One direction for addressing these challenges is to fix the ligands on the HgTe CQDs and find ETLs and HTLs with energy levels appropriate for the design of a rectifying photodiode.

Here, various electron and hole transport materials are tested with the HgTe CQDs in a photodiode. The ligands in the HgTe CQD films are held constant by treatment with a mixture of ethanedithiol and hydrochloric acid, and the candidate transport layers with relevant energy levels are selected. The electrical behavior of the photodiode was characterized and correlated with the use of a given transport layer. A discussion of the effect on operation of the HgTe CQD photodiodes with each transport layer is given in the context of properties such as electron affinity,

work function, and mobility of each transport layer. Insights from the various materials and device architectures tested are summarized in section 2.2.5 below.

2.2.1 Work Function of Candidate Electron and Hole Transport Layers

The work function of a material, be it metal, insulator, or semiconductor, is the energy required to move an electron from the surface to vacuum. This is defined as the difference between the vacuum level, or energy of an electron at rest far from the material surface, and Fermi level of the material.[45] Fig. 2-2 defines useful terms for describing the energy levels of a metal, semiconductor, and insulator including the work function, φ, that is equivalent to the Fermi level energy, E_F; ionization energy, P, that is equivalent to the valence band energy, E_V; and electron affinity, χ, that is equivalent to the conduction band energy, E_C.

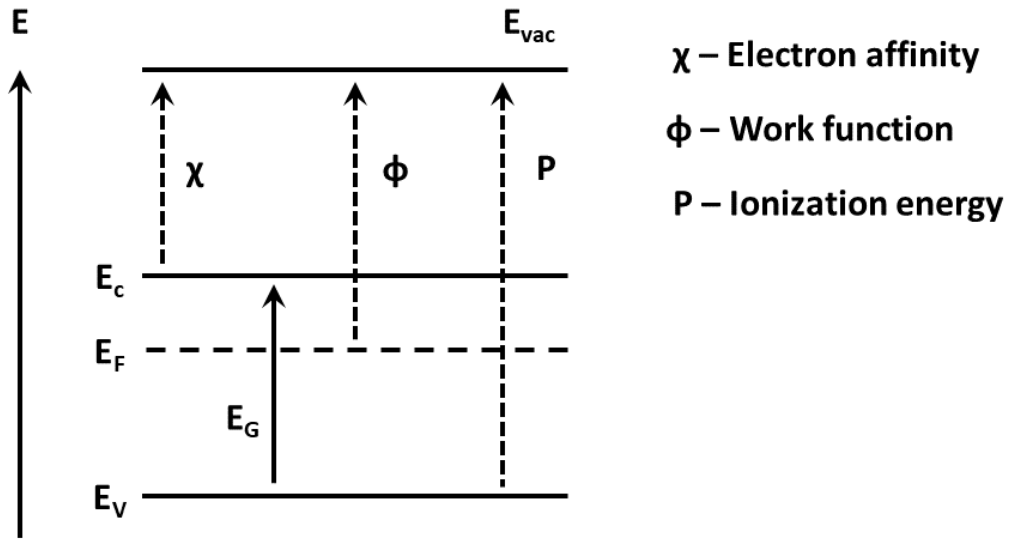

Figure 2-2 *Energy level diagram for semiconductors and insulators. For metals, E_C is equivalent to E_F while E_V is sufficiently far in energy from vacuum.*

A method of measuring the work function was developed by Lord Kelvin, in which a probe metal and a surface to be measured are brought near one another to form a parallel plate capacitor. Fig. 2-3 shows the application of the Kelvin probe technique to measure the work function.[46] The probe and the sample are electrically connected to allow charges to flow, and a difference in potential is generated across the parallel plate capacitor as shown in Fig.2-3(b). The probe metal plate is then oscillated, which induces a current. A backing voltage is applied to the probe-sample circuit to reduce the voltage on the parallel plate capacitor until the current in the circuit is zero, and the backing voltage is equal and opposite in sign to the equilibrium voltage, V_{CPD}, of the probe-sample capacitor, shown in Fig.2-3(c). The applied backing voltage, V_{DC}, is equivalent to the potential difference in the Fermi level of the two plates, *i.e.* probe and sample, which indicates the difference in work functions, V_{CPD}. A calibration can be used to determine the absolute work function of the metal probe and samples.

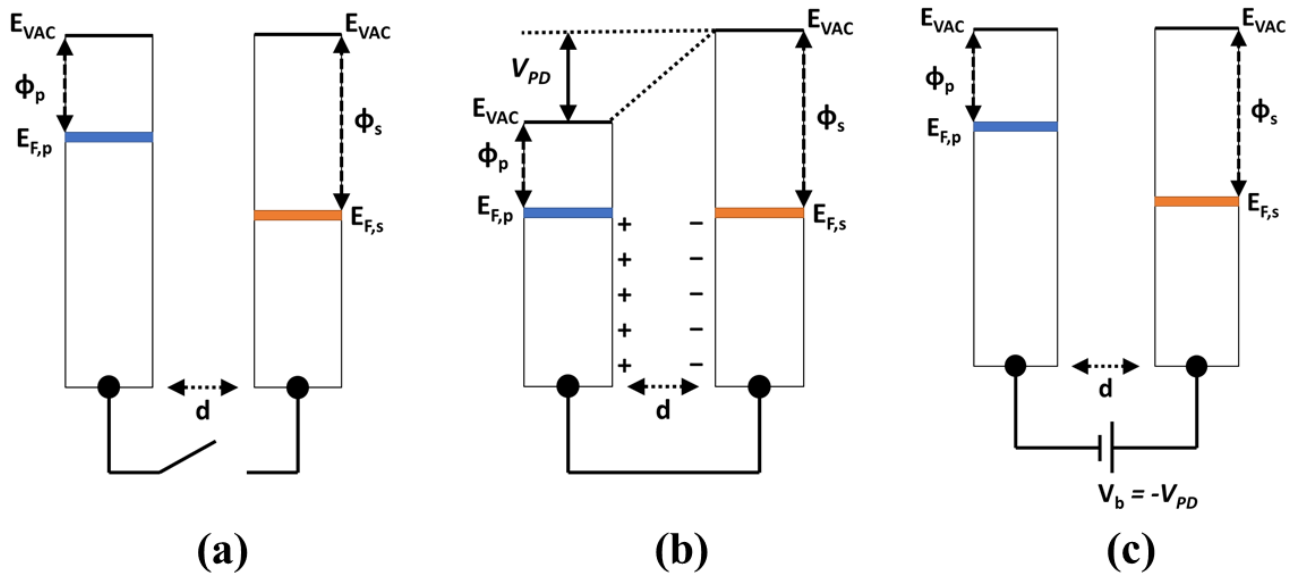

Figure 2-3 *Working principle of Kelvin probe measurement. The sample (s) and probe (p) are brought together a distance, d, which oscillates.* ***(a)*** *Sample and probe band diagrams at equilibrium and disconnected.* ***(b)*** *Sample and probe are electrically connected and forms a parallel plate capacitor with generated potential* V_{PD}*.* ***(c)*** *A backing potential,* V_b*, is applied that is equal and opposite to* V_{PD} *such that the system is an open circuit,* i.e. *current is equal to zero.*

Work functions measured by Kelvin probe for various materials relevant to the discussion of HgTe CQD photodiodes are summarized in Table 2-1. The setup here consisted of a function generator that drives an oscillating metal probe. Samples are prepared on conductive substrates and placed into the circuit. The current is output through a pre-amplifier and then measured with an oscilloscope. A variable voltage source is connected, and the backing voltage is adjusted until the current is zero. The value of the relative voltage difference is then recorded. All measured values are provided with respect to the potential of the HgTe CQDs treated with EdT/HCl ligands and on an absolute scale using 5.1 eV for Au as a reference.

Table 2-1 *Values for the work function of materials relevant to HgTe CQDs photodiodes as measured by chemical potential difference (Kelvin probe) and reported in literature. *An absolute work function of 5.1 eV is assumed for Au.*

Material	Relative potential difference (vs. HgTe) (eV)	Work Function* (eV)	Literature Work Function (eV)
HgTe CQDs (EdT/HCl)	-	4.86	4.7 ± 0.1[25]
NiCr	-0.04	4.82	5.24 ± 0.07 (Ni, 111)[47] 4.5 ± 0.15 (Cr, polycrystalline)[48]
Indium Tin Oxide	0.02	4.88	
Ag	-0.49	4.37	4.53 ± 0.07 (111)[47]
Au	0.24	5.1	5.33 ± 0.06 (111)[47]
Ti	-0.56	4.3	4.33 ± 0.01 (polycrystalline)[48]
TiO_2	-0.14	4.72	4.9 (Anatase, 001)[49] 4.51-5.62 (polycrystalline)[50]
MoO_X	0.47	5.33	5.0[51]
Ag_2Te NPs (EdT)	0.22	5.08	-

The uncertainty in the relative potential is on the order of 0.1 eV and depends on the surface conditions, method of preparation, and ambient environmental factors such as humidity. It is also worth noting that the accuracy of the absolute work functions is limited by the accuracy of the Au reference. Still, Table 2-1 provides a reasonable starting point for determining which materials will work well with HgTe CQDs as electrodes, electron transport layers, and hole transport layers. When considering the energy level alignment, note that for metals the Fermi level lies in the

conduction band while for doped conducting metal oxides it is often assumed that the Fermi level and the conduction band minimum are nearly equivalent in energy. However, the doping of metal oxides and other semiconductors depends on the method of fabrication and handling; therefore, additional techniques such as photoelectron spectroscopy are often required to obtain a more complete energy level diagram.

From only the work functions in Table 2-1, it becomes apparent that NiCr and indium tin oxide, or ITO, would make for good Ohmic contacts to HgTe CQDs given their small relative potential difference. Ohmic junctions allow majority carriers to easily flow to and from the semiconductor, *i.e.* the contact resistance is low, and are important for efficient current collection. For a n-type semiconductor, Ohmic contacts can form when conductors have work functions lower in energy than the semiconductor. For a p-type semiconductor, Ohmic contacts can form with conductors having work functions higher in energy than the semiconductor. In contrast to the Ohmic contact, a Schottky barrier can also form at a metal-semiconductor contact and instead restricts the free flow of the current, thus increasing the contact resistance. This can occur for a n-type semiconductor when the Fermi level of the conductor is greater in energy and for a p-type semiconductor when the conductor Fermi level is lower in energy than the semiconductor. Therefore, Ti and Ag would be expected to form Schottky junctions with p-type HgTe CQDs while Au may likely form an Ohmic contact.

TiO_2 has a work function smaller than HgTe CQDs by ~0.15 ± 0.1 eV for good alignment to the HgTe CQD conduction band energy, and it could be a good electron transport layer given the wide band gap of ~ 3 eV.[49] Further discussion on the use of TiO_2 as an electron transport layer

in HgTe CQD photodiodes is provided in section 2.2.3 below. Ag_2Te and MoO_X have work functions larger in energy than the HgTe CQDs and could be good for hole transport and collection. However, the nature of the junction between HgTe CQDs and MoO_X or Ag_2Te is difficult to predict and would depend on knowledge of the electron affinity, band gap, and doping density of the semiconductors. Further discussion on the use of MoO_X, and other polymeric materials, as a hole transport layer in HgTe CQD photodiodes is provided in section 2.2.4 below.

2.2.2 On the electrode: comparing NiCr, Ti, and ITO

In the proof-of-concept photodiode reported by Guyot-Sionnest and Roberts in 2015, a NiCr/HgTe/Ag_2Te/Ag-paint photodiode prepared on a CaF_2 window demonstrated background-limited photodetection in the mid-wave infrared.[43] Here, we begin our discussion of the evolution of the HgTe CQD photodiode. The first change was to replace the soft, brittle CaF_2 window with IR-transparent undoped silicon or sapphire substrates, which are more robust and easier to handle.

The choice of electrode materials depends on its infrared transparency and conductivity. The utility of NiCr was noted by Guyot-Sionnest and Roberts[43] who postulated, "the rectification is therefore likely determined by the top barrier while the NiCr is indifferent." The authors identify NiCr as an Ohmic contact to the lightly p-type HgTe CQDs, which is consistent with the small difference in the work function given previously in Table 2-1. Additionally, this indicates the significance of charge transport layers, such as Ag_2Te nanoparticles, in the successful fabrication of a rectifying photodiode. Without the use of Ag_2Te, and in agreement with an observation made by the authors, the photodiodes were largely Ohmic even at low temperatures.

In contrast to the passive Ohmic function of NiCr, a low work function titanium (Ti) electrode was tested to form a Schottky junction and possibly improve the rectification of the photodiode. It is worth noting here that the rapid formation of a surface oxide may interfere with an accurate measure of the Ti work function. Therefore, photodiodes were prepared with Ti in the same manner as the Ti was prepared for the Kelvin probe measurement such that the measured work function is representative of the potential difference between the HgTe and Ti layers. For the photodiode, the electron collection efficiency was poor and a large series resistance was measured, which may be explained by a large energy offset between the layers. The work function difference between the HgTe CQDs and the Ti layer is larger than the band gap of MWIR HgTe CQDs, which implies a conduction energy discontinuity greater than ~0.25 eV, as shown qualitatively in Fig. 2-4. This barrier blocks all currents in the detector and increases the series resistance. Such barriers should be avoided to ensure good photodetector performance and emphasizes the importance of evaluating characteristics such as electron affinity and band gap in addition to the work function of the solids in the heterojunction.

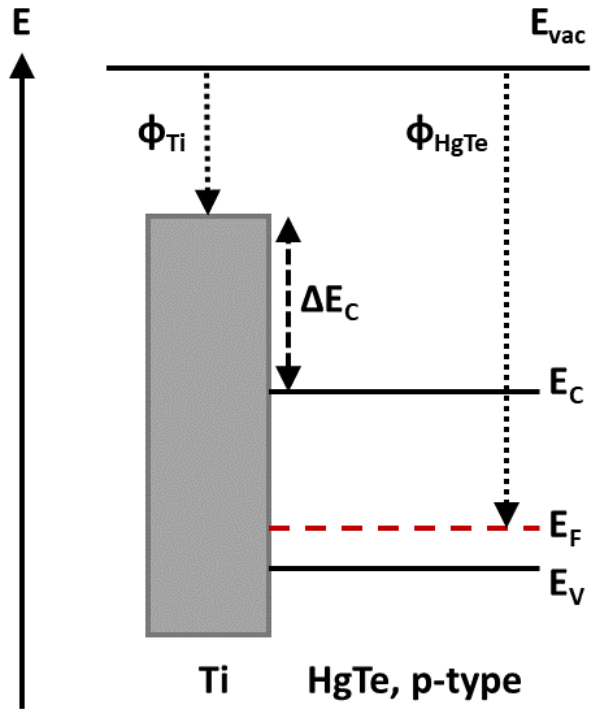

Figure 2-4 *Flat band energy diagram of the conduction band offset between Ti metal and p-type HgTe colloidal quantum dots.*

Due to the low transparency of metal thin films in the infrared and the limited choice of metals with work functions near the HgTe CQDs work function, the use of an n-type, high work function transparent conducting indium tin oxide, or ITO, film was introduced. Indeed, in other photovoltaic and light-emitting devices, ITO has commonly been used as an anode or hole-injecting material because of its relatively high work function.[52] A method of preparing ITO by sputtering under argon and annealing in ambient at 300^{o}C for 1 hour resulted in conductive ITO with resistivity of ~2×10^{-4} Ωcm and IR transparency greater than 60% from 1-5 μm. In addition to the transparency and conductivity, the ITO work function, provided in Table 2-1, was nearly

equivalent to the HgTe CQDs, making it an ideal electrode for all subsequent devices described here.

2.2.3 Electron transport layers

HgTe colloidal quantum dots with EdT/HCl ligands have a relatively high electron work function near 4.7 eV[53] and narrow band gap (~300 meV) for mid-infrared photodetection. Therefore, energy matching to charge selective transport layers is challenging given the limited number of charge transport layers with relevant energy levels between 4.5 and 5 eV to allow for charge carrier selection. Of the commonly used n-type electron transport layers (ETL), TiO_2 and SnO_2 have electron affinities and work functions closely matching HgTe CQDs. [49 54–56 57] The discussion to follow presents the work on ETL-HgTe CQD heterojunctions where TiO_2 and SnO_2 were used as electron-selective transport layers. The ETL was prepared on an ITO electrode, then coated with EdT/HCl-treated HgTe CQDs to form a conductive film. Finally, in each photodiode, Ag_2Te nanoparticle thin films were used as a junction layer with an Au electrode.

TiO_2 was fabricated on an ITO electrode by various techniques including the native oxidation of evaporated Ti metal, thermal oxidation of Ti metal, and hydrolysis of titanium alkoxide sol-gel solutions after spin-coating. Under ambient conditions, the formation of a 2-3 nm thin film of titanium oxide on titanium is known to form.[5859] The native oxide transport layer was prepared by evaporation of Ti to functionalize the ITO interface and then stored in air prior to making the photodiode. The oxidation of titanium is further encouraged by baking at high temperatures, and here a titanium thin film was oxidized at 350^{o}C for 1 hour under atmosphere to completely convert a 4 nm metal film to its oxide species. TiO_2 by hydrolysis was prepared by

spin-coating a 1% by weight titanium isopropoxide in isopropanol solution and baked at 170^{o}C for 10 minutes.

First, a TiO_2 ETL prepared by thermal oxidation of 4 nm of Ti metal was tested in a photodiode and had the current density-voltage (JV) behavior shown in Fig. 2-5(a). The photovoltaic effect was quite weak with negligible photocurrent under short-circuit conditions, small open-circuit voltage, and weak rectification with a photoresponse dominated by photoconductive currents.

Given that native oxide TiO_2 forms with a thickness of 2-3 nm, the effect of the Ti metal thickness on the ETLs was tested for 2 nm, 4 nm, and 8 nm of evaporated Ti. In the 2 nm case, the Ti metal is expected to convert completely to TiO_2. Fig. 2-5(b) and (c) demonstrate two cases for the 2 nm Ti metal that were observed. In Fig. 2-5(b) the response is like the case of the 4 nm thermal oxide TiO_2. However, in Fig. 2-5(c), the JV behavior is more like the 4 nm and 8 nm Ti metal films with native oxide. Fig. 2-5(d) and (e) show the JV behavior for the 4 nm and 8 nm cases where the Ti metal is expected to be present in a junction ITO-Ti(TiO_2) due to the self-terminating process of native TiO_2. The presence of the Ti(TiO_2) junctions induced an unexpected kink in the JV behavior. While the junction between Ti-TiO_2 is expected to be Ohmic for n-type TiO_2, the specific nature of the junction will depend on the TiO_2 doping. TiO_2 displays amphoteric conductivity with doping that depends on the oxygen vacancies, titanium vacancies, and titanium interstitials where each of these values depend on the manner of processing.[60] Here, the doping density of the native oxide TiO_2 was not characterized and it is possible that a Schottky junction between Ti metal and p-type TiO_2 contributes to the observed JV behavior.

In one device, the Ag_2Te film was omitted and the Au was evaporated directly in contact with the HgTe CQDs to form an Ohmic contact. The JV behavior for the 8 nm native oxide Ti(TiO_2) photodiode without Ag_2Te is shown in Fig. 2-5(f). The increased short-circuit current density and open-circuit voltage suggest a reasonable photovoltaic effect due to the Ti(TiO_2)-HgTe CQD junction, however, the rectification, especially under illumination, is poor. Without a hole transport/electron blocking layer such as Ag_2Te, the photodiode leakage current under bias was quite large.

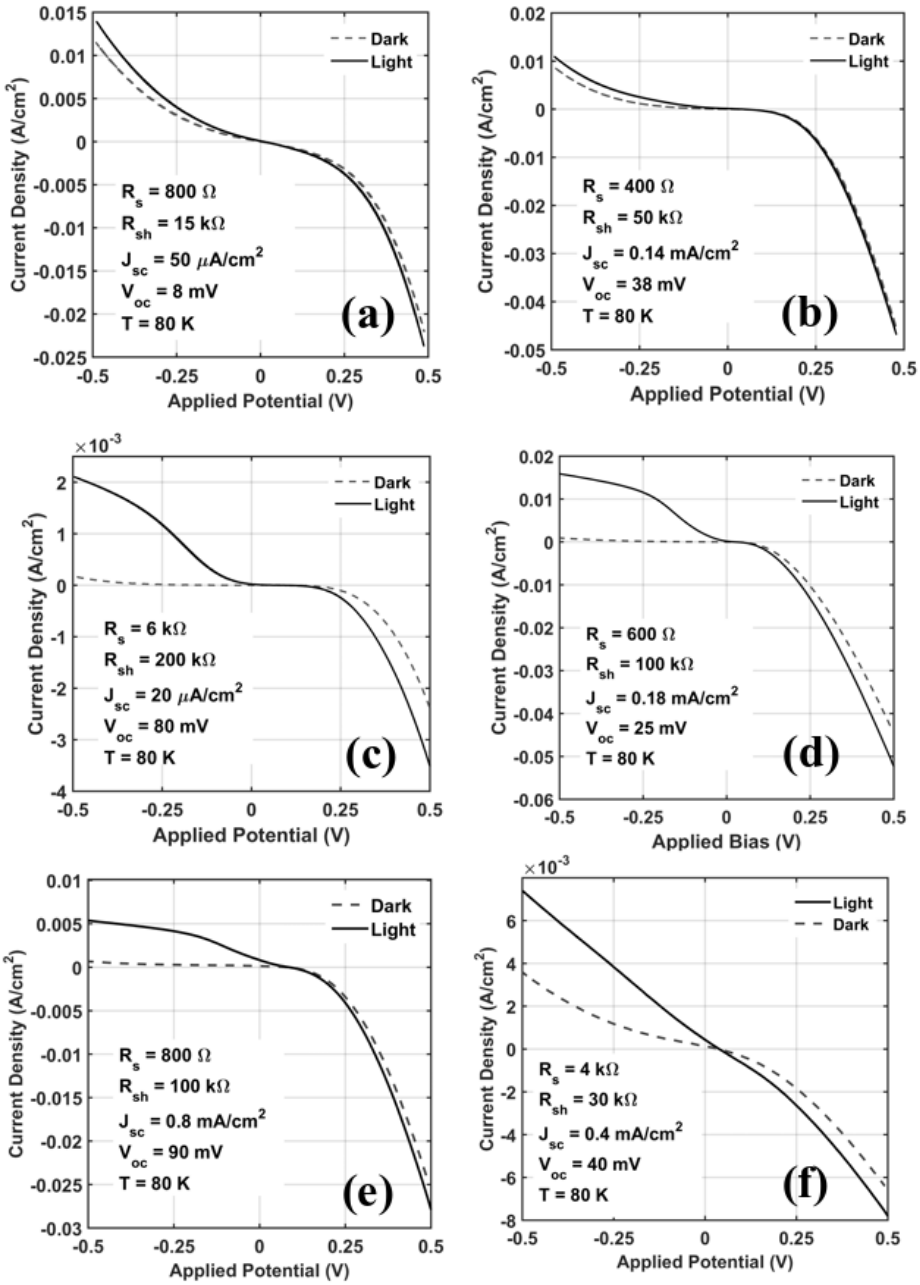

Figure 2-5 *Current density-voltage (JV) behavior for photodiodes with TiO_2 electron transport layer. TiO_2 prepared by* ***(a)*** *thermal oxidation at 350^{o}C,* ***(b,c)*** *native oxidation of 2 nm Ti metal,* ***(d)*** *native oxidation of 4 nm Ti metal,* ***(e)*** *native oxidation of 8 nm Ti metal,* ***(f)*** *native oxidation of 8 nm Ti metal without Ag_2Te nanoparticle layer.*

Natively oxidized Ti(TiO_2) ETLs had the largest shunt resistances larger by at least 2-fold and as much as 10-fold compared to photodiodes with TiO_2 films lacking the Ti metal layer. The lower shunt resistance of TiO_2 prepared by thermal oxidation suggests an increase in the net recombination in the photodiode, possibly due to defects formed during thermal oxidation. Further investigation of the crystallinity and doping density of TiO_2 prepared by thermal oxidation could provide insights here. Photodiodes consisting of 8 nm native oxide Ti(TiO_2) ETLs had the strongest photovoltaic effect with HgTe CQDs as indicated by the large open-circuit voltage and short-circuit photocurrent density. Otherwise, there were no obvious trends in these values with the thickness or manner of preparing TiO_2 ETLs.

One drawback of the native oxide Ti(TiO_2) ETL is the emergence of an S-shaped kink in the JV behavior. The origin of the potential barrier is not well understood in the HgTe CQD-TiO_2 system. One explanation could be the presence of surface dipoles due to contamination or residual hydroxide species when the native oxide forms at room temperature.[61] Evaluation of the surface conditions by x-ray photoelectron spectroscopy paired with plasma treatments to eliminate these species would be immensely helpful here. Another possibility is hole accumulation at the interface due to defects in Ti(TiO_2) film, leading to increased recombination that is mitigated under an applied electric field.[62]

Not shown here, the hydrolyzed TiO_2 prepared by spin-coating from a sol-gel was largely Ohmic with a resistance greater than 200 kΩ. Though the noise was low due to the high resistance, the photocurrent density was also small at ~70 μA/cm^2. The high series resistance that is detrimental to the photocurrent density could be explained by a low conductivity of the hydrolyzed

TiO_2 or a large conduction band discontinuity that blocks photocurrent collection. However, without characterization of the resistivity, band energy levels, or crystallinity of the material it is difficult to assign a specific limitation to hydrolyzed TiO_2.

Clearly, future development of the electron transport layer using TiO_2 would benefit from an understanding of the correlation between microstructure and electronic structure, doping, and transport dynamics of the charge selective layer. Much work has been done on TiO_2 as an ETL;[63,64] this collective understanding should be applied to improving TiO_2 as an ETL in the HgTe CQD photodiode. The potential utility of TiO_2 is recognized by others and has been used with HgTe CQDs to fabricate shortwave infrared photodiodes and phototransistors where the lower electron affinity of the relatively wider-gap HgTe CQD is more closely matched to the conduction levels of the TiO_2. [65–67]

Table 2-1 summarizes the responsivity, noise, and specific detectivity for photodiodes with a TiO_2 ETL. The noise was measured with a fast Fourier transform (FFT) noise spectrum analyzer and a frequency bandwidth of 1 Hz. In the cases of thermally oxidized and spin-coated TiO_2 thin films, the responsivity was between 3-fold and 10-fold worse than when using natively oxidized Ti metal films. From Table 2-1, it becomes apparent that the use of an 8 nm native oxide Ti(TiO_2) resulted in the best specific detectivity of the ETLs tested here. Also notice that the use of a Ag_2Te nanoparticle film with Ti(TiO_2) yielded higher responsivity, decreased noise, and a 4-fold increase in the specific detectivity compared to a photodiode without the Ag_2Te nanoparticle film.

Table 2-2 *Performance at 80 K for photodiodes with electron transport layers*

Device Structure	Responsivity (mA/W)	Noise (pA)	Specific Detectivity (Jones)
ITO/TiO_2/HgTe/Ag_2Te/Au (TiO2 by spin-coating)	7	0.2	4×10^9
ITO/TiO_2/HgTe/Ag_2Te/Au (Thermally oxidized, 350°C)	6	0.75	8×10^8
ITO/Ti(TiO_2)/HgTe/Ag_2Te/Au (native oxide, 2 nm Ti)	2	0.2	1×10^9
ITO/Ti(TiO_2)/HgTe/Ag_2Te/Au (native oxide, 4 nm Ti)	20	0.3	6.7×10^9
ITO/Ti(TiO_2)/HgTe/Ag_2Te/Au (native oxide, 8 nm Ti)	90	0.3	3×10^{10}
ITO/Ti(TiO_2)/HgTe/Au (native oxide, 8 nm Ti)	45	0.6	7.5×10^9
ITO/SnOx/HgTe/Ag_2Te/Au (SnOx by spin-coating)	1	0.2	5×10^8

Overall, the performance when using native oxide Ti(TiO_2) was only comparable to NiCr/HgTe/Ag_2Te/Ag-paint on CaF_2 by Guyot-Sionnest and Roberts[43] and might be improved by addressing the potential barrier that was present in the photodiodes. The S-shaped kink has been eliminated in solar cells that use TiO_2 by increasing the doping of TiO_2 to lower its work function with respect to the absorber,[68] by replacing it with aluminum-doped zinc oxide,[69] or by replacing TiO_2 with the more stable SnO_X electron transport layer.[70]

Like TiO_2, SnO_2 has been investigated for use as an electron transport layer in perovskite solar cells.[71–73] SnO_2 was reported to have higher electron mobilities than TiO_2, and its advantages

depend on the specific energy matching of the absorber to the SnO_2 electron transport layer.[74] The thin films of SnO_2 can be prepared with low temperature processes by spin-coating from a solution of $SnCl_2$ in ethanol followed by baking at 180-190^oC on a hot plate for 1 hour under atmosphere and lead to improved power conversion efficiencies for perovskite solar cells.[71,75] The similarity of SnO_2 to TiO_2, its reported higher mobility, and low temperature solution processing make SnO_2 a reasonable candidate ETL for HgTe CQD photodiodes.

Here, sub-stoichiometric SnO_X was prepared by hydrolysis with $SnCl_2$ precursor dissolved in ethanol and spin-coated onto the ITO/sapphire substrate. After spin-coating, the thin film was baked at 180^oC for 1 hour to drive out the water and convert the thin film from hydroxide to the SnO_X species. The device design consisted of ITO/SnOx/HgTe/Ag_2Te/Au and had a specific detectivity of 5×10^8 Jones at 80 K for a 5 μm spectral cutoff as reported in Table 2-1 above. At 80 K, the photoresponse was very poor with quantum efficiency of <0.1%, much worse than the TiO_2 ETLs. The short-circuit photocurrent density was negligibly small, shown in Fig. 2-6(a), and requires reverse bias operation in excess of 500 mV to achieve a quantum efficiency of ~1%.

The spectral response for the photodiode with a SnO_X electron transport layer is shown in Fig. 2-6(b). The spectral response was measured with a Nicolet Fourier transform infrared (FTIR) spectrometer with an internal blackbody source and deuterated triglycine sulfate (DTGS) pyroelectric detector. Also shown by the solid green line in Fig. 2-6(b) is an ideal spectral response that was calculated by taking the product of the HgTe CQD absorption spectrum with the spectrum of the internal blackbody source as measured by the DTGS detector. For a thin film photodiode,

the ideal spectral response represents a photodiode where contributions from all wavelengths of light to the photocurrent are consistent with the HgTe CQD absorption.

The spectral response can deviate from ideality due to inefficient current collection in each region of the photodiode. Consider the SnO_X ETL photodiode at short-circuit conditions, the relative intensity of the spectral response at smaller wavenumbers (*i.e.* shorter wavelengths) is nearly equivalent to the response at longer wavelengths; this indicates that longer wavelengths are contributing much less to the photocurrent, *i.e.* have a much lower quantum efficiency, than would be expected in comparison to the relative intensities of the ideal response. The efficiency at longer wavelengths begins to improve as a reverse bias is applied to the photodiode, which is apparent from the increasing relative intensities at longer wavelengths as the dashed gray line approaches ideality in Fig. 2-6(b). The shape of the spectral response then provides qualitative information about the operation of the photodiode, *e.g.* that the depletion region may be nearer to the SnO_X ETL where radiation is incident and that the diffusion length is short such that carriers generated by longer wavelengths in neutral regions away from the junction quickly recombine. The effect of the external bias to increase the efficiency at longer wavelengths further suggests that diffusion lengths are still quite short in the SnO_X-HgTe CQD photodiode, even at low temperatures.

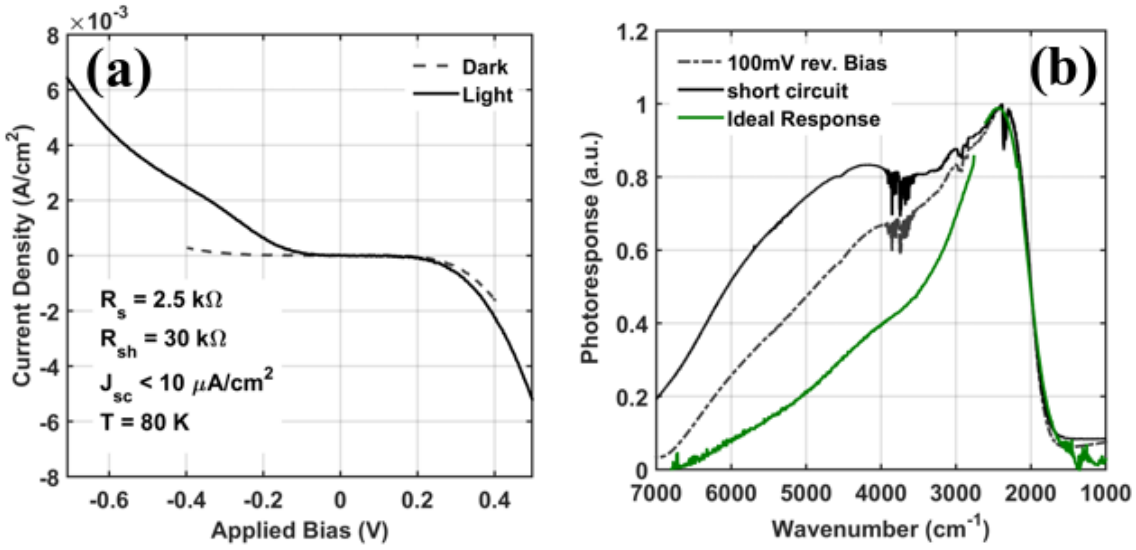

Figure 2-6 (a) *Current density-voltage behavior of photodiode ITO/SnOx/HgTe/Ag2Te/Au and* ***(b)*** *spectral response at 80 K under zero applied bias (solid) and 100 mV reverse bias (dashed) with a 50 % spectral cutoff at 5 µm. Ideal response (solid green) calculated from HgTe CQD absorption spectrum and FTIR internal blackbody spectrum measured by DTGS pyroelectric detector.*

The results on SnO_X presented here offer limited insights toward improving its use as an ETL. Much more could be learned about hydrolyzed SnO_X by x-ray diffraction, photoelectron spectroscopy, and resistivity or mobility measurements. Collectively, this information would provide a more thorough analysis of the advantages and limitations of SnO_X as an ETL in HgTe CQD photodiodes. Though it might be possible to optimize the properties of SnO_X ETL by doping, post-processing, and surface functionalization, the results here are not a promising start for the use of SnO_X as an electron transport layer in HgTe CQD photodiodes.

2.2.4 Hole transport layers

As with the electron transport layers of the previous section, the challenge is to match the valence band level of the HgTe CQDs to the hole transport layer (HTL). Here, the challenge arises because the valence band maxima of many common materials are much higher in energy than the

valence band energy (4.7-4.8 eV[53]) for EdT/HCl-treated HgTe CQD films. Therefore, a small number of commonly used HTLs were selected for their relatively small energy difference to HgTe CQDs. Here, the polymeric HTLs PEDOT:PSS, P3HT, PVK and the oxide HTL MoO_X were tested in an HTL-HgTe CQD heterojunction photodiode. The general structure of the photodiode consisted of ITO/HgTe/HTL/Au and any deviations from this structure are discussed.

In optoelectronic devices, a mixture of poly(3,4-ethylenedioxythiophene) and polystyrene sulfonate acid, also known as PEDOT:PSS, and polyvinylcarbazole (PVK) are commonly used polymeric hole transport layers. The highest occupied molecular orbital (HOMO) level of PEDOT:PSS has a range of 4.7-5.2 eV, which depends on the processing,[76] and the Fermi level varies over this range with the ratio of the polymer blend.[77] Similarly, PVK has an ionization energy between 5.1-5.4 eV[78] and has been used as a replacement for PEDOT:PSS in optoelectronic devices for its improved stability.[79]

First, PEDOT:PSS was tested in a device consisting of ITO/HgTe/PEDOT:PSS/Au. At 80 K the detector responsivity was ~13 mA/W and the photodiode resistance was ~1 kΩ with nearly Ohmic behavior. Similarly, PVK was prepared by spin-coating in a photodetector structure of ITO/HgTe/PVK/Au. At 80 K, the responsivity was ~17 mA/W and the Ohmic behavior of the photodiode resulted in detrimental noise levels. From the responsivity measured under short-circuit, it is clear that a weak photovoltaic effect was present in the HgTe CQD-PEDOT:PSS and HgTe CQD-PVK heterojunction. However, low photodiode resistance and Ohmic behavior suggest poor carrier blocking, and it is apparent that PEDOT:PSS and PVK are ineffective HTLs for HgTe CQD photodiodes.

Poly(3-hexathiophene), or P3HT, has previously been used in a HgTe CQD photovoltaic device,[80] and has a relatively low HOMO energy level of about 5.2 eV. While PEDOT:PSS and PVK, like many polymers, have mobilities on the order of 10^{-4}-10^{-6} cm^2/Vs, an advantage of P3HT is a carrier mobility as large as 10^{-1} cm^2/Vs, which makes it ideal for many optoelectronic applications.[81,82] Here, such high mobilities could better facilitate charge collection from the absorber HgTe CQDs and improve the responsivity.

In a device structure of ITO/HgTe/P3HT/Ni/Au, an effect of the thickness of P3HT was noted in a few early devices. The photocurrent density increased by 40-fold from 8 $\mu A/cm^2$ up to .3 mA/cm^2 as the P3HT thickness decreased from 60 nm to ~20 nm after diluting the P3HT concentration. Fig. 2-7(a) shows the JV behavior at 80 K where the photodiode demonstrates good short-circuit photocurrent density but weak rectification and a small open-circuit voltage. Clearly, there is significant dark current under reverse bias operation and the P3HT provides little benefit to blocking this current and reducing the noise in the photodiode. Therefore, a TiO_2 ETL was included to assist in reducing the dark current and noise. Fig. 2-7(b) shows the JV behavior for a photodiode consisting of ITO/TiO_2/HgTe/P3HT/Ni/Au where the shunt resistance increased slightly more than 2-fold with a marginal change in open-circuit voltage. However, the series resistance also increased slightly more than 2-fold and suggests that the TiO_2 only served to block both dark currents and photocurrents, which is noted by the 20% decrease in the short-circuit current density.

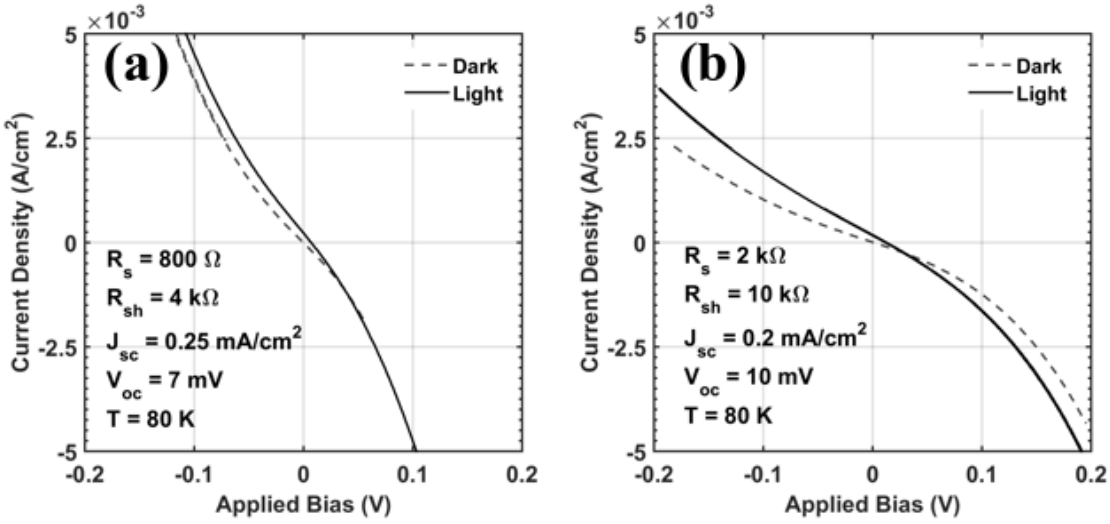

Figure 2-7 *Current density-voltage (JV) behavior of photodiodes consisting of* ***(a)*** *ITO/HgTe/P3HT(20 nm)/Ni/Au and* ***(b)*** *ITO/TiO_2/HgTe/P3HT(20 nm)/Ni/Au.*

While the TiO_2 provided little benefit to the rectification of the current, the addition of the ETL did fix the polarity of the photodiode, *i.e.* holes were collected at Au while electrons were collected at ITO. In the photodiode without TiO_2, the polarity would become inverted at low temperature. The source of the polarity inversion is not well understood at this time. Another small change that proved beneficial was the addition of a thin Ni layer before the evaporation of the Au electrode. With the Ni layer, the photocurrent density increased and the noise was reduced, leading to a 5-fold improvement in the specific detectivity from 1×10^9 Jones to 5×10^9 Jones at 80 K with a 5 μm spectral cutoff. The effect of the nickel could be to act as a barrier to Au diffusion as is common in electrical devices or to modify favorably the Au work function in contact with P3HT and thus improve carrier collection.[83]

In contrast to the polymeric materials previously discussed, the sub-stoichiometric metal oxides of vanadium oxide and molybdenum oxide selectively transport holes through shallow

donor defect states near their high-electron affinity conduction bands, contributing to improved charge extraction in polymer[84,85] and PbS colloidal quantum dot photovoltaics.[86] The work function of MoOx can be as high as 6.8 eV and depends on the surface conditions of the MoOx film, which decreases in energy with exposure to air and other contaminants. [87,88]

MoOx prepared by thermal evaporation directly on PbS CQDs and exposed to air was reported by Gao *et al.*[86] to have a work function of ~5 eV, which is close to the energy of the HgTe CQDs. Therefore, following the same procedure, MoOx (10 nm) was prepared by thermal evaporation at a rate of 0.5-1 Å/s directly onto HgTe CQD thin films. After MoOx evaporation, the device stack was transferred in air to a second evaporator for Ni and Au metal deposition. The total photodiode structure consisted of ITO/HgTe/MoO_X/Ni/Au. Fig 2-8(a) shows an ITO/HgTe/MoOx/Ni/Au photodiode with weakly rectifying JV behavior. Similar to the P3HT photodiodes, the specific detectivity increased 40-fold with the addition of the Ni thin film due to 20-fold decrease in the noise as indicated in Table 2-2 below. In an effort to improve the rectification, an 8 nm natively oxidized Ti(TiO_2) film was included as an ETL with the MoOx HTL and the JV behavior is shown in Fig. 2-8(b). A small increase in the shunt resistance and open-circuit voltage indicates slightly reduced recombination with the addition of the Ti(TiO_2) layer but the rectification was otherwise weak.

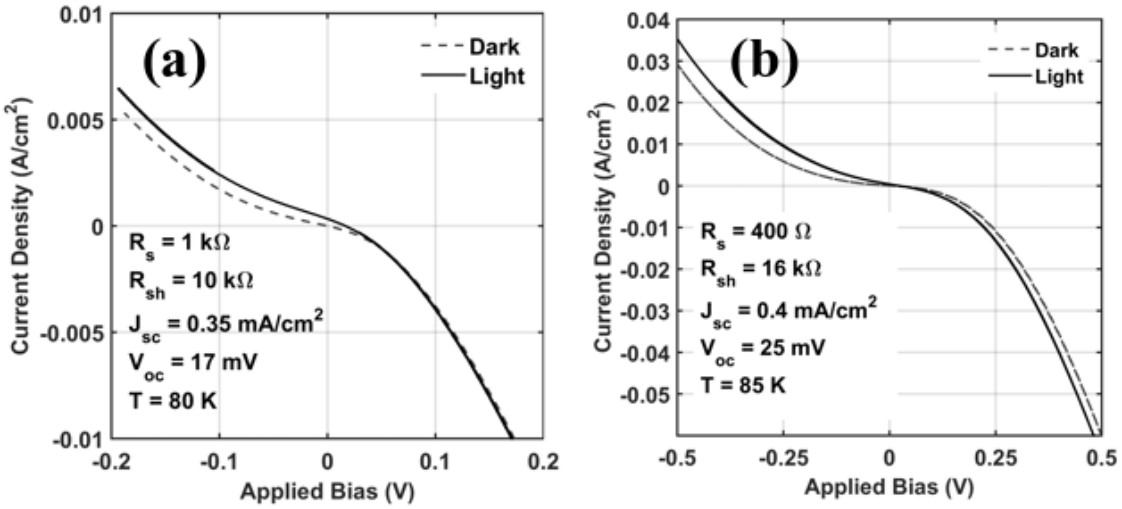

Figure 2-8 *Current density-voltage (JV) behavior of* ***(a)*** *ITO/HgTe/MoOx/Ni/Au and* ***(b)*** *ITO/Ti(TiO_2)/HgTe/MoOx/Ni/Au.*

Table 2-2 summarizes the different hole transport layers used in the HgTe CQD photodiodes. Of the charge transport layers, P3HT and MoO_X yielded the largest responsivity and specific detectivity. However, the figures-of-merit were still much less than that of the photodiodes with Ag_2Te nanoparticle thin films as reported by Guyot-Sionnest and Roberts.[43]

Table 2-3 *Performance at 80 K of photodiodes with hole transport layers*

Device Structure	Responsivity (mA/W)	Noise (pA)	Specific Detectivity (Jones)
ITO/HgTe/PVK/Au	17	20	8.5×10^{7}
ITO/HgTe/PEDOT:PSS/Au	13	12	1×10^{8}
ITO/HgTe/P3HT/Au	33	3	1×10^{9}
ITO/HgTe/P3HT/Ni/Au	80	1.5	5×10^{9}
ITO/TiO_2/HgTe/P3HT/Ni/Au (TiO2 by Atomic layer deposition)	17	0.9	2×10^{9}
ITO/HgTe/MoOx/Au (MoOx by thermal evaporation)	23	20	1.2×10^{8}
ITO/HgTe/MoOx/Ni/Au	39	0.9	4.3×10^{9}
ITO/Ti(TiO_2)/HgTe/MoOx/Au (native oxide, 8 nm Ti)	43	0.4	1.1×10^{10}

The first direction to overcome the challenges of working with Ag_2Te was to replace it with more commonly used hole transport layers with standard fabrication protocols. Following from the previous discussion, this proved unsuccessful and Ag_2Te remains the preferred hole junction layer. The challenge with Ag_2Te was the variation in the synthesis and thickness of the Ag_2Te nanoparticle films that resulted in behavior ranging from Ohmic to insulating. The focus shifted toward developing better protocols for preparing Ag_2Te nanoparticles and films for reliable photodiode operation. The details of this work are discussed in Chapter 3.

2.2.5 Conclusion

Electron and hole transport layers have been tested in HgTe CQD photodiodes for mid-wave infrared photodetection. Predicted by the work function and confirmed by design, indium tin oxide and nichrome were the best matched materials for Ohmic contact with EdT/HCl-HgTe CQD thin films. The infrared optical transparency greater than 60% for ITO makes it the preferred choice for the photodiodes described here. An ETL of TiO_2 prepared by native oxidation of an 8 nm film of Ti metal and a HTL of thermally evaporated MoO_X were the best candidate charge transport layers. Still, the photodiodes with ETLs and HTLs tested here did not perform better than the reported photodiodes consisting of an ITO or NiCr cathode and an Ag_2Te nanoparticle layer as previously reported. The experiments conducted on ETLs and HTLs here were limited by their characterization and future work would benefit from a more complete picture of the energy level alignment between HgTe CQDs with various ligands and the charge transport layers. Characterization techniques such as photoelectron spectroscopy, x-ray diffraction, field-effect mobility, and four-point resistivity method would provide information on the quality, transport, energy levels, and doping of the charge transport layers. As EdT/HCl was the only ligand solution used here, a measure of the relative energies and mobilities of various ligands would also contribute to the band engineering of high-performance HgTe CQD photodiodes.

2.3 HgTe CQD Homojunctions: Non-aggregating HgTe CQD n-type layers

In this section, the design and operation of the HgTe pn-homojunction photodiode is described and evaluated in the context of the current rectifying behavior. When possible, figures-of-merit are expressed. A final comment on the potential utility of non-aggregated HgTe CQDs in the HgTe pn-homojunction photodiode is given to motivate future work on this design.

Shen *et al.* developed a synthesis wherein a highly reactive bis-(trimethylsilyl) telluride (TMSTe) precursor was used for the growth of spherical, non-aggregating HgTe colloidal quantum dots.[89] Surprisingly, the spherical HgTe CQDs have n-type doping that is size-dependent, *i.e.* increasingly n-doped with increasing quantum dot size, evidenced by the onset of an intraband transition as was observed in ambiently doped HgS[90,91] and HgSe[92] CQDs. Prior to this synthesis, aggregated tetrahedral HgTe CQDs were invariably p-type and a pn-homojunction was not possible. Now, a homojunction using p-type aggregated tetrahedral and n-type spherical HgTe CQDs could be realized.

The spherical n-type HgTe CQDs were dropcast over the ITO cathode and crosslinked with a solution of tetrabutylammonium chloride (TBACl) and ethanedithiol (EdT) in isopropanol at a ratio of 1:1:20 by volume. After ~100 nm (2-3 layers) of material were deposited, the aggregated HgTe CQDs were dropcast and crosslinked with the same TBACl/EdT/IPA solution to a total thickness of ~400 nm. The device structure in total consisted of ITO/HgTe(n)/HgTe/Au where HgTe(n) refers to the n-type, non-aggregated HgTe spherical CQDs.

In designing the homojunction photodiode, the size of the n-type spherical HgTe CQDs was optimized with respect to absorption and doping properties. The size was selected such that the cutoff frequency was equivalent or slightly larger in energy than the p-type aggregated HgTe CQDs; this ensures the absorption cutoff is sharp due to the aggregated HgTe CQDs and minimizes additional thermally generated noise due to CQDs with narrower band gap energy. To increase the built-in potential of the diode, the doping of the HgTe(n) CQDs needs to be sufficiently large such that the Fermi level was near the conduction band level but not too large to prevent the intraband

absorption that would lead to broadening of the spectral response. Indeed, the optimal size of the spherical HgTe CQDs for a mid-wave photodetector was between 8-9 nm in diameter.[89]

The pn-homojunction photodiodes consistently showed rectification at reduced operating temperatures, as in Fig. 2-9, and in most cases were more rectifying with larger shunt resistance and open-circuit voltage than the photodiodes with electron and hole transport layers that were previously discussed. Therefore, the pn-homojunction successfully demonstrated a photovoltaic effect with a large built-in potential and a depletion region of good quality to increase the photodiode resistance and reduce the noise. At 80 K, the photocurrent density of 0.2-0.3 mA/cm^2 corresponds to a responsivity of 30 mA/W and, with a noise spectral density of ~0.25 pA/√Hz at a 1 Hz frequency bandwidth, a spectral detectivity of 1.2×10^{10} Jones for detection up to 5 μm.

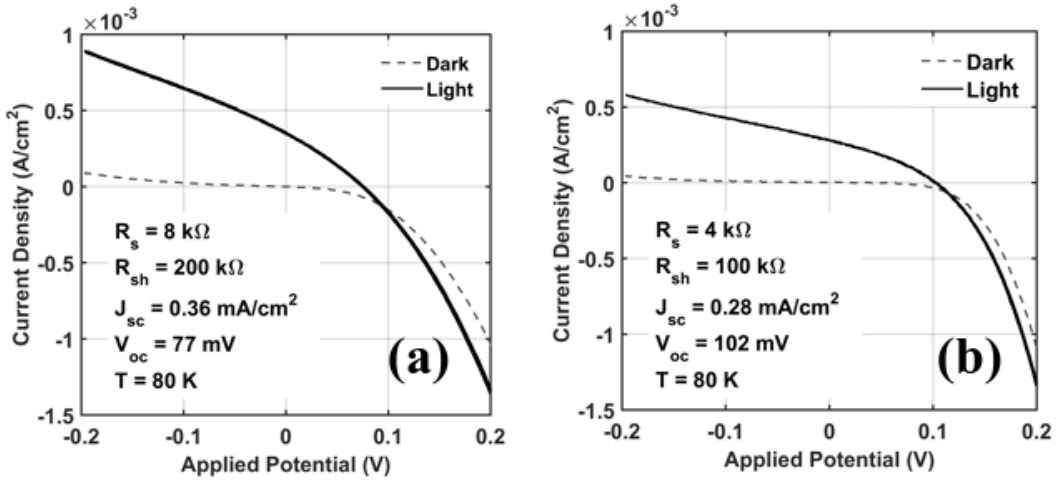

Figure 2-9 *Current density-voltage behavior for two different photodiodes consisting of ITO/HgTe(n)/HgTe/Au operating at 80 K.*

One limitation to the performance of the pn-homojunction was the low mobility, μ, of the spherical HgTe(n) CQDs. Notice from Fig. 2-9 that the series resistance was consistently larger

than 1 kΩ and likely the cause of the low quantum efficiency, ~1% at 80 K. The high series resistance is due to the lower $\mu \sim 10^{-4}$-10^{-3} cm^2/Vs for the n-type HgTe CQD compared to the 10^{-2} cm^2/Vs aggregated HgTe CQDs. Therefore, improving the mobility of non-aggregated HgTe CQDs could improve the photocurrent collection efficiency.

Another limiting factor was the uncertainty in the polarity of the photodiode. At room temperature, the polarity on the photodiode was well behaved with hole collection at the Au anode and electrons at the ITO cathode as designed. However, near 250 K, the polarity became inverted, *i.e.* with ITO as the anode and Au as the cathode, contrary to the device design. Fig. 2-10(b) shows the direction of transport for electrons and holes in the normal and inverted type photodiodes. The polarity inversion is apparent in the temperature response shown in Fig. 2-10(a) with photocurrent density first decreasing toward zero and then increasing with lowering of the operating temperature. Previously, the introduction of a TiO_2 ETL eliminated the polarity inversion in the case of the P3HT-HgTe CQD heterojunction photodiode. Similarly, introducing a junction material here such as TiO_2 or Ag_2Te nanoparticles may fix the polarity. Still, a better understanding of this phenomenon will be required for future development of the HgTe CQD photodiodes. The effect could be due to a temperature dependent change in the doping of the HgTe CQDs and, therefore, temperature-dependent field-effect transistor measurements on HgTe CQDs would provide insight into this phenomenon.

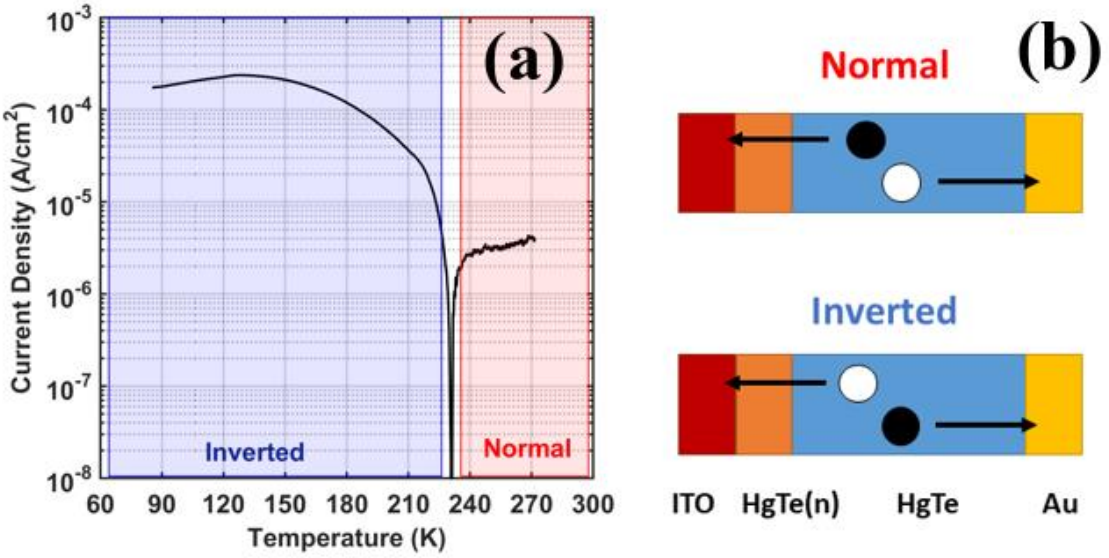

Figure 2-10 (a) *Temperature-dependent photocurrent density for ITO/HgTe(n)/HgTe/Au photodiodes.* ***(b)*** *Direction of carrier transport for electron and holes in a normal and inverted type HgTe CQD photodiode. White circles represent holes while black circles represent electrons.*

Finally, more recent work on the non-aggregated spherical HgTe CQDs has improved significantly the transport with mobilities, μ, approaching 1 cm^2/Vs when using a phase exchange process.[93] Chen *et al.* exchange the HgTe CQDs from a non-polar phase to a polar phase in the presence of ionic ligands of $HgCl_2$ and short-chain mercaptoethanol to replace the native non-polar ligands. Finer control of the HgTe CQD doping is achieved by choosing the initial doping level by the size of the HgTe CQDs and then varying the concentration of $HgCl_2$ in the polar phase. Additionally, the much shorter length of the ionic ligands than the native organic ligands makes it possible for HgTe CQDs to pack closer together in a film and improves the dot-to-dot coupling, thus enhancing the mobility.

The improved mobilities and tunable n-type doping elicits renewed investigation of the pn-homojunction to improve the MWIR HgTe CQD photodiode performance. The specific detectivity

could be proportional to the $\sqrt{\mu}$ for operating temperatures above the activation of hopping transport. Still, the improvement due to higher mobility is limited to photodiodes operating with an IQE less than unity where the efficiency is limited by the transport properties. Therefore, the improvement is especially beneficial for HgTe CQD photodiodes operating at high temperatures where the diffusion length is much shorter than the device thickness and the carrier collection efficiency is low. Control of the n-type doping can yield larger built-in potentials and greater rectification at higher temperatures, thus reducing thermal noise and improving sensitivity.

2.4 Summary

In this chapter, two methods for the fabrication of rectifying HgTe CQD photodiodes were discussed. These methods included the use of electron and hole transport layers and a pn-homojunction with ambiently doped n-type HgTe CQDs. Charge transport layers can lead to current rectification and high sensitivity photodetection but a more thorough understanding of the band energy alignment with HgTe CQDs is required. A pn-homojunction of HgTe CQDs demonstrated strong current rectification and good figures-of-merit at low temperatures with improvements in performance expected to come from higher mobilities and better control of the CQD doping. A third method, and the most successful method so far, for fabricating photodiodes by extrinsically doping HgTe CQD films with Ag ions will be the topic of Chapter 3 to follow.

Chapter 3 HgTe Colloidal Quantum Dot Mid-Wave Photodetection

This chapter describes the development of a mid-wave infrared HgTe CQD photodiode based on a solid-state cation exchange doping method. In contrast to the techniques described in Chapter 2, the aim of this work is to non-uniformly dope the films of HgTe CQDs with an extrinsic dopant, *i.e.* silver (Ag) ion, to build in a rectifying potential. To that end, a solid-state cation exchange process was developed and the details behind the process are discussed. To understand the role of the solid-state cation exchange process in a photodiode, physical insights are gathered through methods such as capacitance-voltage, x-ray photoelectron spectroscopy, and secondary ion mass spectrometry. Figures-of-merit for the HgTe CQD photodiode are discussed and further improved through optical enhancement to demonstrate infrared thermal imaging. The work described in this chapter is adapted with permission from Ackerman, M. M.; Tang, X.; Guyot-Sionnest, P. Fast and Sensitive Colloidal Quantum Dot Mid-Wave Infrared Photodetectors. *ACS Nano* **2018** *12* (7), 7264-7271. Copyright 2018 American Chemical Society.

3.1 Solid-State Cation Exchange of Ag_2Te Nanocrystals

This section describes the process of the solid-state cation exchange for doping HgTe CQD films in photodiodes. The formation of a rectifying junction in a semiconductor device relies on the difference in the doping density or Fermi levels of the materials that make up the junction. Previously, a rectifying homojunction was realized by using n-type non-aggregated HgTe CQDs in contact with slightly p-type HgTe CQDs (see Section 2.3 for details). Here, an extrinsic Ag dopant is used to create a relative difference in the p-type doping across the HgTe CQD film thickness. The implication of Ag as a dopant in HgTe CQDs was first commented on by Guyot-Sionnest and Roberts[43] who noted that "it is possible that the silver paint forms the p-contact by

diffusion of Ag ions in the HgTe dots." The possible influence of Ag ions in the HgTe CQD films on the rectification of these reported photodiodes has motivated the work to follow here.

The simplest idea for introducing Ag ions into the film by diffusion is to briefly expose the film to a solution of Ag ions. Therefore, thin films of HgTe CQDs were prepared and briefly exposed to solution of $AgNO_3$ in methanol (10 mM). However, the Ohmic electrical behavior of photodiodes prepared by soaking in a solution of Ag ions suggests that the Ag diffusion by soaking did not lead to any non-uniform doping density. Instead, the Ag ions likely diffuse uniformly throughout the HgTe CQD film and do so rapidly. This is better understood by considering the nature of the CQD film. In contrast to a bulk semiconductor that is ideally contiguous and crystalline, films of CQDs are by nature porous due to random packing of the nanocrystals into a polycrystalline film. Therefore, the Ag ion solution diffuses readily throughout the film and the Ag distribution is isotropic. To form a junction by doping with Ag ions would then require processes that separate the doping and diffusion steps such that the Ag distribution is non-uniform.

Rather than dope the CQD films directly, extrinsically doped HgTe CQDs could possibly be formed in solution and then deposited to form an abrupt junction with intrinsic HgTe CQD films. Solution phase doping of CQDs has been achieved by mixing CQDs with additional impurity ions that diffuse into the CQDs as either interstitial or substitutional dopants;[94] however, predicting the dopant type can be difficult and depend on the dopant density.[95] In the extreme case of diffusion in CQDs, in-diffusion of impurity ions can lead to a complete cation exchange where the original cations in the lattice are replaced by a new cation, transforming into a different

semiconductor altogether. If the cation exchange process can be controlled, then it becomes a useful tool for realizing extrinsically doped CQDs.

The cation exchange process is determined by many factors including the thermodynamics of the cation exchange, the hard/soft acidity of the cations being exchanged, the solubility of the nanocrystal solids formed, and the ligands that can bind selectively to one cation over another to facilitate the exchange. De Trizio and Manna have summarized well in a recent review each of these factors and the principles for cation exchange in colloidal nanoparticles.[96] As a rule of thumb, expressed by Eq. (3.1), comparing the solubility products, or K_{sp}, of different solids is a starting point for predicting cation exchange in colloidal nanocrystals.

$$AX(s) + B^{+}(aq) \rightarrow A^{+}(aq) + BX(s), \qquad K_{sp,AX} \gg K_{sp,BX} \tag{3.1}$$

In the case of HgTe and Ag_2Te semiconductors, the solubility products are not known. Generally though, Hg chalcogenides are less soluble (*i.e.* have a smaller solubility product) than Ag chalcogenides. For example, Ag_2S and Ag_2Se have solubility products of 3×10^{-50} and 1×10^{-54}, respectively, while HgS and HgSe have values of 6×10^{-53} and 4×10^{-59}, respectively.[97] Therefore, it is expected that HgTe will be much less soluble than Ag_2Te. Indeed, the effectiveness of the solution-phase cation exchange of Ag_2Te with Hg ions has been reported in both Ag_2Te nanowires[98] and Ag_2Te nanoparticles[99] in accordance with the rule of thumb. Here, to form doped HgTe CQDs in the solution phase, the cation exchange process begins with the synthesis of Ag_2Te nanoparticles and follows with exposing the Ag_2Te nanoparticles to a $HgCl_2$ alcoholic solution.

The synthesis of the Ag_2Te nanoparticles begins by dissolving $AgNO_3$ (0.2 mmol) in oleylamine (5 mL) and oleic acid (0.5 mL) at 70°C under nitrogen. Once dissolved,

trioctylphosphine (0.5 mL) is injected and the solution is rapidly heated up to 160^{o}C. At the reaction temperature, trioctylphosphine-telluride (TOPTe, 1M, 0.1 mL) is rapidly injected. The solution immediately turns black and proceeds for 10 minutes to grow the nanocrystals. Finally, the reaction is removed from heat and cooled to room temperature. The crude solution is stored in the freezer to extend the lifetime of the nanoparticles and aliquots are removed as needed for preparing samples. For use, 0.2 mL of Ag_2Te crude solution is precipitated with methanol, the supernatant is removed following centrifugation, and the nanoparticles are dispersed with ~25 µL of 1-dodecanethiol and 0.2 mL of chlorobenzene. Twice more the solution is precipitated with methanol, centrifuged to remove the supernatant, and re-dispersed in chlorobenzene. At the third precipitation, after discarding the supernatant and drying the pellet lightly with nitrogen, the Ag_2Te nanoparticle are re-dispersed in an organic solvent (*e.g.* toluene, hexane:octane) to a desirable concentration and are ready for use. Fig. 3-1 shows a transmission electron microscope image and histogram of the Ag_2Te nanoparticles with a range of sizes from 5-14 nm that form during the synthesis.

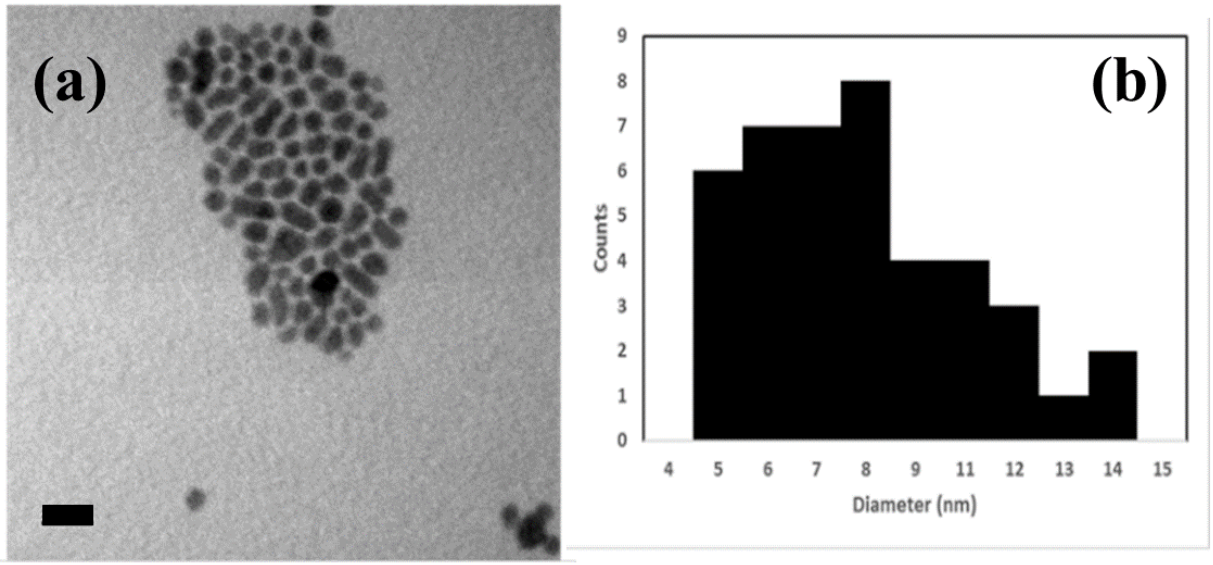

Figure 3-1 (a) *Transmission electron microscope of Ag_2Te nanoparticles. Scale bar is 20 nm.* ***(b)*** *Size distribution of Ag_2Te nanoparticles.*

For the solution phase cation exchange, Ag_2Te nanoparticles were cleaned and solvated with toluene. $HgCl_2$ was dissolved in methanol at a concentration between 10 mM and added dropwise to the Ag_2Te nanoparticle solution. After mixing at room temperature for 1 min, the solution was precipitated with isopropanol and re-dispersed in toluene or tetrachloroethylene with limited colloidal stability. Later, it was found that the addition of a small amount (<0.1 mL) of 1-dodecanethiol followed by precipitation with ethanol or isopropanol could produce stable colloidal solutions in toluene, tetrachloroethylene, or chlorobenzene. The photoluminescence was measured at room temperature for Ag_2Te nanoparticles before and after the cation exchange. The Ag_2Te nanoparticles do not have an infrared absorption or emission in the spectral range from 1000-7000 cm^{-1} as shown in the photoluminescence spectrum of Fig. 3-2(a). However, following the cation exchange step, the newly formed colloidal solution is clearly HgTe CQDs that indeed have an

infrared absorption and emission. The broad emission of the HgTe CQDs is from the polydispersity of the Ag_2Te nanoparticles that contributes to the polydispersity following the cation exchange.

A limiting factor of the solution phase cation exchange process is the quality of the thin films, which were often grainy and non-uniform due to the poor colloidal stability. Therefore, an investigation of the electrical properties of solution phase cation exchange Ag_2Te-HgTe nanoparticles was not conducted. For a thin film photodetector, the quality of the film can significantly affect the performance due to defects, variations in the film thickness, and electrical shorting through cracks in the film. To overcome this limitation, films of Ag_2Te nanoparticles were first deposited by spin-coating and then the cation exchange with $HgCl_2$ was performed. In this way, the Ag dopants were first introduced in the solid phase through the Ag_2Te nanoparticles, and then the diffusion process was initiated and governed by the cation exchange. The Ag_2Te nanoparticles were cleaned and solvated in a mixture of 9:1 hexane:octane, which was then used to spin-coat films at ~2000 rpm for 30 seconds. The solid thin film of Ag_2Te nanoparticles was then exposed to a 10 mM $HgCl_2$ methanolic solution to perform the solid-state cation exchange.

The conversion of the Ag_2Te nanoparticle film to HgTe was first confirmed by measuring the FTIR absorption spectrum of the film before and after the $HgCl_2$ exposure. In the infrared region from 1000-7000 cm^{-1}, Ag_2Te nanoparticles are not absorbing while HgTe CQDs have a strong infrared absorption as shown in Fig. 3-2(b). The increase in absorption over this spectral range is a strong indicator of the conversion of Ag_2Te to HgTe by the $HgCl_2$ exposure. Again, the broad absorption edge of the HgTe CQD spectrum is due to the polydispersity beginning with the Ag_2Te nanoparticles. By comparing the absorption spectrum of the film to the emission spectrum

of the solution phase exchange, the solid-state cation exchange indeed converts the Ag_2Te nanoparticles to HgTe CQDs. The broad emission follows well with the broad absorption edge observed in the cation-exchanged thin films.

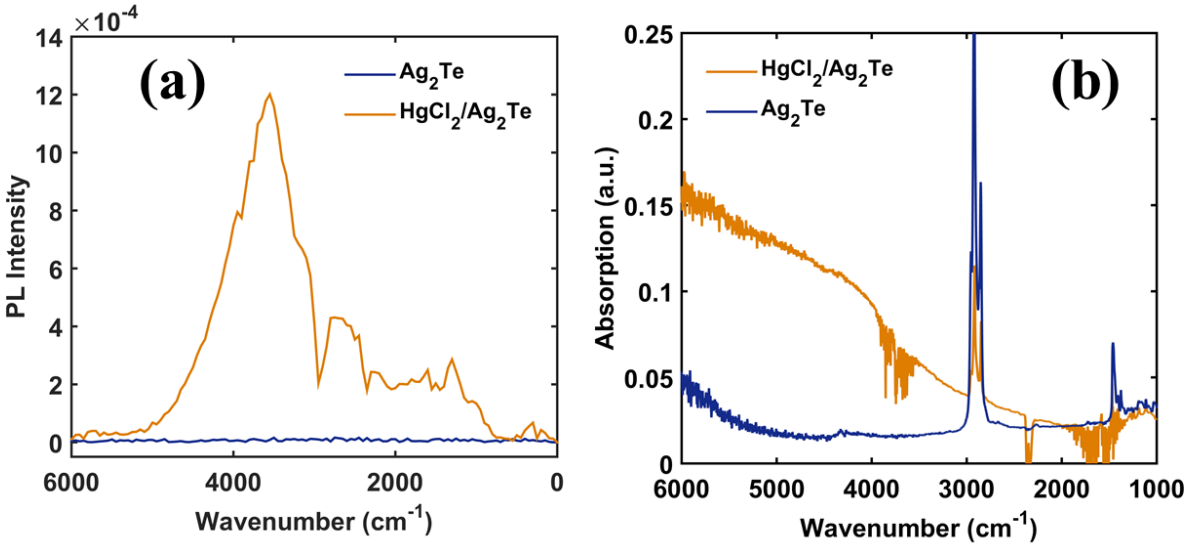

Figure 3-2 (a) *Photoluminescence and* ***(b)*** *FTIR absorption spectrum of Ag_2Te nanoparticle film before and after soaking in $HgCl_2$ methanol solution.*

The absorption and photoluminescence are simple probes for assessing the cation exchange process. However, the question remains whether Ag ions are present in the CQD films and how they are distributed as dopants. To test for the presence of Ag and the speciation in the CQD film, the elemental composition of the films was measured by x-ray photoelectron spectroscopy (XPS). Fig. 3-3 shows the high-resolution peaks for Hg, Te, and Ag for films of Ag_2Te nanoparticles before and after cation exchange. The Te peak energy shifts from 572.3 eV before to 572.9 eV after the $HgCl_2$ treatment, which is attributed to the change from an interaction with Ag to Hg. The Ag3d peaks shifted from 368.1 eV and 374.1eV to 367.6 eV and 373.6 eV, respectively, which is attributed to the likely formation AgCl during the exchange process. Importantly, the shape of the

Ag peak is sharp, in contrast to the broad and asymmetric peaks of metals, which indicates Ag as an ion in the thin film. Most notable is the strong increase in the intensity of the Hg4f peaks at 100.6 eV and 104.6 eV. For $HgCl_2$, the expected peak position is 101.4 eV; therefore, the peaks here are assigned to the formation of HgTe. The broad survey spectrum is shown in Fig. 3-3(d), which also shows the presence of a Cl peak and indicates the retention of Cl atoms in the film. From the XPS measurement, the calculated atomic ratio is ~4:4:1:1 Ag:Cl:Hg:Te. Both Ag:Cl and Hg:Te are in 1:1 ratios and, with the previous results, suggests HgTe and AgCl species are present in the film after the cation exchange process. The higher fraction of Ag and Cl measured by XPS implies that much of the Ag species resides near the surface of the film.

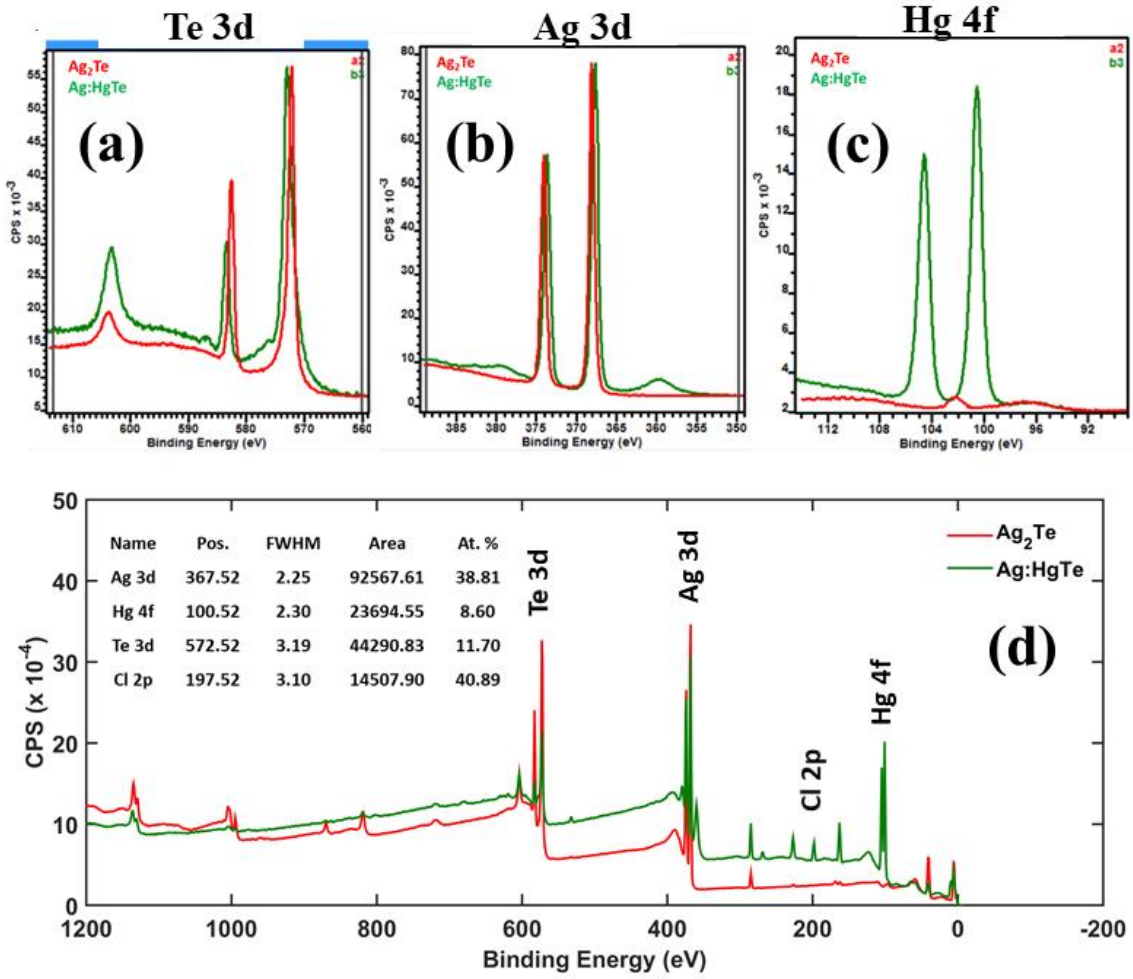

Figure 3-3 *X-ray photoelectron spectroscopy of Ag2Te nanoparticles before and after exposure to $HgCl_2$ methanol solution. High resolution XPS of* ***(a)*** *Te 3d peak,* ***(b)*** *Ag 3d peaks, and* ***(c)*** *Hg 4f peaks.* ***(d)*** *Low resolution XPS survey showing Te, Ag, Hg, and Cl peak positions. (Inset) Table of peak identity, position in eV, peak full width at half maximum, peak area, and atomic percent.*

The previous results support the interpretation that the solid-state cation exchange process does indeed convert the Ag_2Te to HgTe with Ag ions present in the film. Still, the distribution of the Ag ions in the film following the cation exchange process is not known. In a photodiode consisting of ITO/HgTe/$Ag_2Te(HgCl_2)$/Au, where $Ag_2Te(HgCl_2)$ indicates the solid-state cation exchange process, whether the Ag ions remain locally at the surface or diffuse into the film will

determine whether an abrupt or graded doping profile, respectively, forms. The type of doping profile can lead to differences in electrical behavior; therefore, understanding the form of the doping profile due to the solid-state cation exchange process can inform on future directions to improve the photodiode performance.

In bulk semiconductors, one technique for measuring the doping density profile is secondary ion mass spectrometry, or SIMS, which probes the ion concentrations as a function of the depth through the semiconductor device. Here, SIMS was performed by Nanolab Technologies, Inc. using a Cs ion beam on HgTe CQD photodiodes consisting of ITO/HgTe/Ag2Te/Au both with and without the solid-state cation exchange treatment. An important point here is that the concentrations of each element are not absolute and cannot be compared between different elements. However, the relative difference for the same element between samples is accurate and can be compared.

In both samples, shown in Fig. 3-4, the Ag distribution appears to have a graded or diffusion profile. Though such a profile might be expected due to the solid-state cation exchange process, it is not obvious that the untreated Ag_2Te nanoparticles should be distributed through the film. Upon further inspection, an accumulation of Ag at the ITO interface is observed. The accumulation is thought to be due to an induced migration of the Ag through the film during the SIMS depth profiling. Indeed, ion beam induced diffusion of Ag has been reported in organic optoelectronic devices to depend on the incident energy of the ion beam.[100] Therefore, this measurement artifact interferes with the determination of the Ag dopant profile and alternative approaches to definitively measure the doping profile will be required.

It was also observed from the SIMS measurement that (1) the Ag concentration decreased by approximately half following the solid-state cation exchange and (2) the concentration of chlorine increased uniformly throughout the HgTe CQD film. With regards to (1), the decrease in the Ag concentration implies some degree of solvation despite the presence of Cl thought to form AgCl. Understanding the origin of such an effect may lead to small but tunable changes in the Ag doping density at the photodiode junction. From (2), the Cl may do more than bind up the Ag to form AgCl. In Pb chalcogenides, Cl at the CQD surface was shown to effectively reduce oxidation[100] and extend the operational lifetime of photovoltaics.[101] Passivation of the HgTe CQD film here by Cl could contribute to the increase reliability of the devices described in the following section.

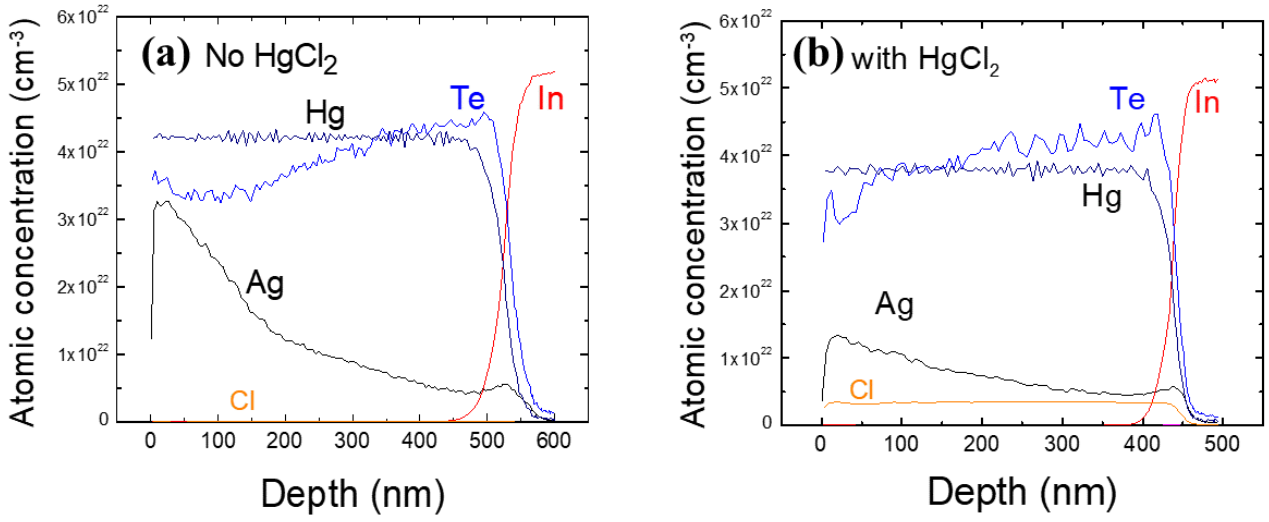

Figure 3-4 *Secondary ion mass spectrometry of HgTe CQD photodiodes ITO/HgTe/Ag_2Te/Au both* ***(a)*** *without and* ***(b)*** *with the $HgCl_2$ methanol solid state cation exchange. The concentrations of each element are relative to a reference indium concentration.*

In conclusion, the solid-state cation exchange converts the Ag_2Te nanoparticle film into a film of HgTe CQDs, which is supported by measurements of the absorption and

photoluminescence before and after cation exchange. From XPS, the Ag remains in the film as Ag^+ ions and most likely as the AgCl species. SIMS measurements were performed to determine the doping density profile of the Ag in the film; however, artifacts in the measurement prevent a definitive description of the doping profile. The results presented in this section provide insights into the Ag concentration and distribution in the HgTe CQD films. However, whether the Ag dopants are electrically active remains to be determined. In the next section, the characteristics and figures-of-merit for photodiodes fabricated using the solid-state cation exchange process are presented. There, a conclusion on the electrical nature of the Ag ions in the HgTe CQD films is provided in the discussion of the photodiode device physics.

3.2 Characteristics of the mid-wave HgTe CQD photodiode

This section describes characteristics and physical properties of the mid-wave infrared HgTe colloidal quantum dot photodiodes fabricated with the solid-state cation exchange as described in the previous section. The figures-of-merit are reported and compared to previous device iterations to highlight the improvement due to the solid-state cation exchange. Several experiments and results are discussed to provide some insights into the physics of the photodiodes. A final comment on the takeaways from these experiments is provided to summarize the findings and motivate future directions for improvement.

The HgTe CQD photodiodes consisted of ITO/HgTe/$Ag_2Te(HgCl_2)$/Au wherein the solid state cation exchange was performed by exposing the Ag_2Te nanoparticle film was to a solution of $HgCl_2$ in methanol. The film of HgTe was prepared by dropcasting at 40^{o}C, layer-by-layer, HgTe CQDs from chlorobenzene and crosslinking each layer with a mixture of 1,2-

ethanedithiol(EdT) and hydrochloric acid (HCl) in isopropanol (IPA) at a 1:1:20 ratio by volume. The final thickness of the HgTe CQDs was ~400 nm after 5-7 cycles of dropcasting and crosslinking. The Ag_2Te nanoparticles were spin-coated at 2000 rpm for 30 seconds from a solution consisting of 9:1 hexane:octane by volume. Two layers are spin-coated, and each layer was treated with 10 mM $HgCl_2$ at room temperature for 10 seconds followed by rinsing with IPA. Then, each layer was crosslinked with EdT in IPA (2% by volume) and rinsed with IPA. The Au film thickness was typically 20 nm and formed by electron beam evaporation under a vacuum of 10^{-8} Torr through a shadow mask. A cartoon representative of the photodiode structure is provided in Fig. 3-5(a) alongside a cross-sectional scanning electron microscope image of an actual photodiode in Fig. 3-5(b), indicating the ITO and CQD film with an approximate thickness of 400 nm.

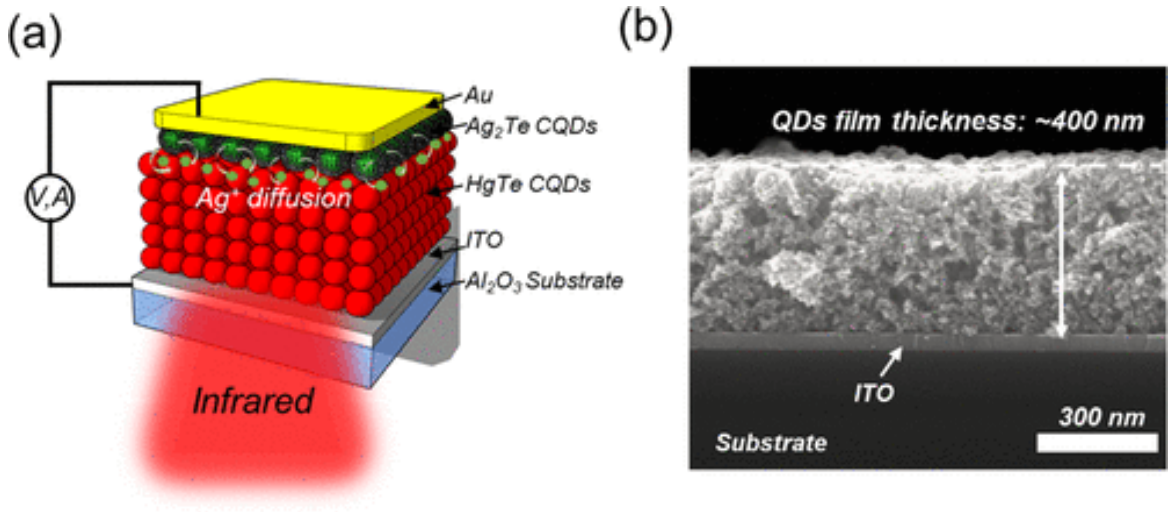

Figure 3-5 (a) *Cartoon and* ***(b)*** *cross-sectional SEM of the HgTe CQD photodiode.*

The concentration of the Ag_2Te nanoparticle solution was evaluated to optimize the photodiode performance. The number of layers spin-coated was kept to two while the

concentration of Ag_2Te nanoparticles in solution was either 3.125 mg/mL, 6.25 mg/mL, or 12.5 mg/mL. The responsivity of the photodiode at 80 K was measured and compared for each concentration of Ag_2Te nanoparticles as shown in Fig. 3-6. A maximum in the responsivity occurs for concentrations between 6-7 mg/mL and is optimal for the operation of the photodiode.

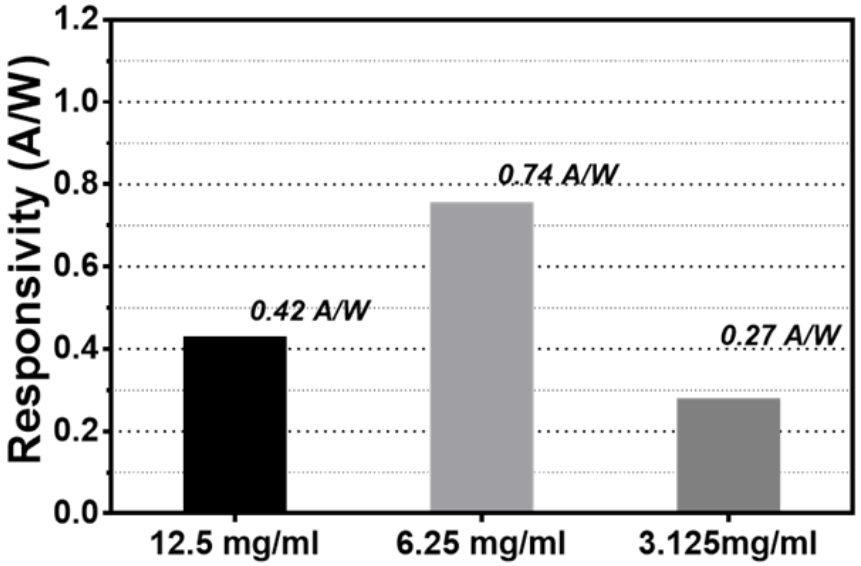

Figure 3-6 *Ag_2Te concentration dependence of the photodiode responsivity at 80 K following solid-state cation exchange.*

At the optimal concentration, it is evident from the strong rectification of the photodiode at 80 K, shown in Fig. 3-7(a), that the solid-state cation exchange leads to a strong photovoltaic effect and rectifying space-charge region in the HgTe CQD photodiode. The photodiode had a shunt resistance of 300 kΩ, series resistance of 400 Ω, an open-circuit voltage of 80 mV, and a short-circuit current density of 3.5 mA/cm^2. In comparison with the photodetectors described in Chapter 2, the electrical behavior here is a significant improvement over all characteristics of the device. Additionally, the electrical behavior was highly reproducible and, at the time of writing

this thesis, remains to be the most reliable method for fabricating rectifying HgTe CQD photodiodes. The spectral response of the photodiode is shown in Fig. 3-7(b) with a 50% detection cutoff of ~4 µm at room temperature and extending out to 5 µm at 85 K.

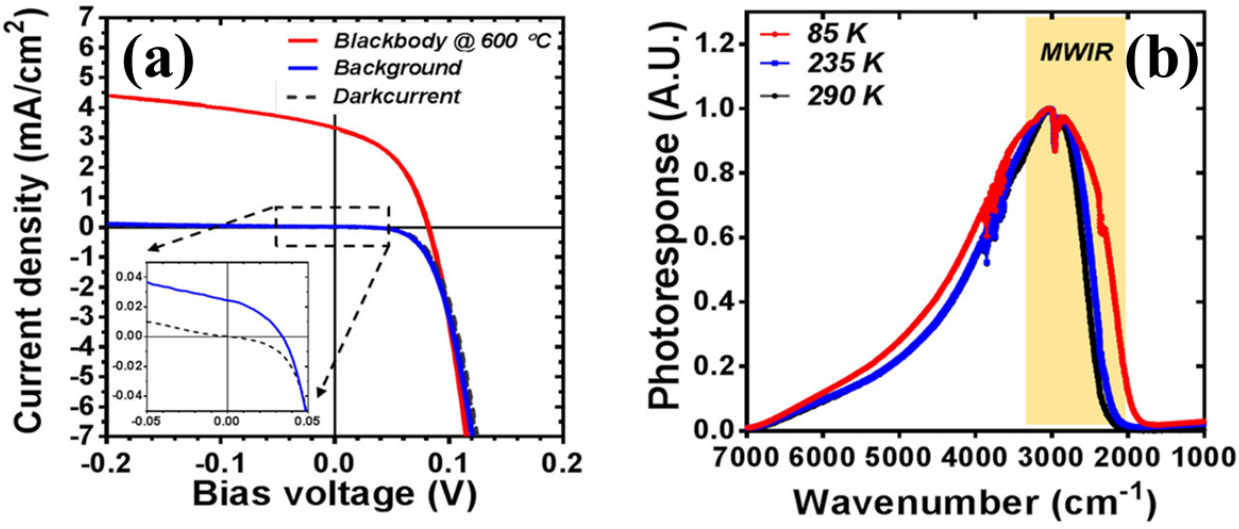

Figure 3-7 (a) *Current density-voltage (JV) behavior of the HgTe CQD photodiode with $HgCl_2$ solid-state cation exchange. (Inset) JV behavior of dark current density (dashed black) and background photocurrent density(solid blue).* ***(b)*** *Blackbody spectral response measured as a function of temperature. The highlighted region indicates the mid-wave infrared (MWIR) spectral region.*

A comparison of the responsivity between devices consisting of CaF_2/NiCr/HgTe/Ag_2Te(EdT)/Ag paint,[43] ITO/HgTe/Ag_2Te(EdT)/Au, and ITO/HgTe/$Ag_2Te(HgCl_2)$/Au is shown in Fig. 3-8(a). In the devices consisting of Ag_2Te(EdT), the Ag_2Te nanoparticle film did *not* undergo a solid-state cation exchange process and remains as Ag_2Te. Devices where the solid-state cation exchange process was used are indicated by the label $Ag_2Te(HgCl_2)$ to assign the use of $HgCl_2$ in the fabrication of the photodiode. It is evident from the responsivity that the $HgCl_2$ solid-state cation exchange process further improves current collection efficiency by more than 10-fold at the 160 K peak response and more than 7-fold

improvement at operating temperatures near 80 K in comparison with the reported CaF_2/NiCr/HgTe/Ag_2Te(EdT)/Ag paint photodiode. While the photodiodes with Ag_2Te(EdT) layers showed some improvement, the device performance was highly variable from Ohmic to insulating.

The improvement in the rectification and responsivity led to an increase in the specific detectivity, D^*, at all temperatures as shown in Fig. 3-8(b). Below 150 K, the photodiodes demonstrated background-limited infrared photodetection (BLIP), *i.e.* the noise and sensitivity of the photodetector is limited by the 300 K ambient background flux. The most significant improvement, and important for the future of high-operating temperature photodetectors, is at temperatures greater than 150 K where the D^* improved by 30-fold. It is apparent then that the solid-state cation exchange with Ag_2Te and $HgCl_2$ is a key development in the advancement of the HgTe CQD-based infrared photodetector.

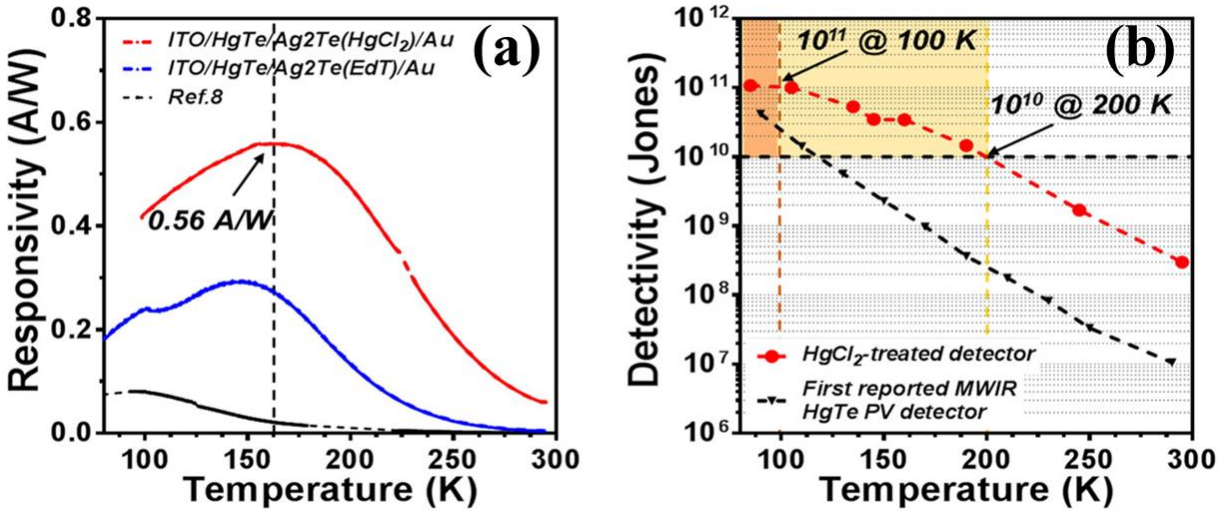

Figure 3-8 (a) *Responsivity and* ***(b)*** *specific detectivity comparison of the $HgCl_2$ exchanged photodiode to the untreated photodiode and the NiCr/HgTe/Ag_2Te/Ag paint photodiode reported by Guyot-Sionnest and Roberts.*[43]

Further development of the HgTe CQD photodiodes will come with a better understanding of the device physics. To begin, the temperature dependence of the photodiode dark current and noise current density is useful to both identify the underlying phenomenon that limits the detector sensitivity and to predict the operating temperature required for a given sensitivity. Fig. 3-9 shows the Arrhenius plot of the R_0A product and the activation energy is fit to the high-temperature data. The activation energy of the R_0A product increased from ~75 meV to ~145 meV, nearly doubling with the use of the $HgCl_2$ solid-state cation exchange process. For a HgTe CQD with optical absorption near 4.5 µm, the band gap energy is ~ 300 meV and the activation energy corresponds to half the band gap. An ideal semiconductor photodiode would be radiatively limited, *i.e.* radiative recombination is the dominant process, and have an activation energy equivalent to the semiconductor band gap.[102] Here, a value less than the band gap indicates non-radiative recombination processes dominate the noise current density and sensitivity of the photodiode.

However, an exact mechanism for the recombination cannot be determined from this information alone. To realize the radiative limit for HgTe CQDs will require a concerted effort to improve the photoluminescence quantum yield (*i.e.* reduce the non-radiative rate due to ligands and defects) and retain the desirable transport properties of the CQD films. Designing a photodiode with lower noise and a stronger temperature dependence of the noise generation process will yield better D^* at higher operating temperatures important for the development of emerging MWIR detectors.

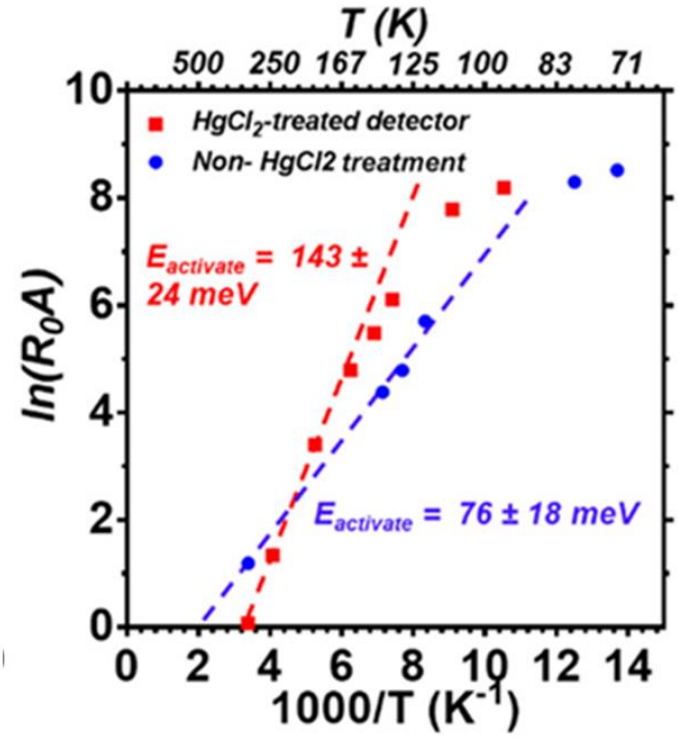

Figure 3-9 *Arrhenius plot of the R_0A product for the untreated and $HgCl_2$ solid-state exchange HgTe CQD photodiode with dashed lines indicating fit with an activation energy of 76 meV and 143 meV, respectively.*

The electrostatics of the photodiode were investigated by measuring the capacitance-voltage behavior and performing a Mott-Schottky analysis to estimate the doping density,

depletion region width, and build in potential of the HgTe CQD photodiode. To begin, the capacitance was measured for the HgTe CQD photodiodes at 80 K by applying a 10 mV AC current to the photodiode for a range of frequencies between 1-20 kHz at a reverse bias between 0-100 mV. Fig. 3-10(a) shows the frequency dependence of the AC current at each reverse bias voltage. From the intercept, the capacitance was calculated by assuming a simple capacitor-resistor model where the current is expressed as in Eq. (3.3).

$$|i| = \sqrt{(\omega C)^2 + \left(\frac{1}{R}\right)^2}\,|V| \tag{3.3}$$

In Eq. (3.3), ω is the AC frequency, C is the capacitance, R is the resistance, V is the AC voltage, and i is the current. In the limit that ωC > 1/R, then the capacitance can be calculated from the slope of the current versus AC frequency. Such a linear dependence is observed for frequencies between 10-20 kHz in Fig. 3-10(a). The diode internal resistance is also calculated from Eq. (3.3) by extrapolating to the DC current value at the 0 Hz y-intercept. Fig. 3-10(c) shows the reverse bias dependence of the photodiode shunt resistance. The zero-bias shunt resistance agrees with the value of 300 kΩ previously measured by the JV behavior.

In a diode, the application of a reverse bias increases the depletion width in response to the external potential and, thus, decreases the capacitance. The reverse bias dependence of the capacitance is summarized in Fig. 3-10(b). From the zero-bias capacitance, the depletion width, d, can be estimated under the assumption of a parallel plate capacitor model such that $d = \epsilon\epsilon_0 A/C$. Then, for a device area of 0.6 mm^2, a dielectric constant of HgTe CQD films ~6, and a capacitance of 230 pF, the equilibrium depletion width is ~140 nm. Given the film thickness is between 400-

500 nm, the depletion width is only a fraction of the total thickness. Assuming carriers generated in the depletion region are swept out before recombining, transport and carrier collection efficiency would be limited by the diffusion length of charge carriers. At high temperatures the diffusion length is on the order of 10 nm to 100 nm, which is much shorter than the neutral region widths given by the difference in film thickness and depletion width. This short diffusion length then limits the device efficiency. A depleted photodiode, *i.e.* a photodiode where the depletion width is the thickness of the device, might have greater efficiency at higher operating temperatures as the current would no longer be limited by the diffusion length of the carriers in the neutral regions.

Finally, to determine the doping of the semiconductor, the capacitance-voltage behavior is presented in a Mott-Schottky plot of the $1/C^2$ dependence on external bias, as shown in Fig. 3-10(d). Under the assumption of an abrupt junction diode, the capacitance is related to the external bias by Eq. (3.4),[42]

$$\frac{1}{C^2} = \frac{2}{\epsilon\epsilon_0 qNA^2}(V_{bi} - V_{ext}) \tag{3.4}$$

where N is the effective carrier density, A is the photodiode area, V_{bi} is the built-in potential, and V_{ext} is the applied external potential where external voltages less than zero indicate operation in reverse bias. An abrupt junction is one between a heavily doped semiconductor and a lightly doped semiconductor. In this case, the space charge region is predominantly in the lightly doped semiconductor and a change in the capacitance, which is inversely proportional to a change of the depletion width, will depend only on the charge density of the lightly doped region. In Eq. (3.4), the doping density distribution is also assumed to be constant in the abrupt junction diode. Then, N can be calculated from the slope of the Mott-Schottky plot, while the built-in potential can be

determined by extrapolating to the voltage at which $1/C^2$ goes to zero. From the x-intercept, the V_{BI} is ~ 80 mV and nearly equivalent to the open-circuit voltage at 80 K. From the slope and with values of $\epsilon \sim 6$ and A of 0.6 mm^2, the effective carrier density was ~2.5×10^{15} cm^{-3}. The carrier density most likely corresponds to the EdT/HCl-treated HgTe CQD layer in the photodiode away from the Ag_2Te nanoparticle layer. Note here that the bias dependence of $1/C^2$ in Fig. 3-10(d) is indeed linear at the small voltages measured, in agreement with the assumption of a constant doping density in an abrupt junction diode.

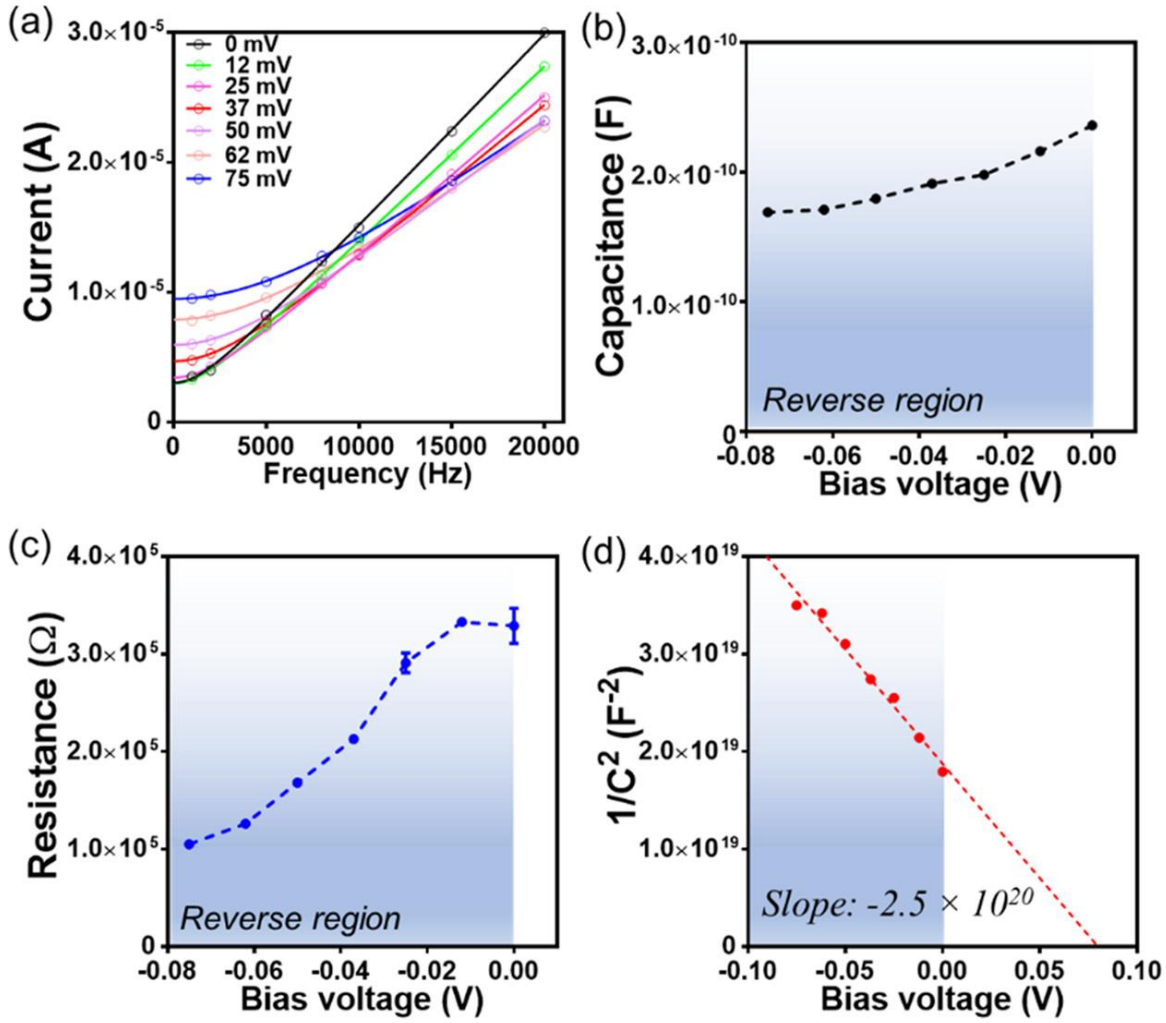

Figure 3-10 (a) *Frequency dependence of the current for the HgTe CQD photodiode operating under a reverse bias between 0 mV and 100 mV.* ***(b)*** *Reverse bias dependence of the photodiode capacitance.* ***(c)*** *Reverse bias dependence of the photodiode resistance.* ***(d)*** *Mott-Schottky plot of the bias-dependent capacitance for the $HgCl_2$ solid state exchange HgTe CQD photodiode.*

A rough picture of the photodiode can now be composed wherein the junction is assumed to be abrupt with a lightly doped region of doping density 2.5×10^{15} cm^{-3} and heavily p-type region doped with Ag. The linear trend in the Mott-Schottky plot implies the HgTe CQD photodiode is an abrupt junction diode, and this interpretation is further supported by the increased Ag

concentration at the surface measured by XPS (see Section 3.2). The MWIR HgTe CQD photodiode has a depletion width of ~140 nm and a built-in potential of ~80 mV.

In conclusion, HgTe CQD photodiodes for mid-wave infrared photodetection were realized using a solid-state cation exchange process to extrinsically dope HgTe CQD films. The performance of the photodiode, resulting from the cation exchange step, surpasses the previously reported responsivity by 10-fold and specific detectivity by 30-fold with significant gains for high temperature operation. The sensitivity of the photodiode is limited by an ~$E_g/2$ recombination process of unknown origin. A preliminary description of the photodiode was given using the results from the capacitance-voltage behavior and Mott-Schottky analysis. The photodiode possibly consists of an abrupt junction between a lightly-doped HgTe CQD film and an extrinsic, heavily Ag-doped p^+-type HgTe CQD layer. Of course, the analysis of the doping profile begins with the assumption of a one-sided diode, and further investigation into the doping profile will be required to complete an accurate description of the HgTe CQD photodiode. A more complete picture of the doping and mechanism involved would not only lead to optimized infrared photodetection but also to concepts for other HgTe CQD optoelectronics.

3.3 Optical enhancement and thermal imaging

This section demonstrates one method in the strategy to improve the photodiode performance and operating temperature for applications in photodetection and imaging. Optical enhancement of the photodiode performance with plasmonic discs and a Fabry-Perot cavity is described, and the outcome is compared with a reference photodiode in terms of figures-of-merit. Proof-of-concept infrared images were taken with the optically enhanced photodiode and a

calculation of the minimum achievable thermal resolution at 80 K was made. The infrared images shown here motivate the next stage of development, *i.e.* making a focal plane array with HgTe colloidal quantum dot photodiodes for thermal imaging applications. Section 3.4 is reproduced in part with permission from Tang, X.; Ackerman, M. M.; Guyot-Sionnest, P. Thermal Imaging with Plasmon Resonance Enhanced HgTe Colloidal Quantum Dot Photovoltaic Devices. *ACS Nano* **2018** *12* (7), 7362-7370. Copyright 2018 American Chemical Society.

To improve the performance of the HgTe CQD photodiodes will require (1) reducing the non-radiative rate of the HgTe CQDs (*i.e.* increasing the photoluminescence quantum yield), (2) increasing the mobility for enhanced carrier collection efficiency, and (3) increasing the absorption of light in the thin film active region of the photodiode. While (1) and (2) are more challenging and require advances in the chemistry of the HgTe CQDs, methods for (3) are engineering challenges and follow immediately from literature on other thin film optoelectronics. Therefore, the first step to improving the HgTe CQD photodiode was to address the low absorption of light in the thin films by integrating plasmonic and interference structures.

In other CQD thin films, the absorption has been enhanced by nanostructuring the CQD surface,[103] integrated gratings into the film,[104] and with the use of optical nanoantennas.[105] Here, plasmonic microstructures and a Fabry-Perot cavity were integrated into the photodiode fabrication process and were shown to enhance the absorption in the HgTe CQD film as measured by an increase in the photodiode responsivity at 80 K. Fig. 3-11(a) shows a cartoon of the optically-enhanced HgTe CQD photodiode that consists of a plasmonic disc array at the ITO electrode and a Fabry-Perot cavity atop the completed photodiode stack. the photodiode was backside

illuminated, *i.e.* through the sapphire/ITO substrate, and Au electrode at the HgTe interface was kept thin to allow light to pass into the Fabry-Perot cavity. The conductivity of the Au electrode was maintained by sputtering additional ITO onto the 5-nm Au electrode, which also acted as a protective layer for the HgTe CQD during the ITO sputtering process step. Fig. 3-11(b) shows a cross-sectional SEM image of the completed optically-enhanced photodiode stack.

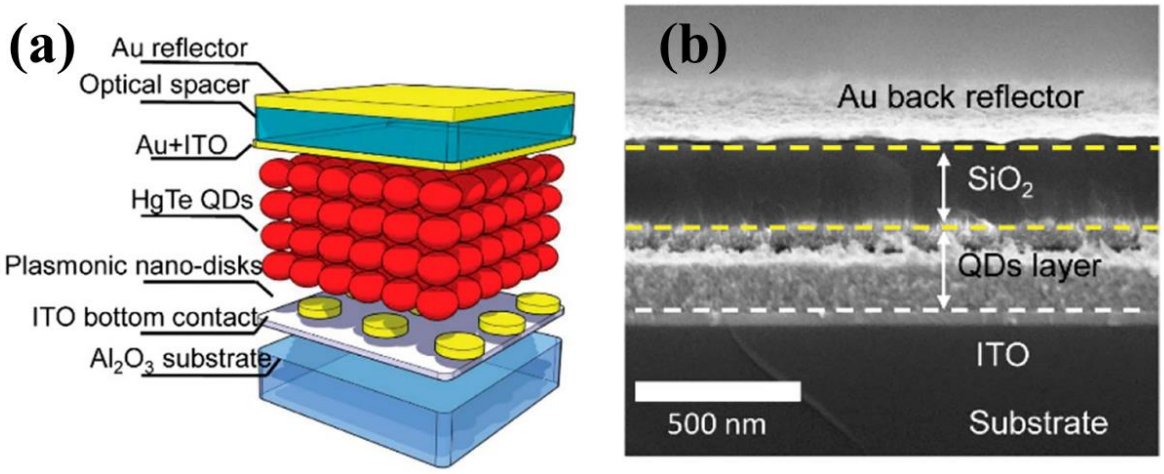

Figure 3-11 (a) *Cartoon and* ***(b)*** *cross-sectional SEM image of the optically-enhanced HgTe CQD photodiode.*

The enhancement of the absorption due to the optical cavity and the plasmonic disc array was simulated with COMSOL Multiphysics®, and an predicts an increase from ~15% to 80% absorption, shown in Fig. 3-12(a), when the cavity and the plasmonic disc array are both integrated into the photodiode. The spectral responses of a photodiode without enhancement and with the integrated optical enhancement structures are shown in Fig. 3-12(b) and demonstrates a 4-fold enhancement at the peak response due to the increased coupling of the light into the thin film. This corresponds to an EQE of ~45% and a significant improvement in the absorption of light by the HgTe thin film. The enhancement is largest at the wavelengths where the cavity and plasmonic

modes overlap, and the spectral peak can be tuned by adjusting the dimensions of the plasmonic array and thickness of the optical spacer. The capability to integrate spectral filters with enhanced peak responsivity is important in hyperspectral sensing applications.[106] The improvement in responsivity resulted in a 2-fold increase in the specific detectivity at all operating temperatures as shown in Fig 3-12(c). Such an enhancement in specific detectivity also corresponds to ~25 K increase in the operating temperature of a photodiode with the same sensitivity, bringing HgTe CQD detectors closer to operation with low-cost, low-power thermoelectric cooling.

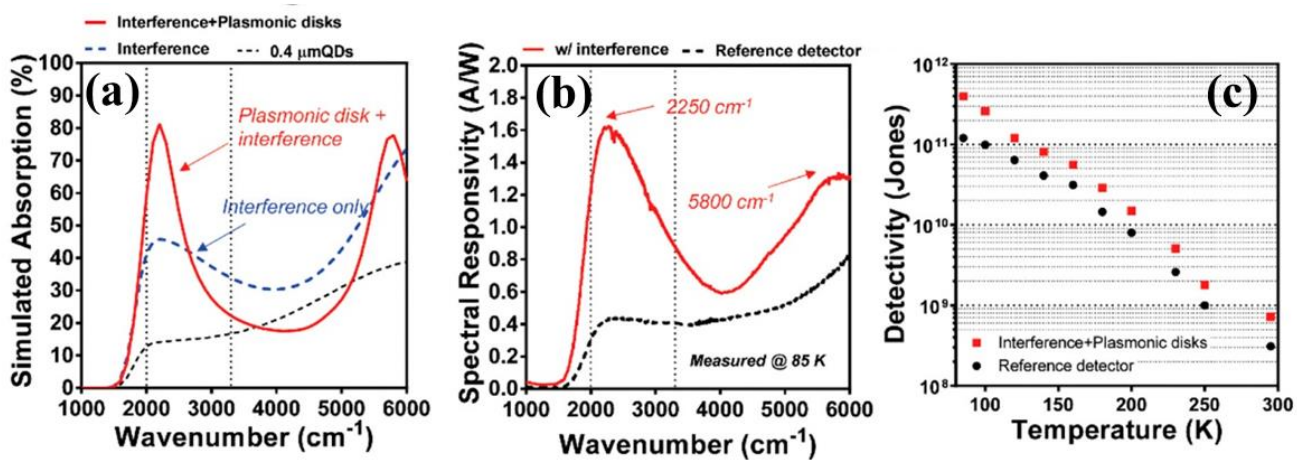

Figure 3-12 (a) *Simulated absorption for HgTe CQD photodiode without any optical structure, with only the Fabry-Perot cavity, and with both the cavity and plasmonic disk array structure integrated.* ***(b)*** *Measured spectral response at 80 K, comparing the photodiode without optical structures to the optically-enhanced photodiode with peaks consistent in the response with the simulated absorption.* ***(c)*** *Temperature dependence of the specific detectivity for both a reference and optically-enhanced photodiode.*

Finally, imaging with the HgTe CQD photodiode was demonstrated using a simple single-pixel, single-lens setup as shown in Fig. 3-13(a). A single photodiode element was placed behind a ZnSe lens that was rastered both horizontally and vertically to focus the image onto the photodiode. At each coordinate, the current is measured and the data set is processed through a

data acquisition system to compose an image. Fig. 3-13(b) shows a thermal image captured with a HgTe CQD photodiode and demonstrates the minimum quality of image that can be obtained when operating at 80 K. From the image, the features of the face and hand can be resolved, and the glasses appear dark as glass is opaque to mid-wave infrared light.

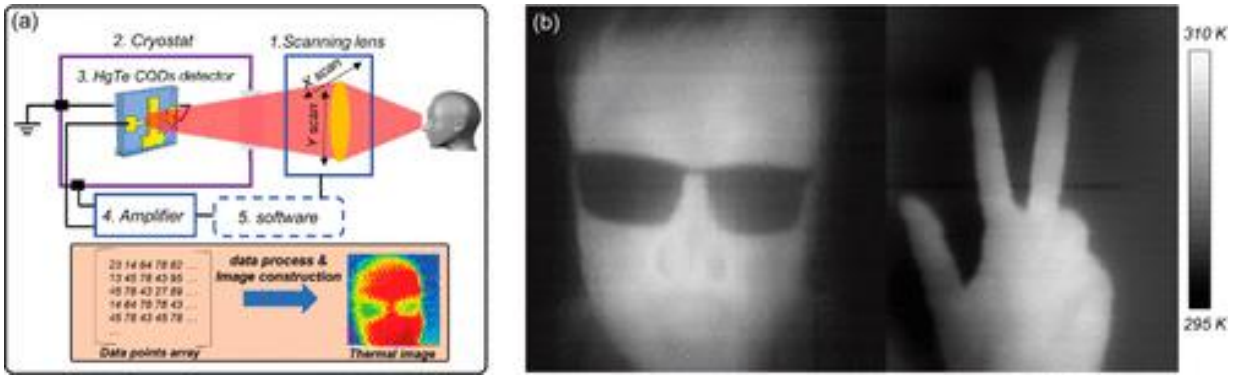

Figure 3-13 (a) *Box diagram of the single-pixel imaging system used to demonstrate infrared imaging.* ***(b)*** *Infrared image captured using the single-pixel imaging system with the HgTe photodiode operating at 80 K.*

In thermal imaging, both spatial and thermal resolution are important for obtaining high quality information about the differences in temperatures in a scene. A simple measure of the maximum thermal resolution obtainable with a HgTe CQD photodiode operating at 80 K was measured by imaging a Peltier cooler as shown in Fig. 3-14(a). The difference in the temperature was set and measured to be 15ºC, and Fig. 3-14(b) shows the current difference through a line in the scene. The NEDT is then calculated according to Eq. (3.5)

$$NEDT = \frac{\Delta T}{\Delta I_s / I_n} \tag{3.5}$$

where ΔT is the temperature difference in the scene, ΔI_s is the signal difference due to the emission from the hot and cold sources, and I_n is the noise current. The NEDT also depends on the frame

rate and F/# used to capture the image, which were an effective rate of 1 kHz and *f*/1.3, respectively. At the current F/# and frame rate, the maximum NEDT value is 14 mK and on par with the best thermal cameras that can achieve between 10-50 mK. Fig. 3-14(c) and (d) show the contrast image and false-color image, respectively, of the Peltier cooler. Notably, the thermal resolution is high enough such that the current-carrying wires can be resolved against the 300 K background. Though preliminary, the results presented here are promising for the future of infrared detection and imaging with HgTe CQD photodiodes.

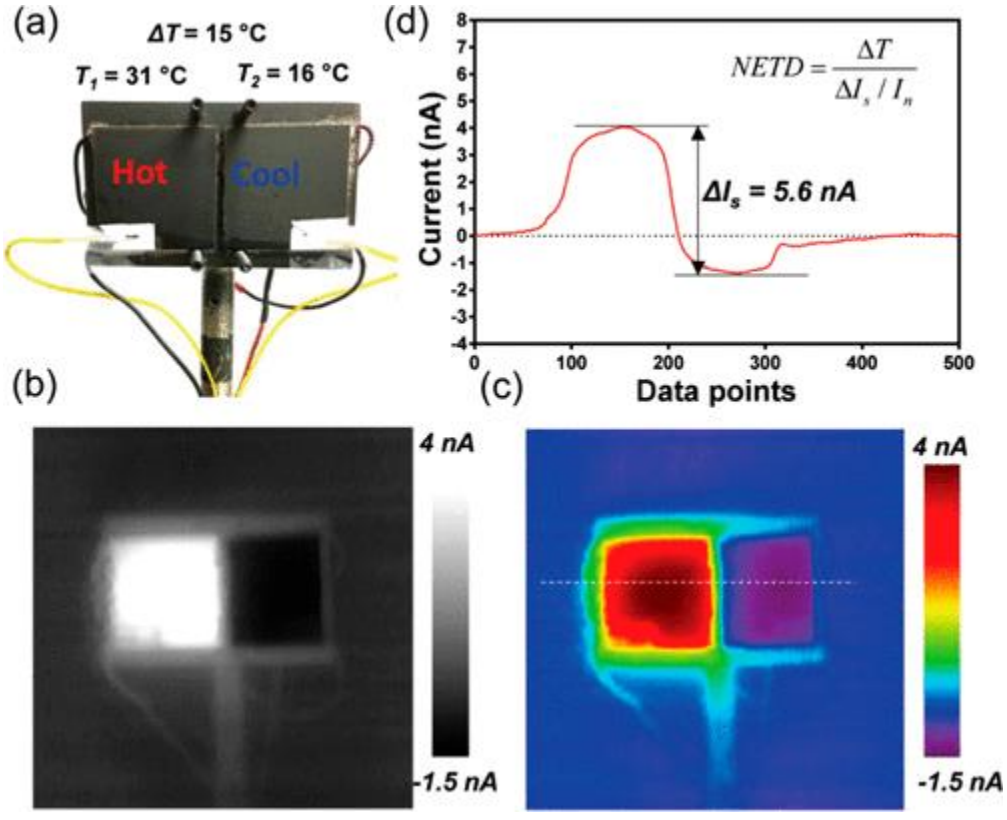

Figure 3-14 (a) *Setup of Peltier coolers used to measure the NEDT.* ***(b)*** *Line scan current profile of the Peltier coolers, indicating the current difference from hot to cold.* ***(c)*** *gray-scale and* ***(d)*** *false-color image of the Peltier cooler captured with the single-pixel imaging system. The current is scaled with respect to the magnitude of the background current.*

3.4 Summary

A solid-state cation exchange processing step was introduced to the fabrication of the mid-wave infrared HgTe CQD photodiode. The solid-state cation exchange process consisted of first spin-coating a thin film of Ag_2Te nanoparticles onto a HgTe CQD film. Second, the film was exposed a 10 mM $HgCl_2$ to convert the Ag_2Te nanoparticle layer into a HgTe thin film that contains Ag ions acting as dopants. The solid-state cation exchange process was evaluated using infrared spectroscopy, x-ray photoelectron spectroscopy, and dynamic secondary ion mass spectrometry to determine the speciation and Ag distribution in the thin film. Infrared spectroscopy and x-ray photoelectron spectroscopy support the claim that the film indeed converts from Ag_2Te to HgTe with Ag, possibly as AgCl, remains near the surface of the film. The open-circuit voltage and capacitance-voltage behavior further supports the assumption of an abrupt junction with estimates of the doping densities to be 2.5×10^{15} cm^{-3} and 8×10^{19} cm^{-3} for the lightly and heavily doped regions, respectively. Photodiodes fabricated using the cation exchange process demonstrate the best MWIR specific detectivities, and optical enhancement further increased the high-operating temperature detection capabilities.

Chapter 4 Extended Shortwave Infrared Detection with HgTe Quantum Dots

The purpose of this chapter is to describe the development of the HgTe colloidal quantum dot extended shortwave infrared photodiode. The significance of the work described in this chapter is both an extension of the solid-state cation exchange doping to a different HgTe CQD photodiode and a demonstration of the relation between the HgTe CQD film photoluminescence to the photodiode figures-of-merit. First, a brief summary of the importance of the extended shortwave infrared and where HgTe CQDs potentially fit into the materials landscape is provided as context for the reader. Second, a method for improving the photoluminescence of small HgTe CQDs is introduced and the physical results are discussed in the context of a qualitative microscopic model. Finally, the characteristics of the extended shortwave infrared photodiode fabricated with the method for improving the photoluminescence are discussed in comparison with commercially available materials. A physical description of the photodiode noise and dark current density is discussed to provide insight toward future methods for improving the extended shortwave photodiode.

There is a growing interest in the commercial market for shortwave infrared photodetectors and imagers, but the adoption of the existing shortwave infrared technologies in emerging markets is restricted by high price. Motivated by the potential for inexpensive shortwave infrared photodetection with colloidal quantum dots, here the development of a HgTe colloidal quantum dot shortwave infrared detector is discussed. The discussion presented here is adapted from M. M. Ackerman, M. Chen, P. Guyot-Sionnest, “HgTe colloidal quantum dot photodiodes for extended short-wave infrared detection,” Appl. Phys. Lett. 116, 083502 (2020), with permission of AIP publishing.

4.1 Shortwave Infrared Photodetection and colloidal quantum dots

The purpose of this section is to provide a brief account of the materials and applications for extended shortwave infrared photodetection, and provide a context to the reader for why HgTe CQDs are an interesting semiconductor material for extended shortwave applications.

The shortwave infrared refers to the spectral region from 1-2.5 μm that is beyond the detection of silicon and limited by the atmospheric absorption due to water. For detection up to 1.7 μm, InGaAs is a semiconductor alloy most commonly used with a band gap of 0.75 eV for high-speed telecommunications and imaging for inspection and night vision applications. Beyond 1.7 microns, many applications of infrared sensing including gas detection and monitoring, enhanced night vision, spectroscopy, materials sorting, and art forensics would benefit from a readily available infrared imager. By increasing the indium content in the InGaAs alloy, the band gap of InGaAs can be tuned for detection beyond 1.7 μm. However, indium-rich InGaAs is no longer lattice matched to the underlying InP substrate for epitaxial growth. Consequently, photodetectors made with indium-rich InGaAs have higher dark currents due to the increased defect densities following from lattice mismatch during epitaxial growth.[107] An alternative semiconductor alloy, HgCdTe, can be tuned for absorption in the extended shortwave infrared from 2-3 microns easily by varying the ratio of Hg:Cd in the alloy without changing the lattice constant to maintain lattice matching to CdTe or ZnCdTe substrates for epitaxial growth. However, working with HgCdTe is still challenging given that the Hg-Te bonds are weaker and the material is more brittle. Another alternative for extended shortwave infrared photodetection is the type-II strained superlattice based on the III-V semiconductors InAs, AlSb, and GaSb recently reported.[108]

By comparison colloidal quantum dots (CQDs) are inexpensive to produce and the solution processability of the inks enables direct coating onto arbitrary substrates, including high-definition focal plane arrays for next-generation imaging. In 2007, Boberl *et al.* reported shortwave photodetection at 1.3 microns by inkjet printing aqueous HgTe colloidal quantum dot solutions onto interdigitated electrodes and demonstrated the possibility of shortwave detection with HgTe colloidal quantum dots.[109] Chen *et al*. spray-deposited aqueous HgTe colloidal quantum dots to fabricate shortwave infrared photoconductors with detection up to 1.4 microns. Chen *et al.* later integrated plasmonic Au nanorods into a photovoltaic vertically stacked shortwave infrared photodiode and showed the local field enhancement could improve the sensitivity for detection up to 1.4 microns.[110]

Today, PbS and HgTe CQDs are being developed as photoconductors,[66,111] photodiodes,[112–114] and phototransistors[115–117] for infrared detection. HgTe colloidal quantum dots are a strong candidate for extended shortwave infrared photodetection. The quantum confinement of HgTe results in a readily tunable band gap with the size of the quantum dots,[27] strong optical absorption,[118] and low Auger coefficients[29] that may lead to higher operating temperature infrared photodetectors.

In the following sections, the figures-of-merit are discussed with respect to the commercial HgCdTe and InGaAs extended shortwave infrared photodetectors. The recent contributions to the development of the extended shortwave infrared photodiode based on HgTe CQDs are informed, qualitatively, by a microscopic theory of defects or surface speciation and charge carrier trapping.

The discussion concludes with challenges to be addressed for proliferation of a HgTe colloidal quantum dot shortwave infrared photodetector array in the commercial market.

4.2 Improving photoluminescence of shortwave infrared HgTe quantum dots

The purpose of this section is to describe the observation and discuss the results related to the method for improving the HgTe CQDs photoluminescence. A qualitative model is introduced based on other II-VI and III-V colloidal quantum dots to motivate the use of $HgCl_2$ solution to modify the surface of the HgTe CQDs in a film. Experimental results are provided for the observed enhancement of the photoluminescence, and a discussion is given to attempt to explain the origin of the improved photoluminescence. In CQDs, the doping and mobility may change when the ligands on the surface change. Therefore, important for the photodiode, these properties of the HgTe CQD film with $HgCl_2$ were characterized and presented with a brief discussion of the results.

In a defect-free semiconductor colloidal quantum dot, the excitation of an electron-hole pair by incident light would subsequently lead to emission of light as the electron relaxes from the excited state to the ground state. However, surface defects can introduce inter-gap states that lead to non-radiative relaxation of the excited electron to the ground state. Then, no light is emitted as the electron relaxes through these mid-gap energy states. The quality of a semiconductor colloidal quantum dot is then measured by the photoluminescence quantum yield, the ratio of photons emitted to photons absorbed or as the ratio of the radiative rate to the total effective recombination rate. Increasing the photoluminescence quantum yield of infrared emitting quantum dots is an ongoing area of research and important to the application of HgTe CQDs for infrared photodetection.

For II-VI semiconductors, much work has focused on the use of core-shell nanocrystal structures to improve the photoluminescence. The growth of a nearly lattice-matched shell material to form a type-I heterostructure can both confine the electron and hole wavefunction to increase the probability of recombination as well as passivate surface defect states that lead to increased non-radiative recombination rates. More recent work has focused on the utility of Z-type ligands such as metal halides to passivate the surface defects and improve the photoluminescence, which is especially useful when shell materials are challenging to grow or cannot be used in devices, such as zero-bias operated photodiodes. For example, the use of Z-type ligands containing a metal ion (*e.g.* In^{3+}, Cd^{2+}) and a halide ion (*e.g.* Cl^{-}) were shown to improve the photoluminescence of II-VI CQDs such as CdTe, CdSe, and CdS and III-V CQDs like InP and In(Zn)P.[119]

Since the specific detectivity of a photodiode is directly related to the radiative fraction, *i.e.* quantum yield, of the semiconductor,[120] improving the photoluminescence is a primary objective for HgTe CQDs. Motivated by the use of the Z-type metal halide ligands to improve the quantum yield of other II-VI and III-V semiconductor CQDs, here a solution of $HgCl_2$ in methanol was introduced to the HgTe CQD films. After cleaning, films of HgTe CQDs were dropcast onto substrates to measure the photoluminescence. Then the film was treated with either $HgCl_2$ solution or the standard crosslinker EdT/HCl, and the relative intensity of the photoluminescence was compared, using an untreated film as a reference.

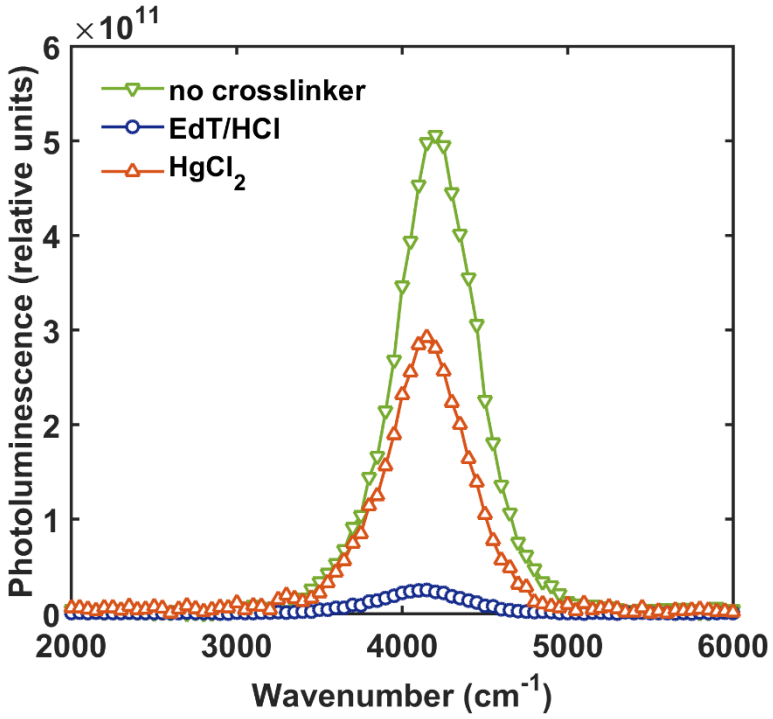

Figure 4-1 *Relative photoluminescence intensity of HgTe colloidal quantum dots treated with different ligand solutions.*

Fig. 4-1 shows the relative photoluminescence intensity for an untreated HgTe CQD film (green down-triangle), after treatment with a $HgCl_2$ ligand solution (orange up-triangle), and after treatment with an EdT/HCl crosslinker solution (blue circle). The intensity of the $HgCl_2$-treated film is 10-fold stronger than the EdT/HCl-treated film. Additionally, the $HgCl_2$-treated film was then exposed to the EdT/HCl crosslinking solution and the photoluminescence intensity was preserved. Improving the photoluminescence should improve the photodiode performance, as previously mentioned, and a photodiode fabricated with the $HgCl_2$ solution treatment was tested. A discussion of the characteristic photodiode performance follows in the next section.

The effect of the $HgCl_2$ solution was also investigated by electrochemistry to investigate the mobility and doping of the HgTe CQD following $HgCl_2$ treatment. The mobility and doping

of $HgCl_2$-treated and EdT/HCl-treated HgTe CQD films are shown in Fig. 4-2. From the electrochemical conductance, it is apparent that the Fermi level of the HgTe CQD film treated with $HgCl_2$ is much nearer the minimum of conductance, or intrinsic level, of the HgTe CQD film while the EdT/HCl-treated film has a Fermi level more toward the valence band and away from the center. From this it was determined that the $HgCl_2$ treatment decreased the doping level and made the HgTe CQD film more intrinsic. The mobility was only different by as much as 2-fold, decreasing slightly with the use of the $HgCl_2$ ligands. It is important that any treatment of the HgT CQD film that preserves or improves the photoluminescence also preserve or, ideally, improve the mobility to retain good transport of the charge carriers and high collection efficiencies. Again, given the small change in the mobility but 10-fold increase in photoluminescence, the performance of a photodiode treated with $HgCl_2$ is expected to be improved against a standard EdT/HCl-treated HgTe CQD photodiode.

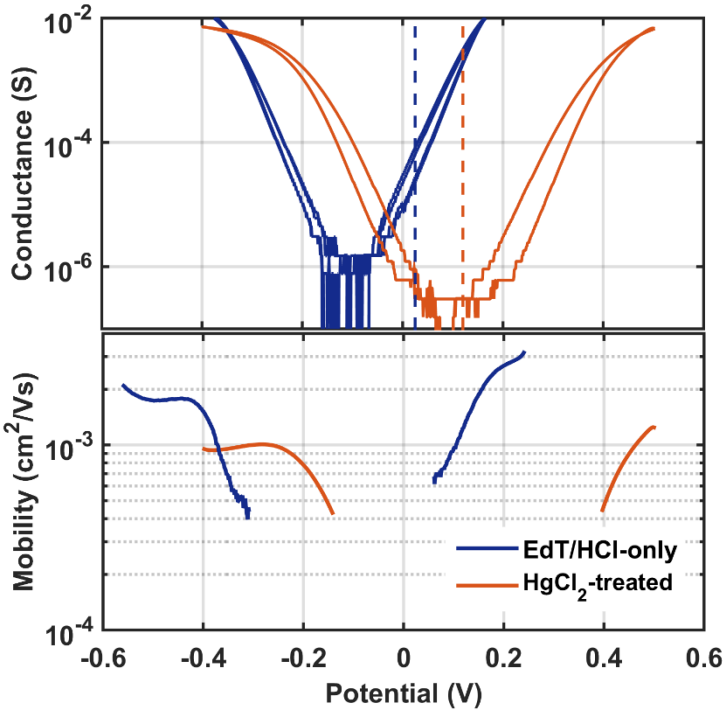

Figure 4-2 *Conductance* ***(top)*** *and mobility* ***(bottom)*** *measured by electrochemistry on HgTe CQD films.*

4.3 HgTe-based extended shortwave infrared photodiodes treated with $HgCl_2$ salts

The purpose of this section is the present the characteristics of the extended shortwave photodiode with and without the method for enhancing the photoluminescence. First, results on current rectification are presented and compared to explain why the $HgCl_2$ improved the photodiode performance. Then, additional investigation into the difference in physical properties due to the $HgCl_2$ are discussed. Insights from the discussion are summarized for the reader and used to inform on further future work.

Beginning with a sapphire/ITO substrate, HgTe CQDs were dropcasted at 40^{o}C from a mixture of 5:1 butyl acetate:chlorobenze solvent system. Each layer was then soaked in a 10 mM $HgCl_2$ methanolic solution for 10 seconds and rinsed with IPA. After the $HgCl_2$ exposure, the film

was then treated with EdT/HCl crosslinker for 10 seconds and rinsed with IPA. This process was repeated for 4-6 layers of HgTe CQDs to reach a final film thickness between 300-500 nm. To complete the photodiode, as with the mid-wave photodiodes described in Chapter 3, a thin Ag2Te nanoparticle layer was spin-coated and exposed to $HgCl_2$ in methanol (10 mM) for 10 seconds at 20^oC, rinsed with IPA, exposed to EdT/IPA for 10 seconds, rinsed, and dried with N_2 gas. This process was repeated a second time, and then a 50 nm Au electrode was evaporated through a shadow mask to pattern the ~1 mm^2 photodiode.

It is first worth noting that the spectrum of the HgTe CQDs is not significantly affected by the $HgCl_2$ exposure in the conditions used here. Conversely, using a large excess of $HgCl_2$ salt may lead to sintering of the HgTe CQDs and loss of the quantum confinement observed as a red-shift in the absorption or spectral response of a photodiode. By comparing the spectral response of photodiodes prepared by each method as shown in Fig. 4-3(a), one with $HgCl_2$ and one without $HgCl_2$ and only EdT/HCl, the 50% spectral cutoff varies by a small margin of only 70 cm^{-1}. Such a small shift can be attributed to the batch to batch variation in the synthesis of the HgTe CQDs as shown in Fig. 4-3(b), and the $HgCl_2$ solution at a concentration of 10 mM does not lead to sintering of ripening the quantum dots.

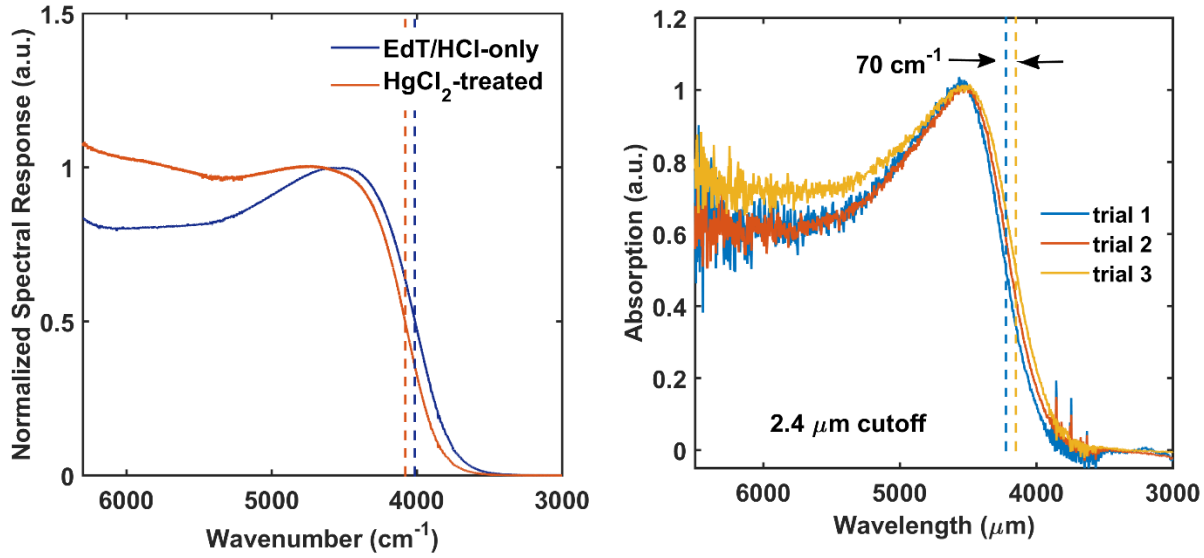

Figure 4-3 (a) *Spectral response of HgTe CQD-based photodiodes using $HgCl_2$ (orange) and using only EdT/HCl (blue) measured at room temperature.* ***(b)*** *Absorption spectra of HgTe CQDs synthesized at three different trials for detection near 2.4 μm and showing the variation of the synthesis.*

For the photodiodes, the current density-voltage (JV) behavior provides information on the quality of the photodiode by its ability to rectify the current. Shown in Fig. 4-4 is the JV behavior for EdT/HCl-only reference photodiode (Fig. 4-4(a)) and a $HgCl_2$-treated photodiode (Fig. 4-4(b)). The photocurrent density was, on average, unaffected by the $HgCl_2$ treatment. In general, the $HgCl_2$ treatment of the HgTe CQD films results in an increased rectification, more than 10-fold increase in the shunt resistance, and more than 2-fold increase in the open-circuit voltage of the photodiode. The increase in the shunt resistance is important here as it is proportional to the decrease in the recombination processes in HgTe CQD films and highlights the significance of addressing the non-radiative processes that limit the quantum yield.

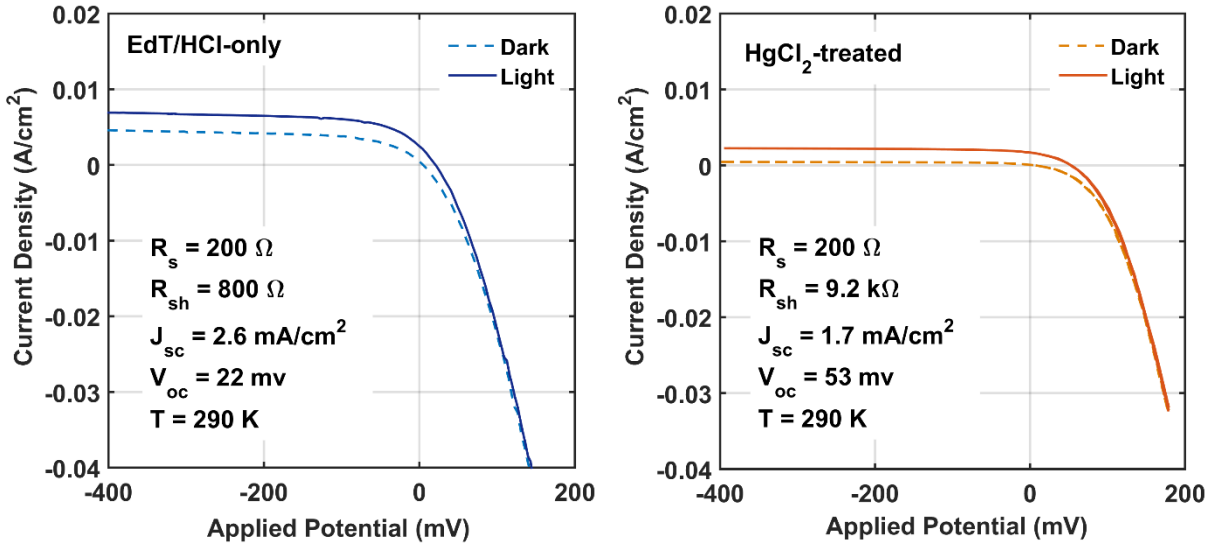

Figure 4-4 *Current density-voltage (JV) behavior for* ***(a)*** *EdT/HCl-only and* ***(b)*** *$HgCl_2$-treated photodiodes with spectral cutoff near 2.5 µm near room temperature.*

An understanding of the temperature dependent processes in the photodiode can be helpful for designing better photodetectors as well as determining the operating temperatures reasonable for photodetector operation. Infrared photodetectors are often operated at decreased temperatures using multi-stage thermoelectric coolers and Stirling coolers to reduce the thermally generated noise currents and improve the detector sensitivity and stability. In Fig. 4-5, the temperature dependence of the zero-bias shunt resistance and reverse-bias dark current density are provided as an Arrhenius plot to determine the activation energy of the limiting noise currents. From Fig. 4-5(a), it is apparent that the zero-bias shunt resistance, which determines the Johnson noise limit for the photodiode, does not follow a single activation energy and has various temperature-dependent mechanism of noise current generation. At high temperatures, the shunt resistance is well described by a geminate recombination process with a fixed radiative fraction and activation energy equivalent to the CQD band gap energy, as described by Eq. (4.1).

$$R_0 = \frac{1}{A}\frac{\hbar}{e^2}\frac{f_c}{\eta\tilde{\nu}}\, e^{\frac{hc\tilde{\nu}}{k_B T}} \tag{4.1}$$

In Eq. (4.1), A is the area of the photodiode in cm^2, $\hbar$ is the reduced Planck constant in Js, e is the charge in Coulomb, $\tilde{\nu}$ is band gap energy expressed in wavenumbers (cm^{-1}), k_B is the Boltzmann constant in J/K, T is temperature in Kelvin, f_c is the radiative fraction, and η is the quantum efficiency. Here, f_c was fixed at 10^{-3} for a HgTe CQD with band gap of 4000 cm^{-1} and photodiode with quantum efficiency (η) of 0.5 as given by the room temperature data as discussed later. As the temperature decreases, the R_0 deviates from a geminate recombination mechanism and converges for both the EdT/HCl and $HgCl_2$ treated photodiodes.

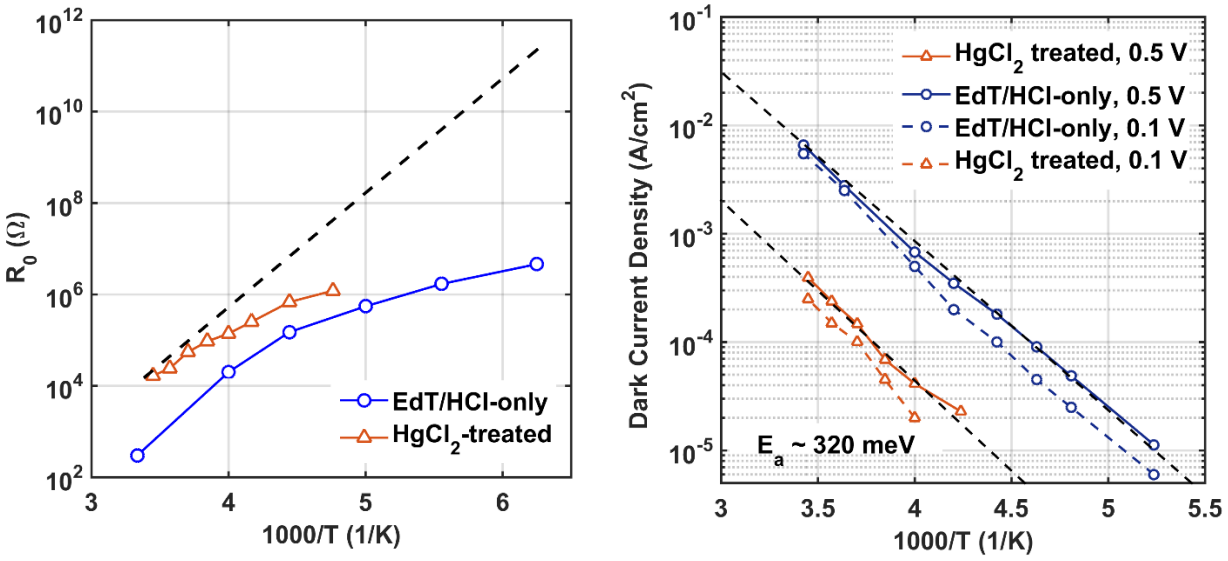

Figure 4-5 *Arrhenius plot of EdT/HCl-only and $HgCl_2$-treated photodiodes operating at* ***(a)*** *zero applied bias and* ***(b)*** *reverse bias of 100 mV (dashed) and 500 mV (solid). Black dashed lines in (b) correspond to an activation energy of 320 meV.*

While operating under reverse bias, a single activation energy is extracted from the Arrhenius plot of the temperature dependence of the dark current density. Additionally, the

activated process for dark current generation appears to be independent of the applied bias for values between 100 mV and 500 mV. An activation energy of ~320 meV fits well the trend in the temperature dependence of the dark current density, and is between half the gap and the total gap energy, which indicates contributions to the dark current density due to both geminate recombination and some non-radiative mechanism not well understood at this time. It worth noting that the dark current density at 500 mV reverse bias of 4×10^{-4} A/cm^2 is nearly equivalent to the extended InGaAs photodiodes of the same area and cutoff wavelength operating under a 500 mV reverse bias at room temperature available from Hamamatsu (Hamamatsu model G12183–030K).

The temperature dependence of the figures of merit, responsivity and specific detectivity, are shown in Fig. 4-6(a) and (b), respectively. As previously mentioned, the photocurrent density, and therefore the responsivity, was on average unaffected by the $HgCl_2$ treatment. In Fig. 4-6(a), the responsivity of the photodiodes was generally independent of the EdT/HCl or $HgCl_2$ solutions used. Therefore, the difference in the specific detectivity was the result of the difference in noise due to thermally generated carriers proportional to the shunt resistance, R_0. A similar trend in the specific detectivity, as shown in Fig. 4-6(b), is observed as was previously seen for the zero-bias shunt resistance previously shown in Fig. 4-5(a) above.

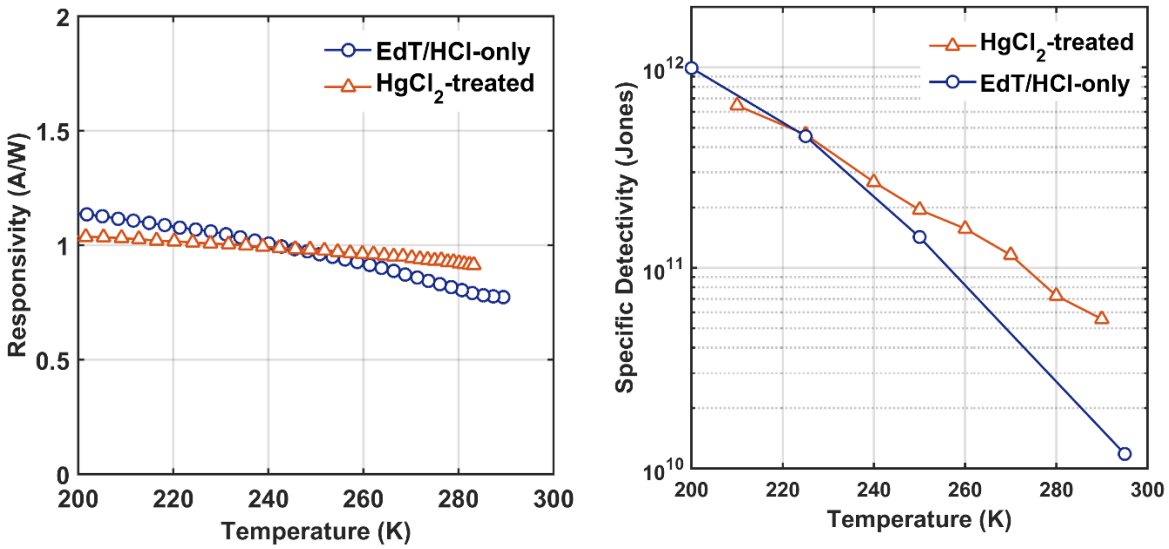

Figure 4-6 *Temperature dependence of the* ***(a)*** *responsivity and* ***(b)*** *specific detectivity for EdT/HCl-only and $HgCl_2$-treated photodiodes with a spectral cutoff near 2.5 µm.*

To demonstrate the range of operation in the extended shortwave infrared region, photodiodes with cutoff wavelengths between 2.2 and 2.6 µm were fabricated with different size HgTe CQDs. From Fig. 4-7(a), a small difference in the responsivity may follow from the $HgCl_2$ treatment, though the difference of average values was no more than 20%. For larger HgTe CQDs with cutoff wavelengths greater than 2.4 µm, the average quantum efficiency was near 50% and decreased for smaller HgTe CQD-based photodiodes with spectral cutoff below 2.4 µm. The source of the decreased quantum efficiency of wider gap HgTe CQDs is made apparent by the JV behavior for a 2.25 µm cutoff $HgCl_2$-treated photodiode measured at room temperature shown in Fig. 4-7(b).

A kink in the JV curve was observed and, as discussed in chapter 2 for Ti(TiOx) electron transport layers, this is possibly due to an interface dipole that forms at the ITO-HgTe CQD interface.[121] Another explanation is the increasing conduction band edge of the HgTe CQD such

that the energy offset between the HgTe CQD electron energy and ITO conduction level energy is too large, leading to poor collection efficiency and increased electron accumulation at the ITO cathode; however, decreasing the ITO work function has been shown to reverse this effect in organic photodiodes.[122] As an anecdote, a similar effect was observed when ITO was cleaned with peroxide and reused to make a 2.5 µm photodiode where the S-shaped kink emerged possibly due to the oxidation and increased work function of ITO with respect to the HgTe CQD conduction level energy. Therefore, reducing the ITO work function or using an alternative conductor such as aluminum-doped zinc oxide (AZO) or fluorine-doped tin oxide (FTO) that have lower work functions will lead to improved quantum efficiencies for HgTe CQD-based photodiodes with higher energy spectral cutoffs.

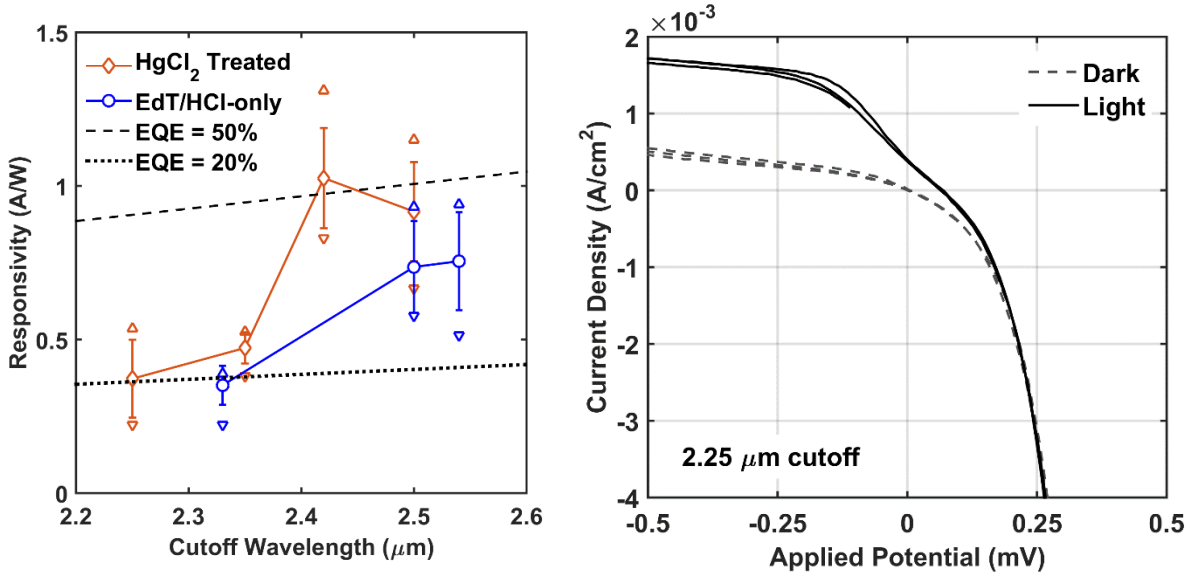

Figure 4-7 (a) *Dependence of the responsivity of the $HgCl_2$-treated and EdT/HCl-only HgTe photodiodes on the size of the HgTe colloidal quantum dots.* ***(b)*** *Current density-voltage (JV) behavior of a 2.25 µm cutoff photodiode at room temperature.*

The zero-bias resistance-area (R_0A) product is used as a proxy for the sensitivity of an infrared photodetector and often quoted in place of the specific detectivity along with the quantum efficiency. Fig. 4-8 shows the dependence of the R_0A product for photodiodes as a function of the cutoff wavelength proportional to the size of the HgTe CQDs. Like the observation that the R_0 increased by 10-fold for the 2.5 μm cutoff photodiodes, the affect of the $HgCl_2$ solution on increasing the R_0 is observed for HgTe CQD films with spectral cutoff in the range from 2.2-2.6 μm and likely extends to below 2.2 μm for HgTe CQD-based photodiodes. Also shown in Fig. 4-8 is the trend in R_0A for extended InGaAs (IGA Rule-17)[123] and HgCdTe (MCT Rule-07)[124] photodiodes. The HgTe CQD-based photodiodes treated with the $HgCl_2$ solution follow closely to the InGaAs heuristic, IGA Rule-17, and can potentially offer comparable sensitivity at operating temperatures near 300 K. Improving the quantum yield of the HgTe CQD another 10-fold will bring it on par with state-of-the-art HgCdTe and beyond the commercial performance of extended InGaAs.

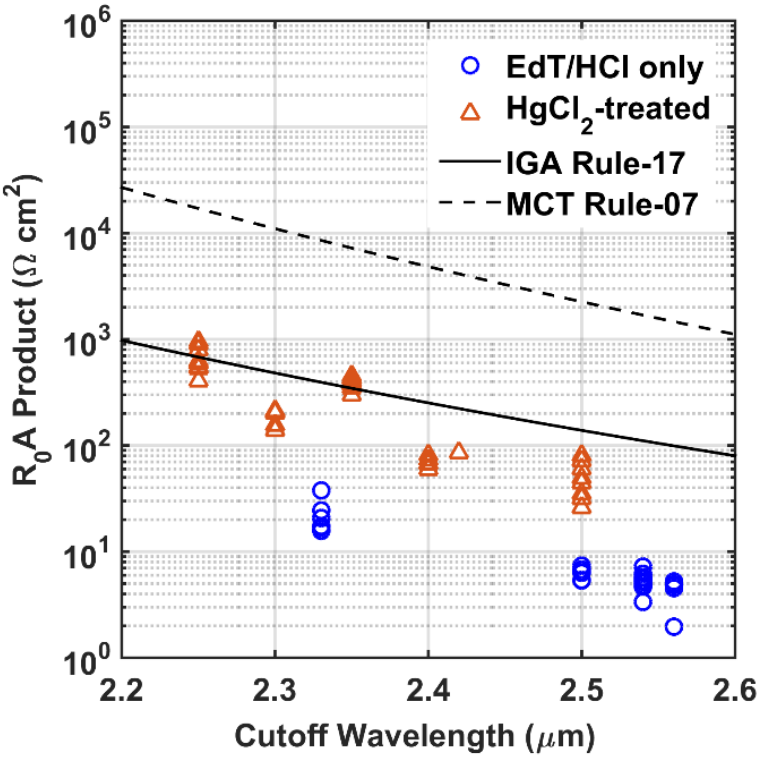

Figure 4-8 *The shunt resistance-area (R_0A) product against the cutoff wavelength for the EdT/HCl-only and $HgCl_2$-treated photodiodes.*

From the responsivity and R_0A, the specific detectivity of a zero-bias operated, Johnson noise limited photodiode can be calculated given by Eq. (4.2).

$$D^* = \mathcal{R}\sqrt{\frac{R_0A}{4k_BT}} \tag{4.2}$$

Fig. 4-9 shows the specific detectivity of the HgTe CQD-based photodiodes in comparison with commercial extended InGaAs and HgCdTe single element photodiodes of area 1 mm^2 and operated at room temperature. On average, the specific detectivity increased between 3-fold and as much as 6-fold when HgTe CQD films are treated with the $HgCl_2$ solution. In comparison with InGaAs, HgTe CQD are about 2-fold worse but improving the short-wavelength photodiode quantum

efficiency and reducing the non-radiative recombination of HgTe CQD films can lead to rapid advancement of HgTe CQD on par or beyond InGaAs. Also provided is the specific detectivity of a HgTe CQD-based photodiode of ITO/Bi_2Se_3/HgTe/Ag_2Te/Au inside a Fabry-Perot cavity where the cavity enhanced the responsivity 2-fold, increasing specific detectivity from 3×10^{10} Jones to 7.5×10^{10} Jones at 2.2 µm spectral cutoff.[125] The $HgCl_2$ treatment brings the shortwave infrared photodiode on par with the cavity-enhanced photodiode, and coupling the $HgCl_2$ treated photodiode to a cavity should lead to a similar 2-fold enhancement for specific detectivity equivalent to extended InGaAs at room temperature and 2.2 µm spectral cutoff.

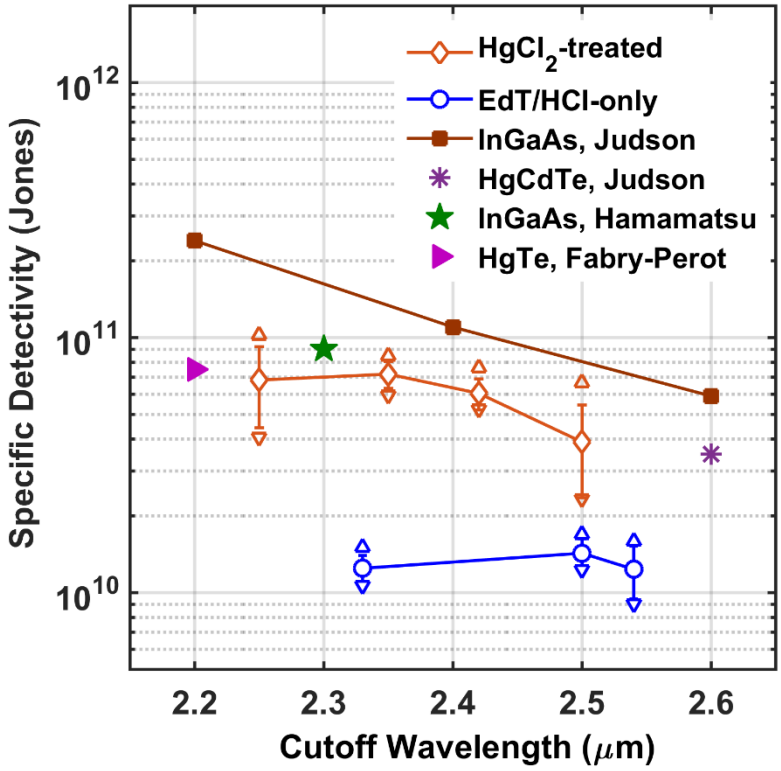

Figure 4-9 *Specific detectivity for photodetectors of area 1 mm^2 at 20-25°C as a function of the detector cutoff wavelength for extended InGaAs, HgCdTe, and HgTe CQD-based photodiodes treated with EdT/HCl only, $HgCl_2$ treated, and included in a Fabry-Perot cavity*[125].

4.4 Summary

HgTe colloidal quantum dots were fashioned into a photodiode and used for the detection of shortwave infrared light up to 2.5 μm. The quality of a semiconductor is determined by its photoluminescence quantum yield, and the use of a $HgCl_2$ methanolic solution was shown to improve the photoluminescence of HgTe CQD films by 10-fold compared to the EdT/HCl crosslinker solution generally used when fabricating HgTe CQD-based photodiodes. Therefore, photodiodes fabricated using the $HgCl_2$ solution during the layer-by-layer film deposition demonstrated improved specific detectivity due largely to a reduction of the photodetector noise and increase in the rectification of the photodiode at room temperature. The influence of the $HgCl_2$ solution was most apparent for photodiodes at shorter cutoff wavelengths down to 2 μm. From these results, a better understanding of the HgTe CQD surface will lead to further improvements in photodiode performance. Determining the origin of the non-radiative recombination and ligands that both reduce the non-radiative recombination rate and improve the charge carrier mobility will be beneficial to the development of competitive HgTe CQD-based extended shortwave infrared photodetectors.

Chapter 5 Dual-Band Infrared Photodetection

This chapter describes the development of a HgTe CQD dual-band infrared photodetector. Multi-spectral and hyperspectral photodetection is analogous to the transition from black-and-white imaging to color images, providing a greater amount of detail and information to the user. One of the challenges today in infrared multi-spectral imaging is the complex processing of multi-stack photodetectors from epitaxial materials. Here, colloidal quantum dots have a major advantage in additive manufacturing for multi-spectral photodetection, and work on the development of HgTe CQD photodiodes for shortwave and mid-wave infrared photodetection is presented.

5.1 Designing infrared multi-spectral photodetectors

Development on third-generation infrared detectors, multi-band infrared detection began in 2000 and efforts to improve multi-band technologies continue today.[3,6] Individually, shortwave infrared imaging provides visible-like imaging with textural and chemical information while mid-wave and long-wave infrared capture thermal information and enhance night-vision imaging capabilities. Combining the information and imaging capabilities of each spectral region extends and improves infrared imaging for applications such as missile tracking, surveillance, object recognition, non-invasive inspection, and remote sensing.[13,126] Multi-band detector technologies, most commonly dual-band for MWIR/LWIR detection, are based on HgCdTe,[127–130] III-V-based Type-II superlattices,[131–133] and quantum well infrared photodetectors.[134] Though these technologies are mature in development, their manufacturability is low due to long run times and complex production processes with low yields. Improving the production efficiency of high-quality epitaxial semiconductors remains an active area of development.[135,136] HgTe CQDs with

tunable infrared absorption present an opportunity to increase the manufacturability of dual-band detectors through solution-processed additive manufacturing.

Dual-band detectors can be designed consisting of either a two-terminal device or a three-terminal device. The three terminal device consists of a common ground and two electrical contacts for measuring currents or applying voltages to each detector pixel. Fig. 5-1(a) is an example of a three-terminal photoconductive device for SWIR/MWIR imaging. The device in Fig. 5-1(a) has pixels for each region of detection lying next to each other and light is incident normal to the surface. The voltages V_1 and V_2 at each terminal can be different from each other and optimized for sensing in each spectral region, or equivalent, in which case the number of terminals can be reduced to two to simplify the electrical requirements. For HgTe CQDs, such photoconductive detectors have been demonstrated for multi-band photodetection in the SWIR/MWIR[137] and SWIR/MWIR/LWIR.[138] These devices required additional processing steps to pattern each pixel with different sizes of CQDs for different spectral regions. Consequently, the additional processing steps reduce the scalability and manufacturability of this design.

A two-terminal device has, first, the advantage of one less electrical connection required to operate the detector. As shown in Fig. 5-1(b), the operation is analogous to a single-band detector, consisting of two electrodes for the detector and the materials are vertically stacked. However, the two-terminal device now contains two layers of different sized CQDs for SWIR and MWIR infrared photodetection in this example. The light is incident from the top-side and requires that the wider gap material, *i.e.* the SWIR absorber, be placed on top of the narrower gap absorber. In this way, the SWIR absorber acts as a window to the MWIR absorber and ensures that incident

radiation reaches the MWIR detector in the stack. Fig. 5-1(b) also shows a simple electrical diagram, indicating that the two-terminal device consists of two photodiodes stacked back-to-back. A single voltage supply operated at either a positive or negative voltage controls which photodiode is forward bias, or "off," and which photodiode is reverse bias, or "on," for bias-selectable infrared detection. The second advantage to this design is the reduced processing requirements as each pixel is identical and eliminates the need for patterning each pixel with different CQDs as in the three-terminal device.

For its advantages, the two-terminal device poses a design challenge. In Fig 5-1(b), the photodiode stack consists of both a p-on-n photodiode (*i.e.* p-type layer on top and n-type layer on bottom as in the MWIR photodiode) and a n-on-p photodiode. The p-type layer is common to both photodiodes and facilitates hole transport across the interface. Until now, the discussions of the HgTe CQD photodiodes in Chapters 2, 3, and 4 have focused on the normal type p-on-n photodiode. The challenge here is to design an inverted photodiode, *i.e.* a n-on-p photodiode, with HgTe CQDs to realize the two-terminal dual-band photodetector and take full advantage of the scalability and manufacturability afforded by CQDs.

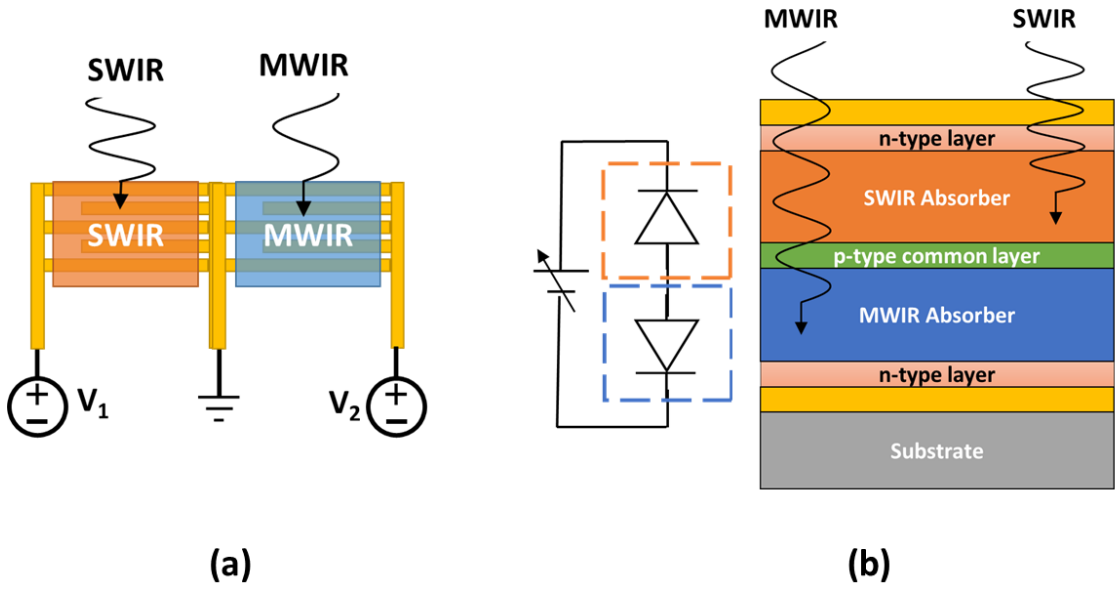

Figure 5-1 (a) *Three-terminal dual-band infrared photodetector composed of a shortwave infrared (SWIR) photoconductor pixel and a mid-wave infrared (MWIR) photoconductor pixel.* V_1 *and* V_2 *are external voltages applied to each photoconductor.* ***(b)*** *Simple circuit diagram (left) and multi-layer design (right) for the two-terminal dual-band infrared photodetector. The device consists of a SWIR photodiode in series with a MWIR photodiode. Light is incident through the SWIR photodiode.*

5.2 Development of the inverted HgTe CQD photodiode

This section describes the development of the inverted photodiode and its characteristics with respect to the normal photodiode. First, a design principle is put forth based on insights from chapter 2 and, by fortuity, a suitable material is identified as an n-type layer. Second, a sequence of device iterations are presented to outline the path to designing a well-behaved inverted photodiode. Finally, SWIR and MWIR inverted photodiodes are demonstrated and the performances are compared to the normal-type (p-on-n) photodiodes.

Single-band HgTe CQD photodiodes as described in Chapters 3 and 4 consisted of ITO/HgTe/Ag_2Te/Au to form the normal type, or p-on-n, photodiode. To understand the challenge with the inverted photodiode, begin by considering the SWIR/MWIR dual-band design, adapted from the single-band structure, that consists of ITO(n)/HgTe(SWIR)/Ag_2Te(p)/HgTe(MWIR)/Au(n). One immediate problem with such a structure is the HgTe/Au junction of the inverted photodiode, which is typically Ohmic and has previously been unreliable in the design of rectifying photodiodes with HgTe CQDs. The strategy then is to introduce an n-type semiconductor layer that would form a junction with HgTe CQDs to rectify the current and facilitate the collection of electrons at Au.

In Chapter 2, commonly used n-type metal oxides were evaluated and largely unsuccessful at forming rectifying heterojunctions with HgTe CQDs. Additionally, many of these commonly reported n-type semiconductors require post-processing at temperatures well above 100^{o}C. In the inverted photodiode, the n-type layer will be deposited atop the HgTe CQD film and the processing of the layer must be compatible with the HgTe CQDs, *i.e.* processed at room temperature to prevent sintering or damage to the absorber layer. Under these constraints, one option is a n-type colloidal nanoparticle solution. The nanoparticles can be processed and synthesized independent of the photodiode and then integrated with the HgTe CQD film at room temperature. An obvious choice is the n-type non-aggregated HgTe CQDs described in Chapter 2.3.

A second option is the class of bismuth chalcogenide semiconductors, *i.e.* Bi_2S_3, Bi_2Se_3, and Bi_2Te_3. Bismuth chalcogenides are well known to form n-type semiconductors with doping densities of 10^{17} cm^{-3} for Bi_2S_3,[139] $>10^{18}$ cm^{-3} for Bi_2Se_3,[140] and $>10^{19}$ cm^{-3} for Bi_2Te_3.[141] In PbS

CQD photovoltaics, Bi_2S_3 nanoparticles have been employed as an n-type semiconductor layer to realize both the normal and inverted devices while using standard ITO and metal contacts.[142] Bulk Bi_2Se_3 has been well-documented as an n-type semiconductor due to its inherently high concentration of selenium defects,[143] though only a limited number of colloidal synthetic processes have been developed for Bi_2Se_3 nanoparticles, which includes sonochemical[144] and micellular colloidal methods.[145] Colloidal n-type Bi_2Te_3 nanoparticles are more developed due to interest in its application for thermoelectrics.[146]

To evaluate the bismuth chalcogenides as n-type layers in the HgTe CQD heterojunction, the band gaps of each were considered. Following from the challenges of band engineering and energy matching wide band gap layers to the narrow band gap HgTe CQDs described in Chapter 2, a wide band gap bismuth chalcogenide is less desirable here. Bi_2S_3 was reported to have a wide band gap of ~1.3 eV and low electron affinity;[139,142] therefore, it is expected Bi_2S_3 would form a large barrier to electron transport, which would adversely affect the performance of the MWIR photodiodes. The reported bulk band gaps of 0.27 eV and 0.15 eV for Bi_2Se_3 and Bi_2Te_3,[147,148] respectively, are promising for good energy alignment with the HgTe CQDs owing to their narrow band gaps. Following from the common anion rule, the valence band matching of HgTe and Bi_2Te_3 and small valence band offset between HgTe and Bi_2Se_3 are expected to contribute to the favorable energy alignment of these semiconductor heterojunctions. However, these assumptions neglect the surface effects that are especially important in determining the energy levels and work function of colloidal nanomaterials. Physical investigation will be required to assess band alignment of the HgTe-Bi_2Se_3 or HgTe-Bi_2Te_3 heterojunctions.

From a practical perspective, the ability to synthesize a clean colloid for the formation of high-quality thin films precludes any physical measurement. Therefore, the synthesis of Bi_2Te_3 was evaluated. The synthesis here was adapted from a reported procedure,[146] where bismuth acetate (0.1 mmol) is dissolved in oleic acid (2.5 mL) and octadecene (2.5 mL) at 100°C to form the bismuth oleate reagent. Then, trioctylphosphine-telluride (TOPTe, 1 M, 0.15 mmol) was injected and the reaction proceeded for 2 minutes. Finally, the reaction was cooled to room temperature, cleaned by precipitation with toluene and acetone, the supernatant was separated by centrifugation, and the Bi_2Te_3 nanoparticles were dissolved in chlorobenzene with sonication. The Bi_2Te_3 nanoparticles that formed was relatively large, ~250 nm in width, hexagonal platelets with a tendency to aggregate as shown in Fig. 5-2.

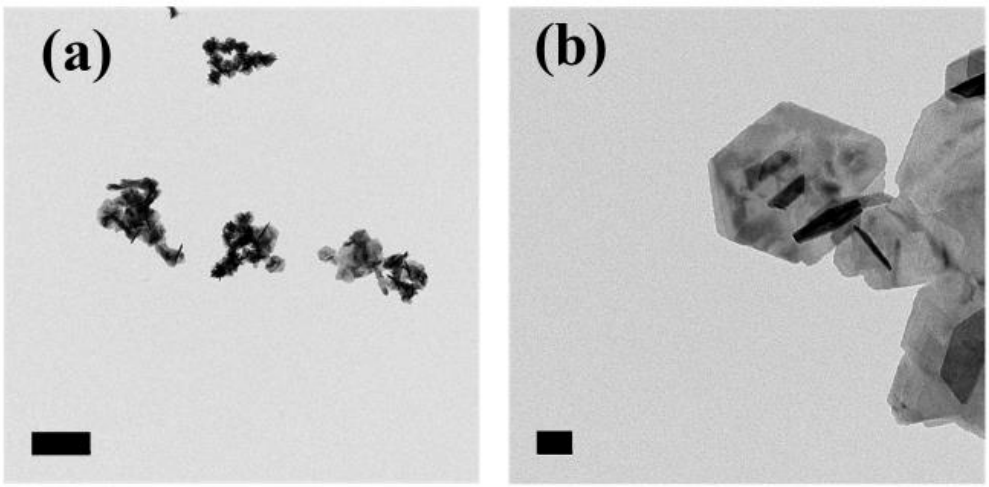

Figure 5-2 *Transmission electron microscope images of Bi_2Te_2 nanoparticles showing* ***(a)*** *aggregation and* ***(b)*** *hexagonal nanoplatelets. Scale bars* ***(a)*** *1 µm and* ***(b)*** *50 nm.*

Even with sonication, the Bi_2Te_3 nanoparticle solutions demonstrated limited colloidal stability. Similar syntheses were attempted, adding ligands such as trioctylphosphine and dodecanethiol, to improve the colloidal stability without much success. Until the Bi_2Te_3

nanoparticle solutions improve in quality, it cannot be used in HgTe CQD photodiodes. For this reason and those to be discussed in the remainder of this section, Bi_2Se_3 nanoparticles were ultimately selected as the electron transport layer to form an inverted photodiode with the p-type HgTe CQDs.

5.2.1 Method 1 for the synthesis of bismuth selenide nanoparticles

The first method described here for the synthesis of Bi_2Se_3 nanoparticles was adapted from the previous Bi_2Te_3 synthesis. In a nitrogen glovebox, bismuth acetate (0.1 mmol) was dissolved in oleic acid (5 mL) at 100^{o}C to form a bismuth oleate reagent. Separately, a solution of oleylamine-selenourea (0.2 M) was prepared by dissolving selenourea in oleylamine at 180^{o}C for 3-5 hours. Oleylamine-selenourea solution (0.75 mL) was injected into the bismuth oleate solution and immediately turned black. The reaction proceeded for 1-2 minutes before removing from heat and cooling to room temperature. The solution was cleaned by precipitation with excess amounts of acetone, separating the supernatant by centrifugation, and dissolving the Bi_2Se_3 nanoparticles in chlorobenzene with sonication. While the colloidal Bi_2Se_3 nanoparticles had a tendency to aggregate during the synthesis, careful sonication and cleaning could yield reasonably stable colloids such that quality thin films could be prepared.

The Bi_2Se_3 nanoparticles, shown in Fig. 5-3(a), varied in shape from triangular to hexagonal and in width, up to 10 nm. The low contrast in the transmission electron microscope image was partly due to the thin nature of the Bi_2Se_3 nanoparticles. Bi_2Se_3 is a layered semiconductor that inherently grows as hexagonal sheets[149] and can be exfoliated.[150] For very thin materials, fewer electrons scatter under the electron beam and thinner areas appear light, thus

reducing the image contrast. Therefore, it is reasonable to conclude that the Bi_2Se_3 nanoparticles here are in fact thin sheets, though the exact thickness was not measured. Fourier transform infrared (FTIR) spectroscopy of the Bi_2Se_3 nanoparticles is shown in Fig. 5-3(b) and a plasmonic peak is observed, indicating a heavily doped semiconductor nanoparticle. The Drude model[151] relates the free carrier density of a material to the plasmon frequency,

$$\omega_p^2 = \frac{n_e e^2}{\epsilon_0 m^*} \qquad (\#)$$

where ω_p is the plasmon frequency, n_e is the free carrier density, e is the elementary charge, ϵ_0 is the vacuum permittivity, and m^* is the electron effective mass. The effective mass for bismuth selenide is $0.124m_e$ where m_e is the free electron mass.[152] Therefore, with a plasmon frequency of 2.8×10^{13} Hz (or 950 cm^{-1}) as observed in Fig. 5-3(b), the estimated carrier density is ~ 1.2×10^{18} cm^{-3}.

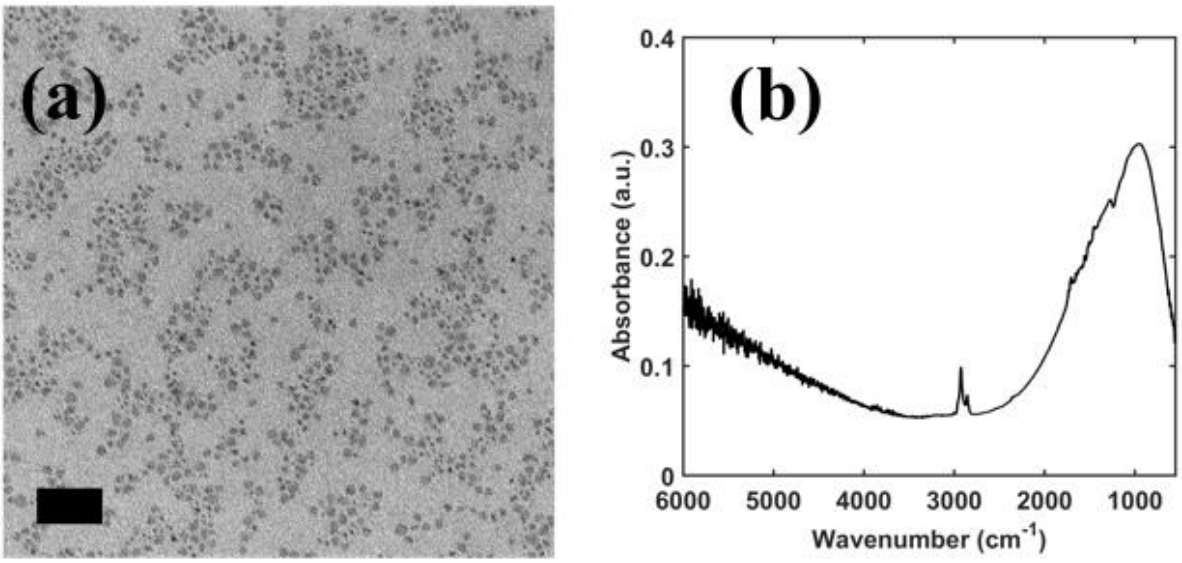

Figure 5-3 (a) *Transmission electron microscope image of Bi_2Se_3 nanoparticles. Scale bar is 50 nm.* ***(b)*** *Fourier transform infrared spectrum of Bi_2Se_3 nanoparticles with a low-energy infrared plasmon resonance.*

With a n-type doped Bi_2Se_3 nanoparticle solution prepared, the first design of the photodiode consisted of ITO/HgTe(MWIR)/Bi_2Se_3/Au. Bi_2Se_3 nanoparticles were spin-coated onto the HgTe CQD film and each layer was crosslinked with EdT/HCl/IPA. Despite the n-type doping of the Bi_2Se_3 nanoparticles, the photodiode still showed p-type polarity with respect to Au, *i.e.* holes were still collected at the Au electrode. This was thought to be the consequence of a Schottky junction between the Au and the Bi_2Se_3 nanoparticles, which could form a barrier to electrons. A lower work function silver (Ag) paint electrode replaced the Au in a structure ITO/HgTe(MWIR)/Bi_2Se_3/Ag paint and the polarity readily became n-type with respect to Ag paint as the contact became Ohmic. Indeed, the work function of the Bi_2Se_3 nanoparticles was measured to be within ~50 mV of the HgTe CQD work function (treated with EdT/HCl/IPA) and, for a n-type semiconductor, would be expected to form a Schottky junction to high work function

Au and an Ohmic junction to low work function Ag (refer to Chapter 2, Table 2-1). Despite the improved control of the polarity, the electrical performance was non-rectifying for both photodiode designs upon cooling to 80 K.

The next iteration of the inverted photodiode included the Ag_2Te p-type layer at the HgTe CQD and ITO interface. As with the normal p-type photodiodes, Ag_2Te could improve the selective transport of holes from HgTe CQDs and contribute to the diode rectification. Indeed, a device consisting of ITO/Ag_2Te(EdT)/HgTe(MWIR)/Bi_2Se_3/Ag paint showed inverted polarity with a responsivity of 50 mA/W and a specific detectivity near 4×10^9 Jones at 80 K. Still, the rectification was weak and the shunt resistance on the order of ~1 kΩ.

Alongside the Bi_2Se_3, the non-aggregating n-doped HgTe CQDs (described in Chapter 2.3) were also considered to form a homojunction in the inverted photodiode design with p-type HgTe CQDs. Here, a device consisting of ITO/Ag_2Te(EdT)/HgTe(MWIR)/HgTe(n)/Au was fabricated and demonstrated n-type inverted polarity with respect to Au at room temperature and at 80 K. Like the inverted photodiodes containing Bi_2Se_3 nanoparticles, the rectification was weak and the responsivity and specific detectivity were 0.1 A/W and 2×10^9 Jones, respectively. The surprising advantage in this design compared to the photodiode containing Bi_2Se_3 nanoparticles was the use of the evaporated Au electrode. It seems the HgTe(n)/Au junction does not present a significant barrier and could be used to form an electron selective contact for the inverted photodiode.

In the previous iterations of the inverted device, a solid-state cation exchange process was not performed on the Ag_2Te nanoparticle film. Therefore, introducing the cation exchange process to these inverted devices might also improve the performance analogous to the photodiodes

discussed in Chapter 3. To test the effect of the solid-state cation exchange process in the inverted photodiode, the film consisting of ITO/Ag_2Te/HgTe was soaked in a 10 mM $HgCl_2$ methanol solution for 5 seconds and rinsed with IPA. Then, the remaining HgTe(n) layer and Au electrode were added to the structure consisting of ITO/Ag_2Te/HgTe($HgCl_2$)/HgTe(n)/Au. Here, the notation HgTe($HgCl_2$) refers to the addition of the $HgCl_2$ soak after the deposition of the HgTe CQD film. Unexpectedly, the photodiode was p-type at room temperature before becoming n-type at low temperature with a 3-fold increase in the photocurrent density, a 3-fold increase in open-circuit voltage, and a specific detectivity of 3×10^{10} Jones, which is 8-fold greater than the previous inverted photodiodes. Based on these results, the $HgCl_2$ treatment is favorable for improving the photodiode operation and performance.

The inverted photodiode designs consisting of Bi_2Se_3 nanoparticles were n-type at all temperatures so long as the contact junction was Ohmic, as demonstrated with Ag paint. Then, in an effort to guarantee inverted n-type polarity at all temperatures, a thin film of Bi_2Se_3 nanoparticles was placed between the HgTe($HgCl_2$) soaked film and the HgTe(n)/Au electrode junction for a device consisting of ITO/Ag_2Te/HgTe($HgCl_2$)/Bi_2Se_3/HgTe(n)/Au. The result was room temperature n-type polarity with responsivity of 8 mA/W and specific detectivity of 4×10^{7} Jones. At 80 K, the performance was like the ITO/Ag_2Te/HgTe($HgCl_2$)/HgTe(n)/Au photodiode, having a responsivity of 0.4 A/W and specific detectivity of 4×10^{10} Jones. Fig. 5-4 provides a comparison of the photodiode JV behavior at 80 K without (Fig. 5-4(a)) and with (Fig. 5-4(b)) the Bi_2Se_3 nanoparticle layer. It becomes clear from these results that the $HgCl_2$ soak contributes to improved rectification, responsivity, and detectivity of the photodiode while the Bi_2Se_3 nanoparticles contribute to current rectification at operating temperatures up to 300 K.

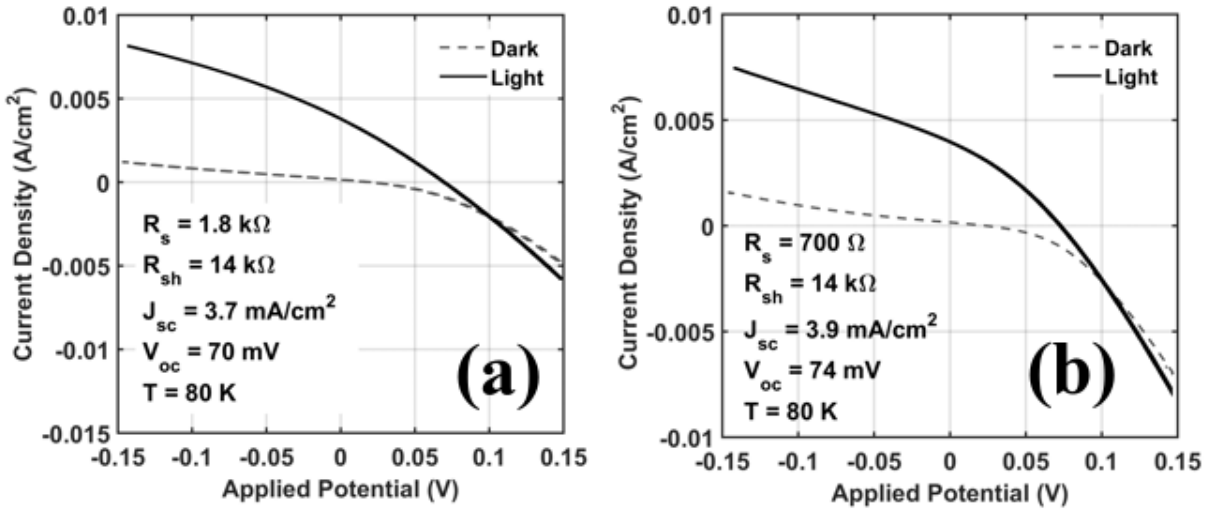

Figure 5-4 *Current density-voltage (JV) behavior for* ***(a)*** *ITO/Ag_2Te/HgTe($HgCl_2$)/HgTe(n)/Au and* ***(b)*** *ITO/Ag2Te/HgTe($HgCl_2$)/Bi_2Se_3/HgTe(n)/Au photodiodes.*

In another attempt to control the room temperature device polarity, the use of heavily doped HgTe, or HgTe(n+), CQDs in a photodiode consisting of ITO/Ag_2Te/HgTe($HgCl_2$)/HgTe(n+)/Au was shown to yield inverted polarity at all temperatures up to 300 K. The doping of the n-type non-aggregated HgTe CQDs was increased by growing larger HgTe CQDs with a size of 15 ± 2 nm as shown in Fig. 5-5(a). The significant doping is apparent from Fig. 5-5(b) given the appearance of an intraband absorption at 1000 cm^{-1} with equal intensity to the interband absorption with a cutoff at ~2100 cm^{-1}. For both HgTe(n+) CQDs and Bi_2Se_3 nanoparticles, the increased doping resulted in reliably inverted photodiode polarity.

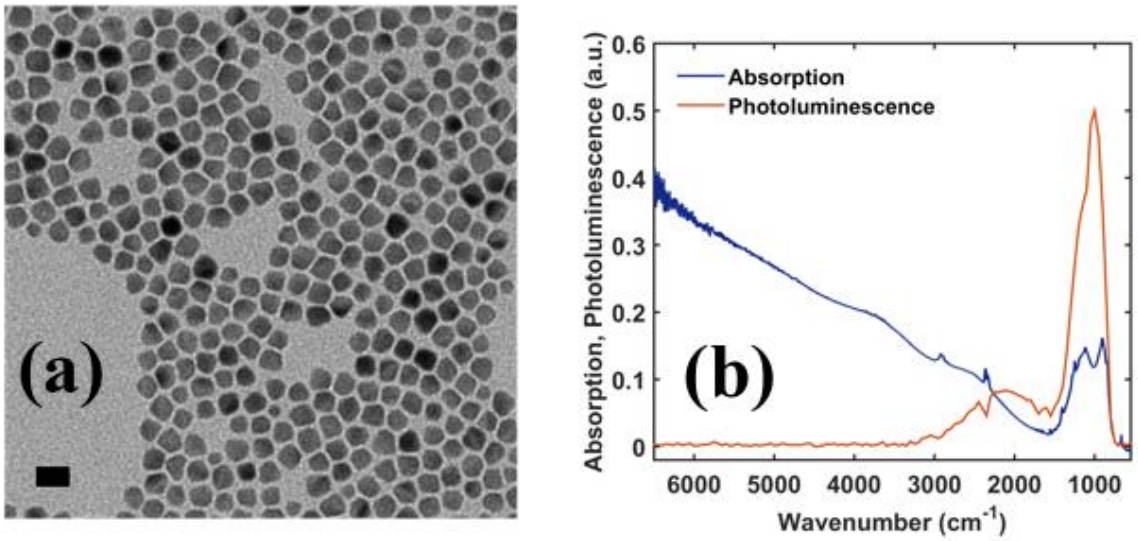

Figure 5-5 (a) *Transmission electron image of the non-aggregating HgTe CQDs captured by electron transmission microscopy. Scale bar is 20 nm.* ***(b)*** *Absorption and photoluminescence of the HgTe CQD from (a) with interband transition at 2100 cm^{-1} and intraband transition at 1000 cm^{-1}.*

5.2.2 Method 2 for the synthesis of bismuth selenide

A method of making colloidally stable Bi_2Se_3 nanoparticles was discovered wherein bismuth neodecanoate (0.2 mmol) was dissolved in oleylamine (5 mL) using dodecanethiol (0.2 mmol) at 70°C. A yellow solution formed, indicating the formation of the bismuth thiolate complex.[153] After equilibration for 5 minutes, oleylamine-selenourea (0.3 mmol; 0.2 M, 1.5 mL) solution was injected and the reaction rapidly turned black. The reaction proceeded for 1 hour without any loss of colloidal stability. The reaction was removed from heat, cooled to room temperature, and cleaned under ambient conditions with acetone followed by centrifugation. The yellow supernatant that contained unreacted bismuth thiolate complex was discarded and the precipitate was dried lightly with N_2 gas. Finally, the Bi_2Se_3 nanoparticles were readily dispersed in tetrachloroethylene, forming a stable dark brown or black colloid. The Bi_2Se_3 nanoparticles had

an average size of 12 ± 1 nm with irregular faceting as shown in Fig. 5-6(a). For the same procedure, increasing the reaction to 150°C resulted in many thin, hexagonal nanoplatelets, as shown in Fig. 5-6(b), with widths as large as 50 nm. Below 60°C, the reaction had very low yields and the nanoparticles were unstable after cleaning one time.

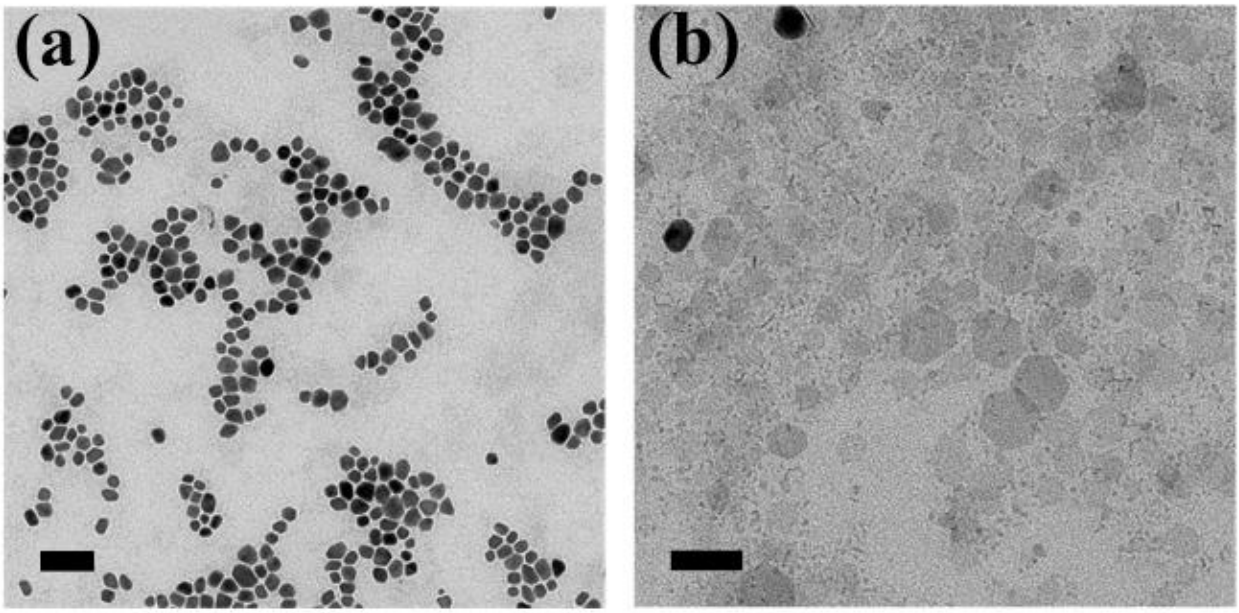

Figure 5-6 (a) *Transmission electron microscope images of Bi_2Se_3 synthesized by method 2. Scale bar is 100 nm.* ***(b)*** *Bi_2Se_3 nanoparticles synthesized by method 2 at a reaction temperature of 150°C. Scale bar is 50 nm.*

A preliminary investigation of the effect stoichiometry has on the method 2 synthesis was also conducted. The goal here is to evaluate the control of the n-type doping by increasing the fraction of metal in the synthesis where metal-rich nanoparticles are increasingly n-type in character. For the bismuth-rich synthesis at 70°C, the stoichiometry was increased from 2:3 (normal stoichiometry) up to 10:3 Bi:Se. The resulting bismuth selenide nanoparticles in Fig. 5-

7(a) showed irregular faceting, commonly featuring 3, 4, or 6 edges, and had an average width of 15 ± 3 nm with a Gaussian size distribution, shown in Fig. 5-7(b).

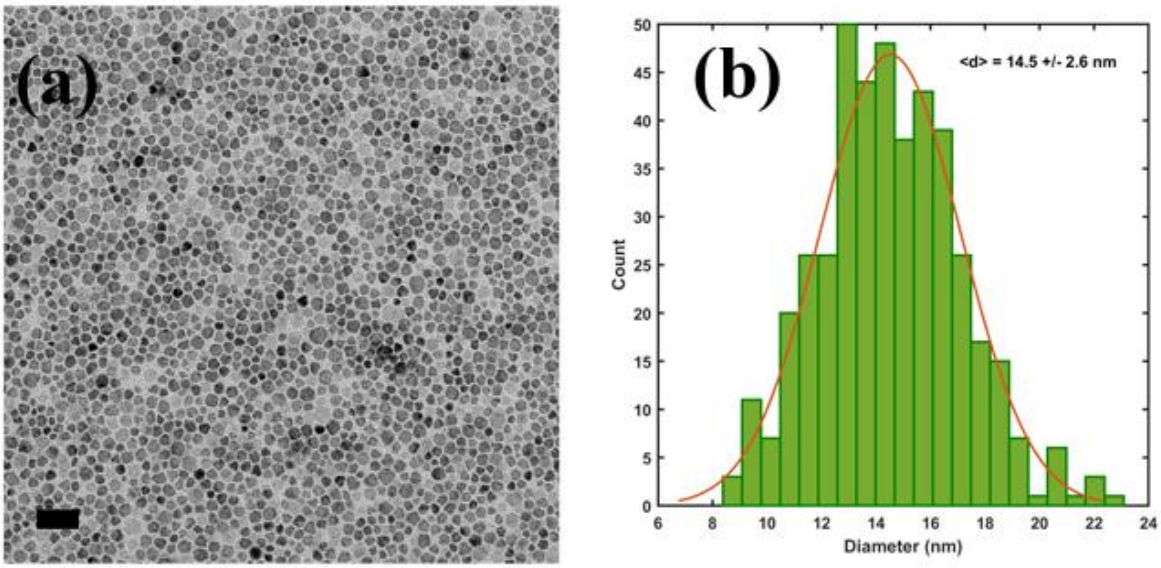

Figure 5-7 (a) *Transmission electron microscope image and* ***(b)*** *size distribution of Bi_2Se_3 nanoparticles synthesized by method 2 using a 10:3 Bi:Se ratio. In (a) the scale bar is 50 nm. The average size in (b) is 14.5 ± 2.6 nm.*

In the discussion of Bi_2Se_3 nanoparticles synthesized by method 1, the FTIR spectrum showed an absorption feature indicating a plasmon resonance due to the high free carrier density of the materials. Fig. 5-8 compares here the FTIR spectrum of bismuth selenide nanoparticles synthesized with 2:3 Bi:Se at 70°C (blue), 2:3 Bi:Se at 150°C (orange), and 10:3 Bi:Se at 70°C (yellow). From the FTIR spectra, increasing either the reaction temperature or the Bi:Se ratio leads to increased doping in the bismuth selenide nanoparticles. Here, high temperature synthesis has a plasmon frequency of ~ 2.8×10^{13} (945 cm^{-1}) and corresponding free carrier density of ~ 1.2×10^{18} cm^{-3}. The Bi-rich bismuth selenide nanoparticles have a higher doping density with a plasmon frequency at ~ 3.75×10^{13} Hz (1250 cm^{-1}) for a corresponding carrier density of ~ 2.2×10^{18} cm^{-3}.

Synthesis at 70°C using 2:3 Bi:Se significantly reduced the doping density of the Bi_2Se_3 nanoparticles in contrast to the results of synthesis method 1.

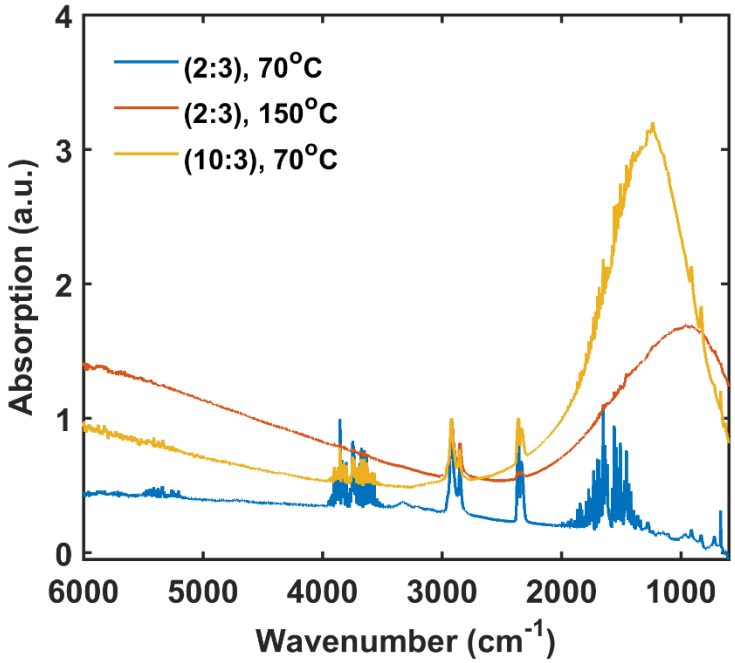

Figure 5-8 *Absorption of thin films of Bi_2Se_3 nanoparticles prepared as described by synthetic method 2 for reaction conditions of 2:3 Bi:Se at 70°C (blue), 2:3 Bi:Se at 150°C (red), 10:3 Bi:Se at 70°C (yellow).*

Inverted photodiodes fabricated with Bi_2Se_3 nanoparticles prepared by synthesis method 2 were, serendipitously, better in performance than those using Bi_2Se_3 synthesized by method 1. The inverted photodiodes here consist of ITO/Ag_2Te/HgTe($HgCl_2$)/Bi_2Se_3/HgTe(n+)/Au with JV behavior at low temperature as shown in Fig. 5-9(b-d). At room temperature, the specific detectivity ranges from 1×10^8 Jones to 3×10^8 Jones with responsivity between 10 and 30 mA/W (or EQE of 0.3-1%) at a cutoff wavelength of 4 µm (Fig. 5-9(a)). At 80 K, the performance was equal to the best normal photodiodes (refer to Chapter 3) with specific detectivity between 8×10^{10} Jones and 1×10^{11} Jones and responsivity of 0.4-0.7 A/W (or EQE 10-17%) with a spectral cutoff

at 5 µm. The electrical behaviors shown in Fig. 5-9(b) and (c) are for photodiodes using less doped (*i.e.* 2:3 Bi:Se, 70°C, method 2) Bi_2Se_3 while Fig. 5-9(d) shows the behavior for a photodiode with heavily doped (10:3 Bi:Se, 70°C, method 2) Bi_2Se_3 nanoparticles.

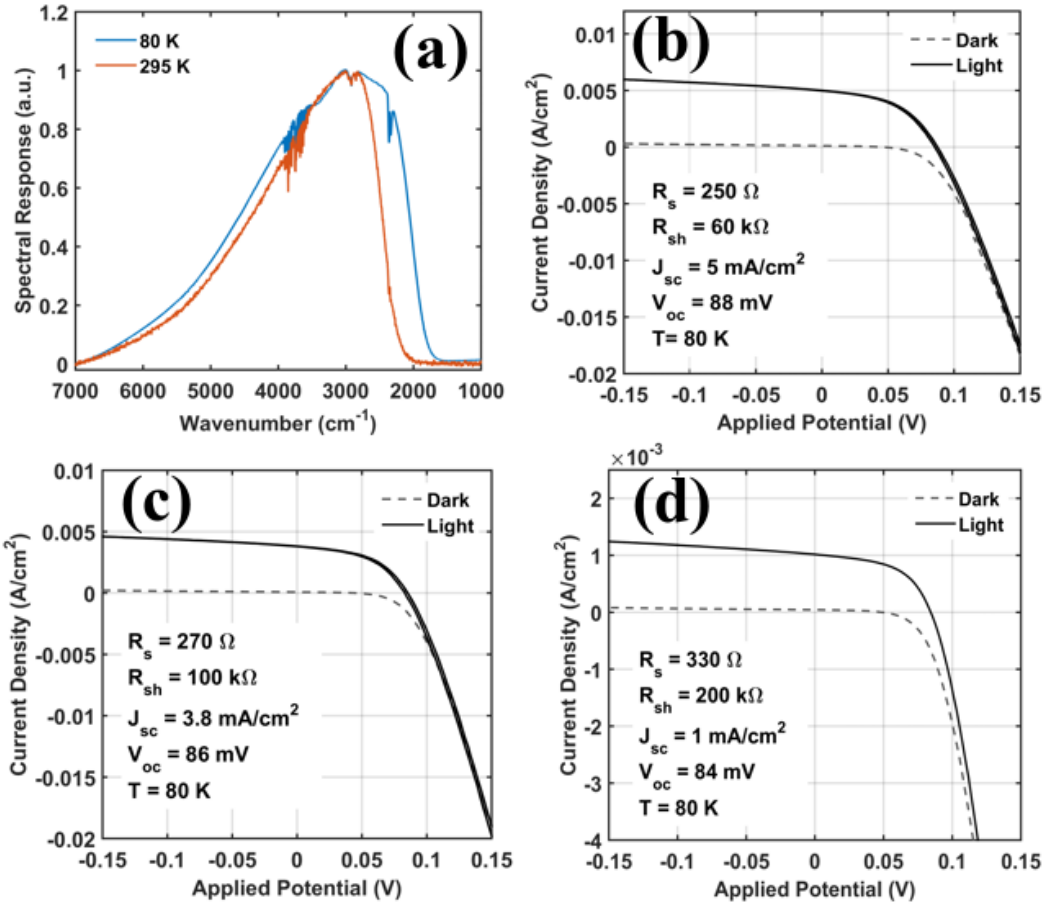

Figure 5-9 (a) *Spectral response of ITO/Ag_2Te/HgTe($HgCl_2$)/Bi_2Se_3/HgTe(n+)/Au photodiode measured at room temperature (orange) and 80 K (blue).* ***(b,c)*** *Current density-voltage (JV) behavior for photodiodes using Bi_2Se_3 nanoparticles prepared by method 2 at 70°C with a 2:3 Bi:Se ratio.* ***(d)*** *JV behavior for photodiode using heavily doped Bi_2Se_3 nanoparticles prepared by method 2 at 70°C with a 10:3 Bi:Se ratio. Light source for JV measurement was a 600°C calibrated blackbody source.*

The most significant differences between these photodiodes and those prepared with Bi_2Se_3 nanoparticles prepared by method 1 (see Fig. 5-4) are the magnitude of the shunt resistance and

the increasing reverse bias leakage current density. These attributes depend on the non-radiative recombination rates due to defects and non-radiative energy losses in the absorber or at interfaces of the device.[102] To understand the origin of these differences, one can begin by considering the energy alignment between the levels of the HgTe CQD and the Bi_2Se_3 nanoparticles. Poor band alignment between the conduction and valence band energy levels has been identified as one source of increased recombination detrimental to photovoltaic devices.[154–156] A preliminary measure of the relative differences in work functions between the HgTe CQDs and the Bi_2Se_3 nanoparticles supports the idea that band discontinuities may contribute to increased recombination.

By synthetic method 1, Bi_2Se_3 nanoparticles had a potential ~0.11 eV higher than HgTe CQDs. The high doping level of the Bi_2Se_3 implies that the conduction band energy and work function are nearly equivalent; therefore, a conduction band discontinuity of at least 0.25 eV (for a HgTe CQD with band gap 0.3 eV) may be present in the respective photodiodes. For Bi_2Se_3 prepared by synthetic method 2, the potential difference for heavily doped Bi_2Se_3 nanoparticles was 0.37 eV below HgTe CQDs, which could result in a conduction band offset of at most 0.12 eV when the HgTe CQDs are intrinsic and ($E_c - E_F$) is ~0.15 eV. The less doped (*i.e.* no plasmon resonance) Bi_2Se_3 nanoparticles work function was less than 0.09 eV above HgTe CQDs. Then, the expected offset will be less than 0.2 eV and decreases as the Bi_2Se_3 doping decreases. The expected differences in performance following from the predicted conduction band offsets provide only partial insight into the physics of the inverted photodiodes. This first look at the differences in behavior due to the Bi_2Se_3 nanoparticles is limited in that the formation of interface dipoles at heterojunctions can make such predictions unreliable.[157]

The device design using Bi_2Se_3 nanoparticles (method 2), heavily doped HgTe(n+) CQDs, and a $HgCl_2$ soak was generally applicable to HgTe CQDs of different sizes as demonstrated with an extended shortwave infrared photodiode. Fig. 5-10(a) provides a comparison of the JV behavior for the normal and inverted photodiodes operating at 80 K with a 5 μm cutoff. The behavior of the normal and inverted MWIR photodiodes is nearly identical. Fig. 5-10(b) provides a comparison of the extended short-wave infrared normal and inverted photodiodes operating at 300 K with a 2.5 μm cutoff. Here, the electrical behaviors of the normal and inverted photodiodes differ in their series resistance, shunt resistance, photocurrent density, and current rectification. Still, the specific detectivity of each photodiode was ~2×10^{10} Jones and the responsivities differed by only 20% with an average value of 300±30 mA/W. Overall, the performance of the inverted HgTe CQD photodiodes is equivalent to the performance of the normal type HgTe CQD photodiodes for both shortwave infrared and mid-wave infrared photodetection.

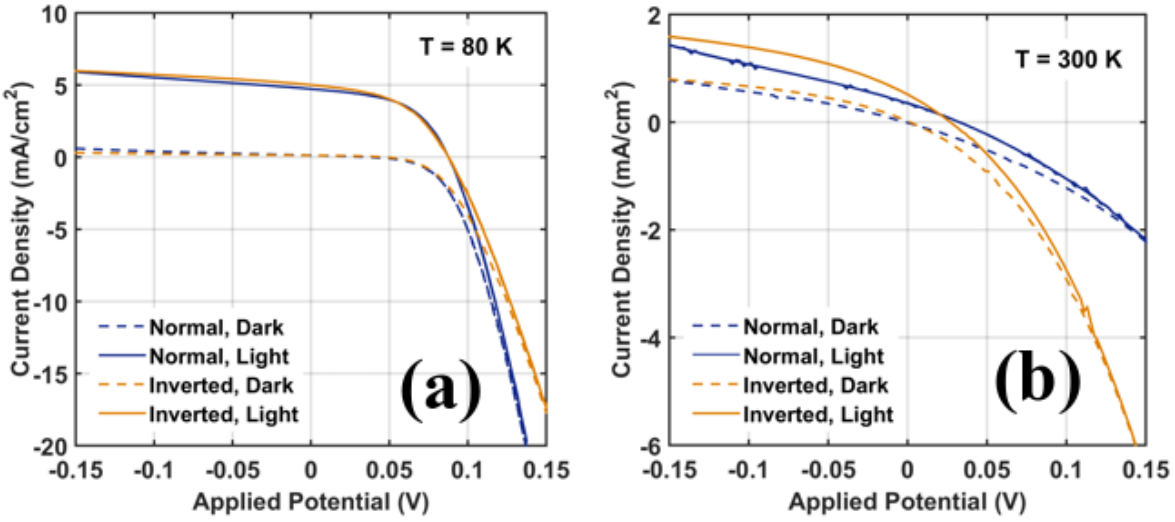

Figure 5-10 *Comparison of the current density-voltage (JV) behavior for* ***(a)*** *normal and inverted mid-wave infrared (MWIR) photodiodes operating at 80 K and* ***(b)*** *normal and inverted shortwave infrared (SWIR) photodiodes at 300 K. The light source in the measurement was a 600^{o}C calibrated blackbody source.*

5.3 SWIR/MWIR dual-band HgTe CQD photodetector

Following from the development of the inverted photodiode, dual-band detection with HgTe CQDs could be realized. This section discusses the design, operation, and characteristics of the HgTe CQD dual-band infrared photodetector. Finally, a demonstration of the imaging capabilities enabled by dual-band infrared sensing in the short-wave and mid-wave infrared is presented. The discussion to follow is adapted from X. Tang, M. M. Ackerman, P. Guyot-Sionnest, "Dual-band infrared imaging using stacked colloidal quantum dot photodiodes," Nature Photonics, **13**, 277–282(2019), Springer Nature Limited.

Dual-band infrared photodetectors for operation in the short-wave and mid-wave infrared were fabricated with simple solution processes. Beginning with the HgTe CQDs, two batches were synthesized with one absorbing in the MWIR and the other in the SWIR. The spectra of the HgTe

CQDs used to make the dual-band photodiode are shown in Fig. 5-11(a). In designing the dual-band detector, it is necessary to keep in mind the direction of incident radiation. Here, the light is incident from the top-side of the substrate, directly onto the photodetector (referred to as top-side illumination). Therefore, the top layer should be transparent to the range of light to be detected by the bottom photodiode. Thus, the SWIR HgTe CQD photodiode would be the top layer and act as a window, allowing MWIR light to reach the bottom MWIR HgTe CQD photodiode.

Fabricating the dual-band detector begins with spincoating Bi_2Se_3 nanoparticles were onto the ITO/sapphire substrate. Two layers were spincoated and each layer was crosslinked with a solution of 1,2-ethanedithiol (EdT) and hydrochloric acid (HCl) in isopropanol (IPA) at a 1:1:20 volume ratio. Then, MWIR HgTe CQDs were dropcast layer-by-layer at 40^{o}C and crosslinked with EdT/HCl/IPA solution and rinsed with IPA to form a film with thickness of ~400 nm. Ag_2Te nanoparticles were spincoated and the solid-state cation exchange was performed with 10 mM $HgCl_2$ in methanol, rinsing with IPA, and crosslinking with an EdT/IPA solution (2% by volume). Another Ag_2Te nanoparticle film was dropcast and only crosslinked with EdT/IPA as in the inverted photodiode fabrication described in the previous section. Layer-by-layer dropcasting of the SWIR HgTe CQDs was then repeated for a film thickness of ~400 nm, crosslinking each layer by EDT/HCl/IPA. Finally, two layers of the Bi_2Se_3 solution was spin-coated on the SWIR HgTe CQDs and each layer was crosslinked with EdT/IPA. Finally, 5 nm Au was deposited by electron-beam evaporation as the top contact. A representation of the total device structure is shown in Fig. 5-11(b). Note that here the heavily doped HgTe CQDs previously used in the inverted photodiodes has been omitted. It was discovered that Au could be directly evaporated onto Bi_2Se_3 and maintain an inverted photodiode so long as the Bi_2Se_3 nanoparticle solution was well cleaned. Fig. 5-11(c)

shows a cross-sectional scanning electron microscope image of the dual-band photodetector. In this configuration, infrared light was incident through the Au electrode such that the SWIR layer acts as a window to the MWIR incident radiation.

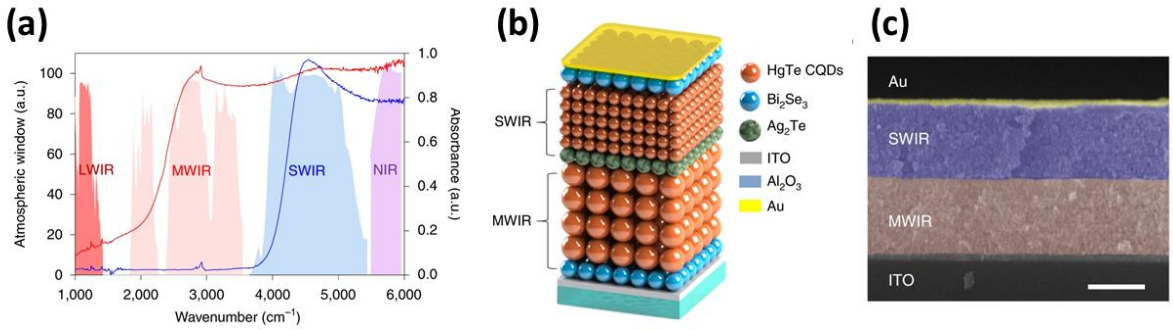

Figure 5-11 (a) *Absorption spectra of shortwave infrared (SWIR) and mid-wave infrared (MWIR) HgTe CQDs superimposed on a spectrum of the atmospheric absorption. The atmospheric windows are indicated.* ***(b)*** *Cartoon and* ***(c)*** *cross-section of the dual-band photodetector.*

An energy diagram of the photodetector at equilibrium is provided in Fig. 5-12(a). The representative band diagram shows that in the npn-type photodetector, the valence band offset will be sufficiently small and enable the transport of holes across the junction for operation of the photodetector. Efficient transport across the diode interface is achieved by minimizing the energy offset. For HgTe CQDs, the heavy holes contribute less to the confinement energy than the light electrons;[118,158] therefore, the change in the valence energy should be much less than the conduction energy as the CQD size changes. Indeed, such an observation has been made by studying thin films of HgTe CQDs using electrochemistry,[25] and the valence band offset here is predicted to be less than 60 meV. Due to the high doping density of the HgTe CQD film at the interface following from the cation exchange, this remaining barrier is expected to be thin such that holes can easily tunnel across the interface. In contrast, the energy offset in the conduction

band that is approximately equivalent to the difference in the band gaps of the CQD films and would be undesirable for the operation of a similar pnp-type photodetector. As shown in Fig. 5-12(b) and (c), the detector operating under a positive bias with respect to the n-doped side of the SWIR diode "turns-off" the SWIR diode and reverse biases the MWIR diode, while a negative bias with respect to the n-dopde side of the SWIR diode "turns-off" the MWIR and reverse biases the SWIR photodiode, respectively. Thus, switching the polarity of the potential on the photodetector will change the region of spectral detection.

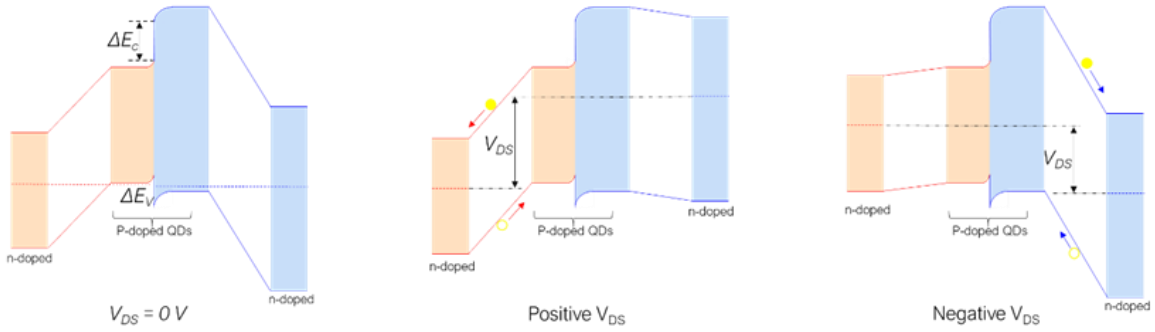

Figure 5-12 *Relative energy level diagram of the dual-band photodetector in* ***(a)*** *zero bias,* ***(b)*** *MWIR reverse bias, and* ***(c)*** *SWIR reverse bias operating modes.*

The effect of the external potential on the sensing of the dual-band photodetector is presented in Fig. 5-13(a) where the region of infrared detection switches between SWIR and MWIR with the polarity of the potential. The specific detectivity for the photodetector operating in either the SWIR or MWIR mode is presented in Fig. 5-13(b) as a function of operating temperature. For dual-band detection, the operating temperature of the photodetector is limited by the cooling required for sensitive MWIR detection. Notice that at low temperatures the MWIR performance is on par with the best reported photodiodes, however the D^* quickly falls when operating at higher temperatures. Approaching room temperature, the MWIR photodiode is likely

Ohmic and the D^* is rather poor with a value of ~1×10^7 Jones. Therefore, depending on the operating temperature, the photodetector is either a single band SWIR detector (at high operating temperatures) or a dual-band infrared detector (operating at low temperatures). As with the single element detector, improving the quantum yield, charge mobility, and absorption in the thin film detector will lead to improved sensitivity and higher temperature operation.

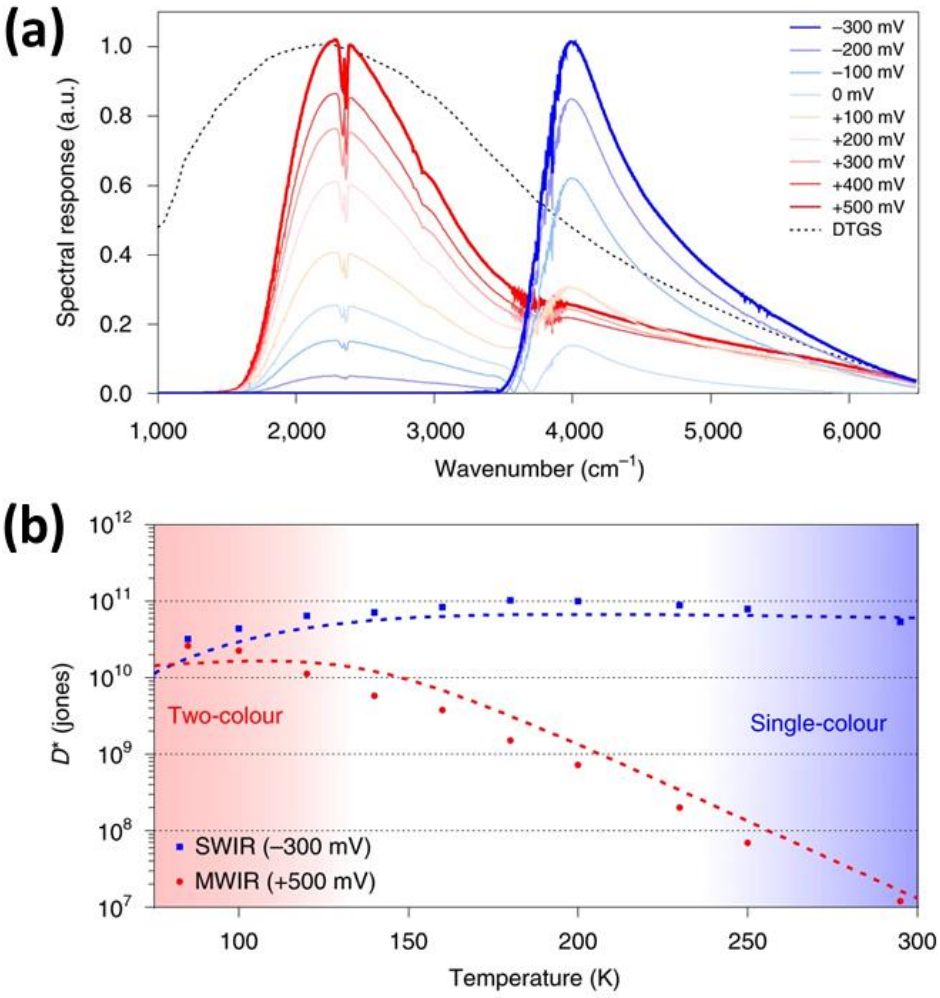

Figure 5-13 (a) *Bias dependence of the 80 K spectral response for the SWIR/MWIR dual-band photodetector.* ***(b)*** *Temperature dependence of the specific detectivity under optimal operating bias for photodetection in each spectral region.*

A demonstration of the infrared imaging capabilities with the dual-band detector are presented in Fig. 5-14. Shown in Fig. 5-14(a), the single-element camera setup consists of a dual-band detector operating at 80 K and an infrared lens, here BaF_2, that is rastered along the x and y axis while the signal is measured at each coordinate. A data acquisition system processes the output signals and coordinates to reconstruct an image. Here the image resolution is 75×500 (H×L) and provides a first look at the potential for dual-band imaging with HgTe CQDs. Single-band detection is enabled by fixing the external bias for either SWIR or MWIR detection. For SWIR imaging, a tungsten lamp was used as the light source. Such imaging where an external light source is required is referred to as active imaging. In the SWIR, active imaging captures images with qualities like visible imaging. As shown in Fig. 5-14(b), the visible (top) and SWIR (bottom) images share common information about the textures of the objects, but the SWIR can also see through the silicon wafer as Si is transparent to light beyond 1 μm. SWIR imaging can provide chemical or material information as different chemicals have different absorption in the SWIR and appear lighter or darker, as shown in Fig. 5-14(d) for a series of common solvents. Fig. 5-14(c) highlights the difference in information between a MWIR image that provides thermal information but lacks quality spatial information and a SWIR image where the facial features can be well resolved. Active SWIR and thermal MWIR can also act together to provide spatial, chemical, and thermal information for added value as shown in Fig. 5-14(e).

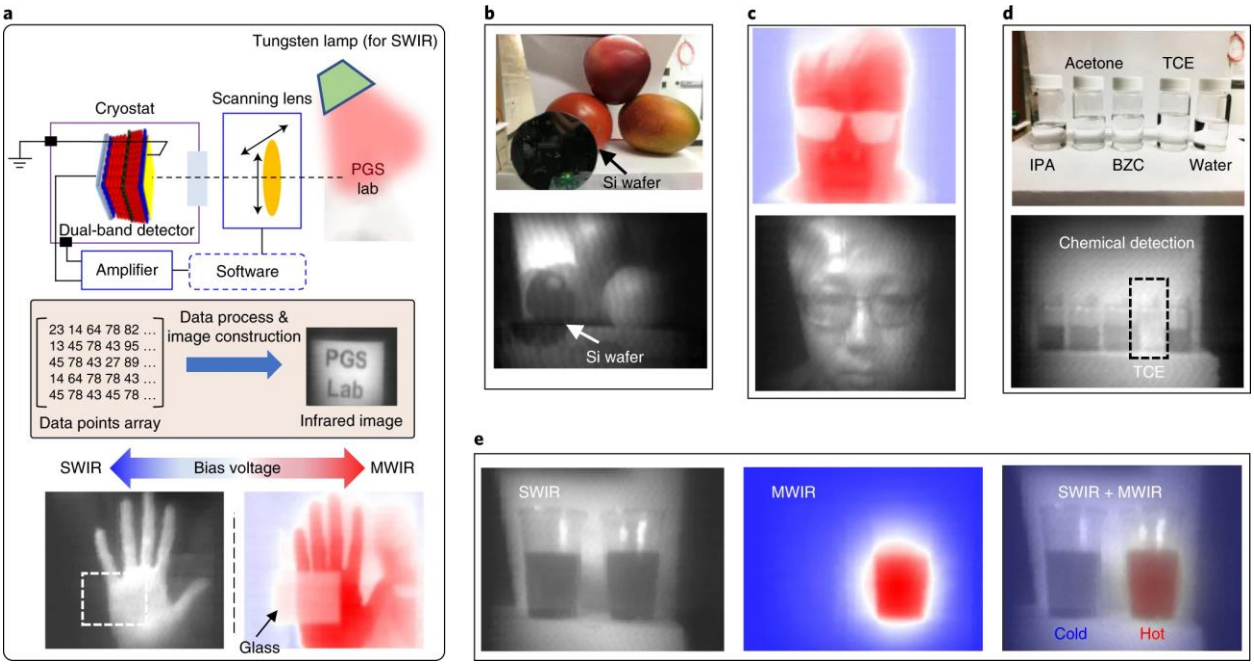

Figure 5-14 (a) *Experimental setup for single pixel camera imaging.* ***(b)*** *Short-wave infrared (SWIR) imaging of fruit and a silicon wafer illuminated by a tungsten lamp. The silicon is transparent in the SWIR (bottom) but not in the visible image.(top)* ***(c)*** *Mid-wave infrared (MWIR) thermal image (top) and SWIR (bottom) image of human face.* ***(d)*** *Visible (top) and SWIR (bottom) images of a solvent series illuminated by a tungsten lamp.* ***(e)*** *SWIR (left), MWIR (center), and superimposed SWIR/MWIR (right) images of two cups containing either hot or cold water. The thermal images are presented in a blue (cold) to red (hot) false color scale.*

Dual-band detection can also be used for remote detection of hot objects. For objects at temperatures of at least 400°C, as the object becomes hotter, the amount of SWIR light emitted increases while the MWIR light emitted decreases. Therefore, given a calibration curve for the ratio of SWIR/MWIR light as a function of blackbody temperature, the object temperature can be determined. For the dual-band detector, this means taking the ratio of the SWIR/MWIR signal output by the detector that will correspond to the temperature of the object. The calibration of the detector is performed by measuring the ratio of the SWIR/MWIR signals for a series of blackbody temperatures, like the setup shown in Fig. 5-15(a). Fig. 5-15(b) exemplifies the difference in the

ratio of the SWIR/MWIR signal for a series of hot objects, and Fig. 5-15(c) shows both a calibration curve and the measurement of temperatures for a soldering iron and heat gun at high (H) and low (L) setting. The ratio of the SWIR/MWIR signal could measure object temperatures up to 1 m away without a lens (Fig. 5-15(d)) and at operating frequencies as fast as 100 kHz (Fig. 5-15(e)), thanks to the fast response times of the individual photodiodes.

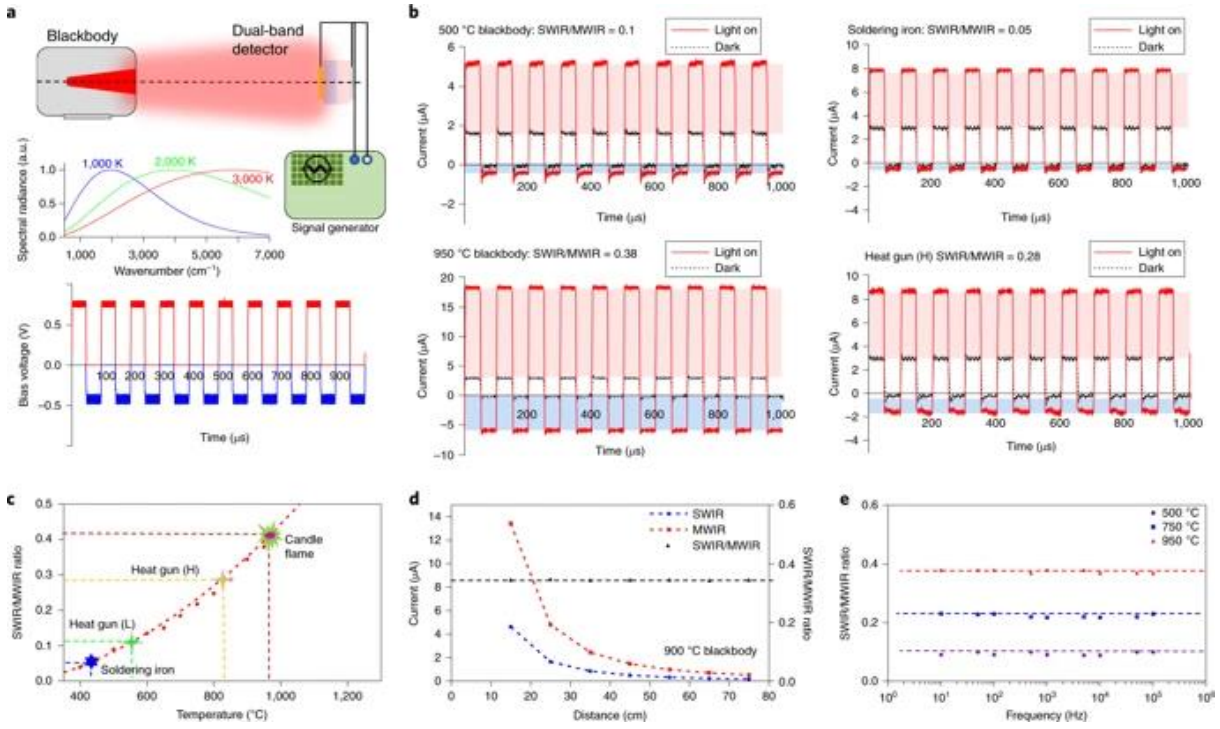

Figure 5-15 (a) *Experimental setup for calibrating the dual-band photodetector for remote infrared sensing. A calibrated blackbody was used with radiation incident on the photodetector, which was operated at a frequency set by the function generator.* ***(b)*** *Signal due to the operation of the photodetector in the SWIR (blue) and MWIR (red) operating modes. The ratio of the response at each operating mode was measured for a (top, left) 500°C blackbody, (bottom, left) 950°C blackbody, (top, right) soldering iron, and (bottom, right) heat gun at high (H) heat.* ***(c)*** *Calibration curve of the SWIR/MWIR signal ratio to the temperature of a source for remote temperature sensing.* ***(d)*** *Dependence of the SWIR signal (blue), MWIR signal (red), and SWIR/MWIR ratio (black) signal on the object distance from the detector.* ***(e)*** *Ratio of the SWIR/MWIR signals measured as a function of operation biasing frequency, demonstrating the fast response of the dual-band photodetector up to operation at 100 kHz.*

Though only SWIR/MWIR dual-band detection and imaging was demonstrated here, the application of CQDs to other types of infrared dual-band imaging such as SWIR/SWIR, MWIR/MWIR, LWIR/LWIR, SWIR/LWIR, and MWIR/LWIR is made possible by this work. Extending the application to LWIR detection would first require improvements on the LWIR HgTe CQD synthesis and a demonstration of a LWIR photodiode based on HgTe CQDs.

5.4 Summary

HgTe CQDs present a unique opportunity for the development of next-generation infrared imaging technologies. Compared to the epitaxial processes used today, HgTe CQDs leverage solution processing for scalable production of imaging systems. Specifically, two or more different sizes of HgTe CQD solutions can be integrated onto silicon electronics in an additive manufacturing process.

The development of the inverted HgTe CQD photodiode was a key step in the realization of a HgTe CQD dual-band infrared photodiode. Inverted polarity photodiodes were realized by introducing doped Bi_2Se_3 nanoparticles as the n-type layer in the HgTe CQD heterojunction and a $HgCl_2$-methanol processing step. Together, these modifications improved the device rectification and detection sensitivity with performance on par with previously reported normal HgTe CQD photodiodes. Then, the normal type and inverted type photodiodes were integrated into a two-terminal dual-band infrared photodetector designed for shortwave and mid-wave infrared photodetection.

The two-terminal photodetector consisted of back-to-back photodiodes where changing the bias switched the detection from MWIR to SWIR sensing. The advantage to this design is both the

reduced electrical demands of the integrated circuit and simplified processing requirements for operation and production. A first look at infrared imaging with a HgTe CQD dual-band photodetector was presented alongside a demonstration of its remote temperature sensing capabilities. In principle, the design used here is generalizable for dual-band detection in other spectral regions by simply changing the CQDs in the absorber layers. Future work on multi-terminal back-to-back photodiodes or two-terminal tandem photodiodes for simultaneous multi-band photodetection will be beneficial to the development of HgTe CQD infrared photodetectors. Vitally important is increasing the operating temperature of the photodetector and reducing spectral crosstalk (*i.e.* overlap in photoresponse between spectral regions) to bring the HgTe CQD multi-band photodetectors on par with epitaxial II-VI and III-V technologies.

Chapter 6 Future Direction and Conclusion

6.1 Future Direction

High mobility HgTe colloidal quantum dots

For the HgTe CQD photodiodes described in Chapter 3, the quantum efficiency of the photodetector MWIR response at room temperature was typically on the order of 1%. Improvement of the efficiency is limited by the diffusion lengths of charge carriers, which are much shorter than the thickness of the film at high operating temperatures. However, decreasing the thickness of the film will lead to losses in the absorption. Therefore, there is a tradeoff between charge collection efficiency and absorption in CQD thin films. The diffusion length is defined as $L_D = \sqrt{\frac{\mu k_b T}{q}\tau}$, proportional to the charge carrier mobility, μ. Then, increasing the mobility of the charge carriers in HgTe CQD films is expected to improve the high temperature operation, assuming the carrier lifetime is not adversely affected by the means of enhancing the mobility. Indeed, HgTe CQDs with mobility >1 cm^2/Vs realized with a polar phase ligand exchange[159] demonstrated an 8-fold improvement of the specific detectivity up to 7×10^7 Jones at room temperature for a photoconductive device.[93] The next step then is to integrate these high mobility HgTe CQDs into the photodiode designs to realize high operating temperature MWIR detectors. An 8-fold improvement in the performance of the HgTe CQD photodiodes will realize $D^* > 10^{10}$ Jones at operating temperatures that are accessible by low-power thermoelectric coolers.

Doping in HgTe colloidal quantum dot films

The success of much of the work described in this thesis is due to the discovery of the solid-state cation exchange process that underlies the device designs of Chapters 3, 4, and 5. The

utility and contribution of such a simple processing step to the robustness of the HgTe CQD photodiode operation cannot be understated. Of course, there is still much to improve in the way of learning to manipulate this process and predict the change in the performance of the HgTe CQD photodiodes.

Beyond Ag_2Te nanoparticles, other metal tellurides such as Cu_2Te and Sb_2Te_3 with solubility constants larger than HgTe might also be investigated as sacrificial host materials for the metal dopant ions.[119] The cation exchange with Sb_2Te_3 is particularly interesting as a method for n-type doping HgTe CQD films with aliovalent Sb^{3+} ions and extending the solid-state cation exchange process for designing n-type HgTe CQD films. Thus, changing the metal telluride layer is one direction for investigating the differences in doping of HgTe CQD films by solid-state cation exchange.

The solid-state cation exchange process might also be used to explore different HgTe CQD heterojunctions that are challenging to realize directly. For example, in Chapter 5, heterojunctions of HgTe-Bi_2Te_3 were considered for the inverted photodiode design. However, the Bi_2Te_3 nanoparticles solutions were not suitable for making quality thin films. Instead, the $HgCl_2$ solution in the solid-state cation exchange could be replaced by a Bi salt solution to convert the Ag_2Te to n-type Bi_2Te_3 and, ideally, form a Bi_2Se_3-HgTe CQD heterojunction diode.

The solid-state cation exchange is only one method for doping HgTe CQDs and the control of the doping is limited. Beyond this, non-aggregated HgTe CQD doping is directly tunable with both the size of the nanocrystal[89] and by polar ligand exchange into different concentrations of $HgCl_2$ polar ligand solutions.[93] Together, these processes allow for control of the n-type doping in

the solution phase. Throughout this work, EdT/HCl/IPA was commonly used as the crosslinker, but different ligand solutions might also be considered to tune the doping of the HgTe CQD films.[44]

Clearly, many paths may be taken to investigate the doping in HgTe CQD films and its effect on the photodiode performance. To guide the investigative work, simulation and modeling of the HgTe CQD photodiodes would be immensely beneficial. Modeling of HgCdTe photodetectors has led to the discovery of unique device designs to reduce recombination and increase the overall performance.[160–162] Similarly, a 1D numerical model of the HgTe CQD photodiodes would provide insights into the doping techniques that may lead to an optimal infrared detector at high operating temperatures.

Enhanced absorption in thin films

Due to the thin film thickness of the HgTe CQDs, much of the incident light is not absorbed, leading to low quantum efficiencies, especially at high temperature operation. The goal then is to enhance the absorption such that the film might also be made thinner to enhance the charge collection efficiency and improve high temperature operation in the mid-wave infrared. In Chapter 3, a Fabry-Perot cavity and plasmonic metal disks were integrated into a photodiode to increase the absorption in the film nearly 8-fold.[163] The enhanced absorption in the photodiode resulted in a 3-fold improvement of the specific detectivity at all operating temperatures and the highest reported quantum efficiency of 45% for a HgTe CQD photodiode in the mid-wave infrared operating at 85 K. In these photodiodes, the film thickness was held constant at 400 nm, still much thicker than the diffusion length at high temperatures. One direction then for MWIR HgTe CQD photodetectors is to integrate the cavity and plasmonic absorbers into thinner film devices, possibly

composed of high mobility HgTe CQDs,[159] such that both the absorption and charge collection are enhanced for greater quantum efficiency at higher operating temperatures.

The room temperature quantum efficiency of the shortwave infrared photodiodes described in Chapter 4 is already quite high at ~50% for a cutoff wavelength of 2.5 μm. For a thin film device, such a high quantum efficiency would imply the photodiode performance is limited by the absorption in the film. Therefore, optical enhancement of the SWIR HgTe CQD photodiode is an obvious direction for improving the overall performance. Indeed, the integration of a cavity into the photodiode stack enhanced the detectivity by 7-fold up to 7.5×10^{10} Jones at 2.25 μm and operating temperature of 300 K.[164] A 7-fold enhancement of the photodiodes described in Chapter 4 would lead to HgTe CQD photodiodes with quantum efficiency and specific detectivity exceeding the commercial extended InGaAs technologies.

<u>High quantum yield HgTe colloidal quantum dots</u>

The most significant challenge HgTe CQDs face is the low photoluminescence quantum yield. The specific detectivity of a HgTe CQD detector scales as the square root of the radiative fraction, *i.e.* $D^* \alpha \sqrt{f_c}$,[19] and would lead to significant improvements as the radiative fraction approaches unity. However, the quantum yield of HgTe CQDs is low, especially in the MWIR.[165] The photoluminescence is reduced by non-radiative processes such as energy transfer to the high frequency vibrations of the organics ligands[166] or longitudinal optical phonons at the nanocrystal surface.[167] Improvements in the visible photoluminescence for colloidal quantum dots have followed from either passivating the surface with inorganic ligands[168] or a shell material.[169] However, improving the HgTe CQD quantum yield by such methods has seen limited success.[170]

While researchers continue to address these limitations and identify opportunities for improving the photoluminescence, the near-term improvements in the detectivity are expected to come from better photodiode design through doping control, increasing the mobility, and enhancing the absorption in HgTe CQD thin films.

Long-wave infrared detection with HgTe CQDs

Long-wave infrared photodetection with HgTe CQDs is much less explored than the shortwave and mid-wave detectors. Detection up to 12 μm was first demonstrated in 2014 with a photoconductive device[27] and later up to 9.5 μm in a multi-spectral photoconductive detector.[138] Just as with mid-wave infrared detection, HgTe CQDs in the long-wave infrared should, theoretically, achieve higher operating temperatures than the epitaxial technologies owing to the lower Auger coefficient in colloidal quantum dots compared to bulk HgCdTe.[29] Currently, the limitation to the development of LWIR HgTe CQD photodetectors is the synthesis, which yields HgTe CQDs with broad size distributions and broad absorption that is detrimental to device operation.[27,28,171] If the synthesis of monodisperse HgTe CQDs with a reasonably sharp absorption edge in the LWIR can be realized, then the photodiode designs described in Chapters 3 and 5 will likely extend to HgTe CQDs to enable LWIR single- and dual-band detectors.

An alternative direction for LWIR detection is to use the intraband absorption of the doped, non-aggregating HgTe CQDs.[89] For sizes of HgTe CQDs greater than 8 nm in diameter, the intraband absorption peaks in the LWIR and intraband detection might be possible.[172] Intraband HgSe CQDs were shown to have suppressed Auger recombination[173] and this effect likely translates to the intraband transition of HgTe CQDs. The complete suppression of Auger

recombination with ambiently doped HgTe CQDs could then lead to higher temperature operation of LWIR photodetectors.

6.2 Conclusion

Chapter 1 introduced the shortwave, mid-wave, and long-wave infrared spectral regions, and the figures-of-merit for infrared photodetectors relevant to the work of this thesis. A brief review of the bulk epitaxial technologies was provided to motivate the advantages of HgTe colloidal quantum dot infrared detectors in terms of manufacturability. More specifically, HgTe CQDs were highlighted for the potential advantages in performance and operating temperature due to theoretically predicted reduced Auger recombination.

A strategy for improving the performance of HgTe CQD photodiodes was described and set into motion in Chapters 2 and 3. The focus was on improving the current rectifying behavior of the photodiodes using charge transport layers and doped HgTe CQDs. The success with the charge transport layers was marginal while the homojunction between p-type HgTe and n-type non-aggregated HgTe[89] showed greater promise with the exception of a temperature-dependent polarity inversion. Finally, strongly rectifying photodiodes were formed with the introduction of a solid-state cation exchange process wherein Ag-doped HgTe thin films are the result of a Hg cation exchange on Ag_2Te nanoparticle thin films. A preliminary description of the HgTe CQD photodiodes as a one-sided abrupt junction diode provides a starting point for understanding the physics and for future work investigating methods for manipulating the doping guided by numerical models.

In Chapter 4, the solid-state cation exchange process was implemented in an extended shortwave infrared HgTe CQD photodiode, and the figures-of-merit were on par with commercial epitaxial technologies. Interestingly, the performance of the extended SWIR detector was enhanced by soaking each layer of HgTe CQD in $HgCl_2$ solution before crosslinking. The result of the process was an improved photoluminescence concurrent with the reduction in the noise, ultimately leading to high performance detectors. It was reported that the metal halide ligands can enhance the quality of II-VI colloidal quantum dots,[119] and the results here suggest further investigation of different metal halides might lead to optimized extended SWIR performance.

The significance of $HgCl_2$ cannot be understated here. In Chapter 5, the realization of inverted photodiodes with performance equivalent to the normal type photodiodes relied on a $HgCl_2$ soaking step in addition to using a n-type Bi_2Se_3 nanoparticle thin film. With designs for both the normal and inverted photodiode, this work culminates in the demonstration of SWIR/MWIR dual-band detection with a two-terminal photodetector operating at 80 K. The processes developed in Chapters 3 and 5 enable the design of inverted and normal photodiodes for SWIR and MWIR detection; therefore, it is reasonable to think that these designs might be general to HgTe CQD photodiodes and apply to LWIR HgTe CQDs. Tunable infrared detection from 1-12 μm, the potential to operate at higher temperatures, and the low-cost, scalable solution processing altogether make HgTe CQDs an emerging and versatile technology for infrared photodetection and imaging.

Bibliography

1. Case, T. W. Notes on the change of resistance of certain substances in light. *Phys. Rev.* **9**, 305–310 (1917).

2. Case, T. W. 'thalofide Cell'-A new photo-electric substance. *Phys. Rev.* **15**, 289–292 (1920).

3. Rogalski, A. History of infrared detectors. *Opto-electronics Rev.* **20**, 279–308 (2012).

4. Lawson, W. D., Nielsen, S., Putley, E. H. & Young, A. S. Preparation and properties of HgTe and mixed crystals of HgTe-CdTe. *J. Phys. Chem. Solids* **9**, 325–329 (1959).

5. Rogalski, A. HgCdTe infrared detector material: history, status and outlook. *Reports Prog. Phys.* **68**, 2267 (2005).

6. Rogalski, A. HgCdTe photodetectors. in *Mid-infrared Optoelectronics* 235–335 (Elsevier, 2020). doi:10.1016/b978-0-08-102709-7.00007-3

7. Tennant, W. E., Lee, D., Zandian, M., Piquette, E. & Carmody, M. MBE HgCdTe technology: A very general solution to IR detection, described by 'rule 07', a very convenient heuristic. *J. Electron. Mater.* **37**, 1406–1410 (2008).

8. Avery, D. G., Goodwin, D. W. & Rennie, M. A. E. New infra-red detectors using indium antimonide. *J. Sci. Instrum.* **34**, 394 (1957).

9. Leheny, R. F., Nahory, R. E. & Pollack, M. A. In0.53Ga0.47As p-i-n photodiodes for long-wavelength fibre-optic systems. *Electron. Lett.* **15**, 713–715 (1979).

10. Pearsall, T. P. Papers: Ga047ln053As: A Ternary Semiconductor for Photodetector Applications. *IEEE J. Quantum Electron.* **16**, 709–720 (1980).

11. Pearsall, T., Piskorski, M., Brochet, A. & Chevrier, J. A Ga0.47In0.53As/InP Heterophotodiode with Reduced Dark Current. *IEEE J. Quantum Electron.* **17**, 255–259 (1981).

12. Ting, D. Z. *et al.* Advances in III-V semiconductor infrared absorbers and detectors. *Infrared Phys. Technol.* **97**, 210–216 (2019).

13. Norton, P. R., Campbell III, J. B., Horn, S. B. & Reago, D. A. Third-generation infrared imagers. in *Infrared Technology and Applications XXVI* (eds. Andresen, B. F., Fulop, G. F. & Strojnik, M.) **4130**, 226 (SPIE, 2000).

14. Move Over, CMOS: Here Come Snapshots by Quantum Dots - IEEE Spectrum. Available at: https://spectrum.ieee.org/consumer-electronics/audiovideo/move-over-cmos-here-

come-snapshots-by-quantum-dots. (Accessed: 12th May 2020)

15. Khodayar, F., Sojasi, S. & Maldague, X. Infrared thermography and NDT: 2050 horizon. *Quantitative InfraRed Thermography Journal* **13**, 210–231 (2016).

16. Sousa, E. *et al.* A review on the application of medical infrared thermal imaging in hands. *Infrared Physics and Technology* **85**, 315–323 (2017).

17. Malchow, D., Battaglia, J., Brubaker, R. & Ettenberg, M. High speed short wave infrared (SWIR) imaging and range gating cameras. in *Thermosense XXIX* **6541**, 654106 (SPIE, 2007).

18. Livache, C., Martinez, B., Goubet, N., Ramade, J. & Lhuillier, E. Road map for nanocrystal based infrared photodetectors. *Frontiers in Chemistry* **6**, 575 (2018).

19. Guyot-Sionnest, P., Ackerman, M. M. & Tang, X. Colloidal quantum dots for infrared detection beyond silicon. *Journal of Chemical Physics* **151**, 060901 (2019).

20. LaPierre, R. R., Robson, M., Azizur-Rahman, K. M. & Kuyanov, P. A review of III–V nanowire infrared photodetectors and sensors. *J. Phys. D. Appl. Phys.* **50**, 123001 (2017).

21. Amani, M., Regan, E., Bullock, J., Ahn, G. H. & Javey, A. Mid-Wave Infrared Photoconductors Based on Black Phosphorus-Arsenic Alloys. *ACS Nano* **11**, 11724–11731 (2017).

22. Wise, F. W. Lead salt quantum dots: The limit of strong quantum confinement. *Acc. Chem. Res.* **33**, 773–780 (2000).

23. Kagan, C. R., Lifshitz, E., Sargent, E. H. & Talapin, D. V. Building devices from colloidal quantum dots. *Science (80-.).* **353**, (2016).

24. Sze, S. M. & Ng, K. K. Appendix F Properties of Important Semiconductors. in *Physics of Semiconductor Devices* 789–789 (John Wiley & Sons, Inc., 2006). doi:10.1002/9780470068328.app6

25. Chen, M. & Guyot-Sionnest, P. Reversible Electrochemistry of Mercury Chalcogenide Colloidal Quantum Dot Films. *ACS Nano* **11**, 4165–4173 (2017).

26. Abdelazim, N. M. *et al.* Room Temperature Synthesis of HgTe Quantum Dots in an Aprotic Solvent Realizing High Photoluminescence Quantum Yields in the Infrared. *Chem. Mater.* **29**, 7859–7867 (2017).

27. Keuleyan, S. E., Guyot-Sionnest, P., Delerue, C. & Allan, G. Mercury telluride colloidal quantum dots: Electronic structure, size-dependent spectra, and photocurrent detection up to 12 μm. *ACS Nano* **8**, 8676–8682 (2014).

28. Goubet, N. *et al.* Terahertz HgTe Nanocrystals: Beyond Confinement. *J. Am. Chem. Soc.* **140**, 5033–5036 (2018).

29. Melnychuk, C. & Guyot-Sionnest, P. Slow Auger Relaxation in HgTe Colloidal Quantum Dots. *J. Phys. Chem. Lett.* **9**, 2208–2211 (2018).

30. Dutta, P. & Horn, P. M. Low-frequency fluctuations in solids: 1f noise. *Rev. Mod. Phys.* **53**, 497–516 (1981).

31. Shockley, W. & Queisser, H. J. Detailed balance limit of efficiency of p-n junction solar cells. *J. Appl. Phys.* **32**, 510–519 (1961).

32. Dereniak, E. L. & Boreman, G. D. (Glenn D. . *Infrared detectors and systems*. (Wiley, 1996).

33. Rogach, A. *et al.* Colloidally Prepared HgTe Nanocrystals with Strong Room-Temperature Infrared Luminescence. *Adv. Mater.* **11**, 552–555 (1999).

34. Kim, H. *et al.* Photocurrent mechanism in a hybrid system of 1-thioglycerol-capped HgTe nanoparticles. *Appl. Phys. Lett.* **83**, 4619–4621 (2003).

35. Kim, H. *et al.* Optoelectronic characteristics of close-packed HgTe nanoparticles in the infrared range. *Solid State Commun.* **137**, 315–319 (2006).

36. Günes, S. *et al.* Hybrid Solar Cells Using HgTe Nanocrystals and Nanoporous TiO2 Electrodes. *Adv. Funct. Mater.* **16**, 1095–1099 (2006).

37. Böberl, M., Kovalenko, M. V., Gamerith, S., List, E. J. W. & Heiss, W. Inkjet-printed nanocrystal photodetectors operating up to 3 μm wavelengths. *Adv. Mater.* **19**, 3574–3578 (2007).

38. Kovalenko, M. V. *et al.* Colloidal HgTe nanocrystals with widely tunable narrow band gap energies: From telecommunications to molecular vibrations. *J. Am. Chem. Soc.* **128**, 3516–3517 (2006).

39. Keuleyan, S., Lhuillier, E., Brajuskovic, V. & Guyot-Sionnest, P. Mid-infrared HgTe colloidal quantum dot photodetectors. *Nat. Photonics* **5**, 489–493 (2011).

40. Keuleyan, S., Lhuillier, E. & Guyot-Sionnest, P. Synthesis of colloidal HgTe quantum dots for narrow mid-IR emission and detection. *J. Am. Chem. Soc.* **133**, 16422–16424 (2011).

41. Lhuillier, E., Keuleyan, S., Rekemeyer, P. & Guyot-Sionnest, P. Thermal properties of mid-infrared colloidal quantum dot detectors. *J. Appl. Phys.* **110**, (2011).

42. Sze, S. M. & Ng, K. K. p - n Junctions. in *Physics of Semiconductor Devices* 77–133 (John Wiley & Sons, Inc., 2006). doi:10.1002/9780470068328.ch2

43. Guyot-Sionnest, P. & Roberts, J. A. Background limited mid-infrared photodetection with photovoltaic HgTe colloidal quantum dots. *Appl. Phys. Lett.* **107**, (2015).

44. Brown, P. R. *et al.* Energy level modification in lead sulfide quantum dot thin films through ligand exchange. *ACS Nano* **8**, 5863–5872 (2014).

45. Kittel, C. Surface and Interface Physics. in *Introduction to Solid State Physics* 555–586 (Wiley, 1996).

46. Melitz, W., Shen, J., Kummel, A. C. & Lee, S. Kelvin probe force microscopy and its application. *Surface Science Reports* **66**, 1–27 (2011).

47. Derry, G. N., Kern, M. E. & Worth, E. H. Recommended values of clean metal surface work functions. *J. Vac. Sci. Technol. A Vacuum, Surfaces, Film.* **33**, 060801 (2015).

48. Hölzl, J. & Schulte, F. K. Work function of metals. in 1–150 (Springer, Berlin, Heidelberg, 1979). doi:10.1007/bfb0048919

49. Xiong, G. *et al.* Photoemission electron microscopy of TiO2 anatase films embedded with rutile nanocrystals. *Adv. Funct. Mater.* **17**, 2133–2138 (2007).

50. Kashiwaya, S. *et al.* The Work Function of TiO2. *Surfaces* **1**, 73–89 (2018).

51. Gao, J. *et al.* N-type transition metal oxide as a hole extraction layer in PbS quantum dot solar cells. *Nano Lett.* **11**, 3263–3266 (2011).

52. Yokokura, Y. *et al.* Control of indium tin oxide anode work function modified using Langmuir-Blodgett monolayer for high-efficiency organic photovoltaics. *AIP Adv.* **7**, 085321 (2017).

53. Chen, M. & Guyot-Sionnest, P. Reversible Electrochemistry of Mercury Chalcogenide Colloidal Quantum Dot Films. *ACS Nano* **11**, 4165–4173 (2017).

54. Szydlo, N. & Poirier, R. I-V and C-V characteristics of Au/TiO2 Schottky diodes. *J. Appl. Phys.* **51**, 3310–3312 (1980).

55. Liu, G., Jaegermann, W., He, J., Sundström, V. & Sun, L. XPS and UPS characterization of the TiO2/ZnPcGly heterointerface: Alignment of energy levels. *J. Phys. Chem. B* **106**, 5814–5819 (2002).

56. Marques, F. C. & Jasieniak, J. J. Ionization potential and electron attenuation length of titanium dioxide deposited by atomic layer deposition determined by photoelectron

spectroscopy in air. *Appl. Surf. Sci.* **422**, 504–508 (2017).

57. Cahen, D., Hodes, G., Grätzel, M., Guillemoles, J. F. & Riess, I. Nature of Photovoltaic Action in Dye-Sensitized Solar Cells. *J. Phys. Chem. B* **104**, 2053–2059 (2000).

58. Lehoczky, S. L., Lederich, R. J. & Bellina, J. J. Oxidation of thin titamium films in ambient conditions. *Thin Solid Films* **55**, 125–135 (1978).

59. Bareiß, M. *et al.* Ultra-thin titanium oxide. *Appl. Phys. Lett.* **101**, 083113 (2012).

60. Bak, T., Nowotny, J. & Nowotny, M. K. Defect disorder of titanium dioxide. *J. Phys. Chem. B* **110**, 21560–21567 (2006).

61. Lu, G., Bernasek, S. L. & Schwartz, J. Oxidation of a polycrystalline titanium surface by oxygen and water. *Surf. Sci.* **458**, 80–90 (2000).

62. Sundqvist, A., Sandberg, O. J., Nyman, M., Smått, J. H. & Österbacka, R. Origin of the S-Shaped JV Curve and the Light-Soaking Issue in Inverted Organic Solar Cells. *Adv. Energy Mater.* **6**, 1502265 (2016).

63. Lattante, S. Electron and hole transport layers: Their use in inverted bulk heterojunction polymer solar cells. *Electronics (Switzerland)* **3**, 132–164 (2014).

64. Shin, S. S., Lee, S. J. & Seok, S. Il. Metal Oxide Charge Transport Layers for Efficient and Stable Perovskite Solar Cells. *Advanced Functional Materials* **29**, 1900455 (2019).

65. Jagtap, A. *et al.* Design of a Unipolar Barrier for a Nanocrystal-Based Short-Wave Infrared Photodiode. *ACS Photonics* **5**, 4569–4576 (2018).

66. Jagtap, A. *et al.* Short Wave Infrared Devices Based on HgTe Nanocrystals with Air Stable Performances. *J. Phys. Chem. C* **122**, 14979–14985 (2018).

67. Huo, N., Gupta, S. & Konstantatos, G. MoS2–HgTe Quantum Dot Hybrid Photodetectors beyond 2 μm. *Adv. Mater.* **29**, 1606576 (2017).

68. Kim, G. *et al.* Overcoming the light-soaking problem in inverted polymer solar cells by introducing a heavily doped titanium sub-oxide functional layer. *Adv. Energy Mater.* **5**, 1401298 (2015).

69. Trost, S. *et al.* Overcoming the 'light-soaking' issue in inverted organic solar cells by the use of al:zno electron extraction layers. *Adv. Energy Mater.* **3**, 1437–1444 (2013).

70. Trost, S. *et al.* Tin Oxide (SnOx) as Universal 'light-Soaking' Free Electron Extraction Material for Organic Solar Cells. *Adv. Energy Mater.* **5**, 1500277 (2015).

71. Ren, X. *et al.* Solution-processed Nb:SnO2 electron transport layer for efficient planar perovskite solar cells. *ACS Appl. Mater. Interfaces* **9**, 2421–2429 (2017).

72. Ke, W. *et al.* Effects of annealing temperature of tin oxide electron selective layers on the performance of perovskite solar cells. *J. Mater. Chem. A* **3**, 24163–24168 (2015).

73. Shin, S. S., Lee, S. J. & Seok, S. I. Exploring wide bandgap metal oxides for perovskite solar cells. *APL Mater.* **7**, 022401 (2019).

74. Tiwana, P., Docampo, P., Johnston, M. B., Snaith, H. J. & Herz, L. M. Electron mobility and injection dynamics in mesoporous ZnO, SnO 2, and TiO2 films used in dye-sensitized solar cells. *ACS Nano* **5**, 5158–5166 (2011).

75. Ke, W. *et al.* Lowerature solution-processed tin oxide as an alternative electron transporting layer for efficient perovskite solar cells. *J. Am. Chem. Soc.* **137**, 6730–6733 (2015).

76. Nishino, S., Okada, J., Kumazawa, K. & Mori, T. Modification of ionization potential of polyethylene dioxythiophene: Poly(styrene sulfonate) film by acid or base treatment. *Japanese J. Appl. Physics, Part 1 Regul. Pap. Short Notes Rev. Pap.* **46**, 7427–7431 (2007).

77. Koch, N., Elschner, A., Rabe, J. P. & Johnson, R. L. Work function independent hole-injection barriers between pentacene and conducting polymers. *Adv. Mater.* **17**, 330–335 (2005).

78. Fulghum, T. M., Taranekar, P. & Advincula, R. C. Grafting hole-transport precursor polymer brushes on ITO electrodes: Surface-initiated polymerization and conjugated polymer network formation of PVK. *Macromolecules* **41**, 5681–5687 (2008).

79. Yang, L., Yan, Y., Cai, F., Li, J. & Wang, T. Poly(9-vinylcarbazole) as a hole transport material for efficient and stable inverted planar heterojunction perovskite solar cells. *Sol. Energy Mater. Sol. Cells* **163**, 210–217 (2017).

80. Günes, S. *et al.* Hybrid solar cells using HgTe nanocrystals and nanoporous TiO2 electrodes. *Adv. Funct. Mater.* **16**, 1095–1099 (2006).

81. Bao, Z., Dodabalapur, A. & Lovinger, A. J. Soluble and processable regioregular poly(3-hexylthiophene) for thin film field-effect transistor applications with high mobility. *Appl. Phys. Lett.* **69**, 4108–4110 (1996).

82. Sirringhaus, H., Tessler, N. & Friend, R. H. Integrated optoelectronic devices based on conjugated polymers. *Science (80-.).* **280**, 1741–1744 (1998).

83. Osikowicz, W. *et al.* Energetics at Au top and bottom contacts on conjugated polymers.

Appl. Phys. Lett. **88**, 193504 (2006).

84. Kim, D. Y. *et al.* The effect of molybdenum oxide interlayer on organic photovoltaic cells. *Appl. Phys. Lett.* **95**, (2009).

85. Li, G., Chu, C. W., Shrotriya, V., Huang, J. & Yang, Y. Efficient inverted polymer solar cells. *Appl. Phys. Lett.* **88**, (2006).

86. Gao, J. *et al.* N-type transition metal oxide as a hole extraction layer in PbS quantum dot solar cells. *Nano Lett.* **11**, 3263–3266 (2011).

87. Irfan *et al.* Energy level evolution of air and oxygen exposed molybdenum trioxide films. *Appl. Phys. Lett.* **96**, (2010).

88. Meyer, J., Shu, A., Kröger, M. & Kahn, A. Effect of contamination on the electronic structure and hole-injection properties of MoO3 /organic semiconductor interfaces. *Appl. Phys. Lett.* **96**, (2010).

89. Shen, G., Chen, M. & Guyot-Sionnest, P. Synthesis of Nonaggregating HgTe Colloidal Quantum Dots and the Emergence of Air-Stable n-Doping. *J. Phys. Chem. Lett.* **8**, 2224–2228 (2017).

90. Jeong, K. S., Deng, Z., Keuleyan, S., Liu, H. & Guyot-Sionnest, P. Air-stable n-doped colloidal HgS quantum dots. *J. Phys. Chem. Lett.* **5**, 1139–1143 (2014).

91. Shen, G. & Guyot-Sionnest, P. HgS and HgS/CdS Colloidal Quantum Dots with Infrared Intraband Transitions and Emergence of a Surface Plasmon. *J. Phys. Chem. C* **120**, 11744–11753 (2016).

92. Deng, Z. & Guyot-Sionnest, P. Intraband Luminescence from HgSe/CdS Core/Shell Quantum Dots. *ACS Nano* **10**, 2121–2127 (2016).

93. Chen, M. *et al.* High Carrier Mobility in HgTe Quantum Dot Solids Improves Mid-IR Photodetectors. *ACS Photonics* **6**, 2358–2365 (2019).

94. Mocatta, D. *et al.* Heavily doped semiconductor nanocrystal quantum dots. *Science (80-.).* **332**, 77–81 (2011).

95. Sahu, A. *et al.* Electronic impurity doping in CdSe nanocrystals. *Nano Lett.* **12**, 2587–2594 (2012).

96. De Trizio, L. & Manna, L. Forging colloidal nanostructures via cation exchange reactions. *Chemical Reviews* **116**, 10852–10887 (2016).

97. Moon, G. D., Ko, S., Xia, Y. & Jeong, U. Chemical transformations in ultrathin

chalcogenide nanowires. *ACS Nano* **4**, 2307–2319 (2010).

98. Samal, A. K. & Pradeep, T. Hybrid A-B-A type nanowires through cation exchange. *Nanoscale* **3**, 4840–4847 (2011).

99. Wang, C.-W., Lin, Z.-H., Roy, P. & Chang, H.-T. Detection of mercury ions using silver telluride nanoparticles as a substrate and recognition element through surface-enhanced Raman scattering. *Front. Chem.* **1**, 20 (2013).

100. Philipp, P., Ngo, K. Q., Kieffer, J. & Wirtz, T. Silver Diffusion in Organic Optoelectronic Devices: Deposition-Related Processes versus Secondary Ion Mass Spectrometry Analysis Artifacts. *J. Phys. Chem. C* **119**, 23334–23341 (2015).

101. Marshall, A. R., Young, M. R., Nozik, A. J., Beard, M. C. & Luther, J. M. Exploration of Metal Chloride Uptake for Improved Performance Characteristics of PbSe Quantum Dot Solar Cells. *J. Phys. Chem. Lett.* **6**, 2892–2899 (2015).

102. Guyot-Sionnest, P., Ackerman, M. M. & Tang, X. Colloidal quantum dots for infrared detection beyond silicon. *Journal of Chemical Physics* **151**, 060901 (2019).

103. Kim, Y. *et al.* Nanoimprint-Transfer-Patterned Solids Enhance Light Absorption in Colloidal Quantum Dot Solar Cells. *Nano Lett.* **17**, 2349–2353 (2017).

104. Beck, F. J., Stavrinadis, A., Diedenhofen, S. L., Lasanta, T. & Konstantatos, G. Surface Plasmon Polariton Couplers for Light Trapping in Thin-Film Absorbers and Their Application to Colloidal Quantum Dot Optoelectronics. *ACS Photonics* **1**, 1197–1205 (2014).

105. Yifat, Y., Ackerman, M. & Guyot-Sionnest, P. Mid-IR colloidal quantum dot detectors enhanced by optical nano-antennas. *Appl. Phys. Lett.* **110**, 041106 (2017).

106. Tang, X., Ackerman, M. M. & Guyot-Sionnest, P. Acquisition of Hyperspectral Data with Colloidal Quantum Dots. *Laser Photon. Rev.* **13**, 1900165 (2019).

107. Ji, X. *et al.* Deep-level traps induced dark currents in extended wavelength In xGa1-xAs/InP photodetector. *J. Appl. Phys.* **114**, 224502 (2013).

108. Haddadi, A., Chevallier, R., Dehzangi, A. & Razeghi, M. Extended short-wavelength infrared nBn photodetectors based on type-II InAs/AlSb/GaSb superlattices with an AlAsSb/GaSb superlattice barrier. *Appl. Phys. Lett.* **110**, 101104 (2017).

109. Böberl, M., Kovalenko, M. V., Gamerith, S., List, E. J. W. & Heiss, W. Inkjet-Printed Nanocrystal Photodetectors Operating up to 3 μm Wavelengths. *Adv. Mater.* **19**, 3574–3578 (2007).

110. Chen, M. *et al.* Photocurrent Enhancement of HgTe Quantum Dot Photodiodes by Plasmonic Gold Nanorod Structures. *ACS Nano* **8**, 8208–8216 (2014).

111. Killilea, N. *et al.* Pushing PbS/Metal-Halide-Perovskite Core/Epitaxial-Ligand-Shell Nanocrystal Photodetectors beyond 3 μm Wavelength. *Adv. Funct. Mater.* **29**, 1807964 (2019).

112. Martinez, B. *et al.* HgTe Nanocrystal Inks for Extended Short-Wave Infrared Detection. *Adv. Opt. Mater.* **7**, 1900348 (2019).

113. Tang, X., Ackerman, M. M., Chen, M. & Guyot-Sionnest, P. Dual-band infrared imaging using stacked colloidal quantum dot photodiodes. *Nat. Photonics* **13**, 277–282 (2019).

114. Dong, C. *et al.* Long-Wavelength Lead Sulfide Quantum Dots Sensing up to 2600 nm for Short-Wavelength Infrared Photodetectors. *ACS Appl. Mater. Interfaces* **11**, 44451–44457 (2019).

115. Chen, M. *et al.* Mercury Telluride Quantum Dot Based Phototransistor Enabling High-Sensitivity Room-Temperature Photodetection at 2000 nm. *ACS Nano* **11**, 5614–5622 (2017).

116. Huo, N., Gupta, S. & Konstantatos, G. MoS2–HgTe Quantum Dot Hybrid Photodetectors beyond 2 μm. *Adv. Mater.* **29**, 1606576 (2017).

117. Özdemir, O., Ramiro, I., Gupta, S. & Konstantatos, G. High Sensitivity Hybrid PbS CQD-TMDC Photodetectors up to 2 μm. *ACS Photonics* **6**, 2381–2386 (2019).

118. Lhuillier, E., Keuleyan, S. & Guyot-Sionnest, P. Optical Properties of HgTe Colloidal Quantum Dots. *Nanotechnology* **23**, (2012).

119. Kirkwood, N. *et al.* Finding and Fixing Traps in II-VI and III-V Colloidal Quantum Dots: The Importance of Z-Type Ligand Passivation. *J. Am. Chem. Soc.* **140**, 15712–15723 (2018).

120. Guyot-Sionnest, P., Ackerman, M. M. & Tang, X. Colloidal quantum dots for infrared detection beyond silicon. *Journal of Chemical Physics* **151**, (2019).

121. Kumar, A., Sista, S. & Yang, Y. Dipole induced anomalous S-shape I-V curves in polymer solar cells. *J. Appl. Phys.* **105**, 094512 (2009).

122. Zhou, Y. *et al.* Direct correlation between work function of indium-tin-oxide electrodes and solar cell performance influenced by ultraviolet irradiation and air exposure. *Phys. Chem. Chem. Phys.* **14**, 12014–12021 (2012).

123. Zhang, Y.-G. *et al.* IGA-rule 17 for performance estimation of wavelength-extended

InGaAs photodetectors: validity and limitations. *Appl. Opt.* **57**, D141 (2018).

124. Tennant, W. E. ‘Rule 07’’ revisited: Still a good heuristic predictor of p/n HgCdTe photodiode performance? in *Journal of Electronic Materials* **39**, 1030–1035 (Springer, 2010).

125. Tang, X., Ackerman, M. M., Shen, G. & Guyot-Sionnest, P. Towards Infrared Electronic Eyes: Flexible Colloidal Quantum Dot Photovoltaic Detectors Enhanced by Resonant Cavity. *Small* **15**, 1804920 (2019).

126. Abedin, M. N. *et al.* Progress of multicolor single detector to detector array development for remote sensing. in *Infrared Spaceborne Remote Sensing XII* (ed. Strojnik, M.) **5543**, 239 (SPIE, 2004).

127. Blazejewski, E. R. Bias-switchable dual-band HgCdTe infrared photodetector. *J. Vac. Sci. Technol. B Microelectron. Nanom. Struct.* **10**, 1626 (1992).

128. Reine, M. B. *et al.* Independently accessed back-to-back HgCdTe photodiodes: A new dual-band infrared detector. *J. Electron. Mater.* **24**, 669–679 (1995).

129. Martyniuk, P., Madejczyk, P., Gawron, W. & Rutkowski, J. Demonstration of a Dual-Band Mid-Wavelength HgCdTe Detector Operating at Room Temperature. *J. Electron. Mater.* **47**, 5752–5758 (2018).

130. Ames, C. *et al.* High-performance SWIR/MWIR and MWIR/MWIR bispectral MCT detectors by AIM. in 28 (SPIE-Intl Soc Optical Eng, 2018). doi:10.1117/12.2304355

131. Haddadi, A., Chevallier, R., Chen, G., Hoang, A. M. & Razeghi, M. Bias-selectable dual-band mid-/long-wavelength infrared photodetectors based on InAs/InAs1-xSbx type-II superlattices. *Appl. Phys. Lett.* **106**, 011104 (2015).

132. Haddadi, A., Dehzangi, A., Chevallier, R., Adhikary, S. & Razeghi, M. Bias-selectable nBn dual-band long-/very long-wavelength infrared photodetectors based on InAs/InAs1-xSbx/AlAs1-xSbx type-II superlattices /639/301/1005/1009 /639/766/1130/2799 /128 /145 /144 /142/126 /120 article. *Sci. Rep.* **7**, 1–7 (2017).

133. Delaunay, P.-Y., Nosho, B. Z., Gurga, A. R., Terterian, S. & Rajavel, R. D. Advances in III-V based dual-band MWIR/LWIR FPAs at HRL. in *Infrared Technology and Applications XLIII* (eds. Andresen, B. F., Fulop, G. F., Hanson, C. M., Miller, J. L. & Norton, P. R.) **10177**, 101770T (SPIE, 2017).

134. Gunapala, S. D. *et al.* Demonstration of megapixel dual-band QWIP focal plane array. *IEEE J. Quantum Electron.* **46**, 285–293 (2010).

135. Colegrove, E. *et al.* Scalable ultrafast epitaxy of large-grain and single-crystal II-VI

semiconductors. *Sci. Rep.* **10**, 1–8 (2020).

136. Lee, B., Fan, D. & Forrest, S. R. A high throughput, linear molecular beam epitaxy system for reduced cost manufacturing of GaAs photovoltaic cells: will GaAs ever be inexpensive enough? *Sustain. Energy Fuels* **4**, 2035–2042 (2020).

137. Cryer, M. E. & Halpert, J. E. 300 nm Spectral Resolution in the Mid-Infrared with Robust, High Responsivity Flexible Colloidal Quantum Dot Devices at Room Temperature. *ACS Photonics* **5**, 3009–3015 (2018).

138. Tang, X., Tang, X. & Lai, K. W. C. Scalable Fabrication of Infrared Detectors with Multispectral Photoresponse Based on Patterned Colloidal Quantum Dot Films. *ACS Photonics* **3**, 2396–2404 (2016).

139. Gildart, L., Kline, J. M. & Mattox, D. M. Some semiconducting properties of bismuth trisulfide. *J. Phys. Chem. Solids* **18**, 286–289 (1961).

140. Jacob John, K., Pradeep, B. & Mathai, E. Electrical properties of bismuth selenide (Bi2Se3) thin films prepared by reactive evaporation. *Solid State Commun.* **85**, 879–881 (1993).

141. Zhao, L. D., Zhang, B.-P., Liu, W. S., Zhang, H. L. & Li, J.-F. Effects of annealing on electrical properties of n-type Bi2Te3 fabricated by mechanical alloying and spark plasma sintering. *J. Alloys Compd.* **467**, 91–97 (2009).

142. Rath, A. K., Bernechea, M., Martinez, L. & Konstantatos, G. Solution-processed heterojunction solar cells based on p-type PbS quantum dots and n-type Bi 2S 3 Nanocrystals. *Adv. Mater.* **23**, 3712–3717 (2011).

143. Kašparová, J. *et al.* n-type to p-type crossover in quaternary Bi xSb yPb zSe 3 single crystals. *J. Appl. Phys.* **97**, 103720 (2005).

144. Ramezani, M., Sobhani-Nasab, A. & Davoodi, A. Bismuth selenide nanoparticles: simple synthesis, characterization, and its light harvesting applications in the presence of novel precursor. *J. Mater. Sci. Mater. Electron.* **26**, 5440–5445 (2015).

145. Webber, D. H. & Brutchey, R. L. Photochemical synthesis of bismuth selenide nanocrystals in an aqueous micellar solution. *Inorg. Chem.* **50**, 723–725 (2011).

146. Stavila, V. *et al.* Wet-chemical synthesis and consolidation of stoichiometric bismuth telluride nanoparticles for improving the thermoelectric figure-of-merit. *ACS Appl. Mater. Interfaces* **5**, 6678–6686 (2013).

147. Mishra, S. K., Satpathy, S. & Jepsen, O. Electronic structure and thermoelectric properties of bismuth telluride and bismuth selenide. *J. Phys. Condens. Matter* **9**, 461–470 (1997).

148. Zhang, H. *et al.* Topological insulators in Bi 2 Se 3, Bi 2 Te 3 and Sb 2 Te 3 with a single Dirac cone on the surface. *Nat. Phys.* **5**, 438–442 (2009).

149. Kong, D. *et al.* Few-Layer Nanoplates of Bi $_2$ Se $_3$ and Bi $_2$ Te $_3$ with Highly Tunable Chemical Potential. *Nano Lett.* **10**, 2245–2250 (2010).

150. Sun, Y. *et al.* Atomically Thick Bismuth Selenide Freestanding Single Layers Achieving Enhanced Thermoelectric Energy Harvesting. *J. Am. Chem. Soc.* **134**, 20294–20297 (2012).

151. Kittel C. *Introduction to Solid State Physics, 8th edition, Berkeley. John Wiley & Sons, New York* (1996).

152. Stordeur, M., Ketavong, K. K., Priemuth, A., Sobotta, H. & Riede, V. Optical and Electrical Investigations of n-Type Bi2Se3 Single Crystals. *Phys. status solidi* **169**, 505–514 (1992).

153. Scheele, M. *et al.* ZT enhancement in solution-grown Sb(2-x)BixTe 3 nanoplatelets. *ACS Nano* **4**, 4283–4291 (2010).

154. Yamada, A. *et al.* Effect of band offset on the open circuit voltage of heterojunction CuIn1-xGaxSe2 solar cells. *Appl. Phys. Lett.* **85**, 5607–5609 (2004).

155. Chen, Y. *et al.* The Influence of Conduction Band Offset on CdTe Solar Cells. *J. Electron. Mater.* **47**, 1201–1207 (2018).

156. Javaid, K. *et al.* Band Offset Engineering in ZnSnN2-Based Heterojunction for Low-Cost Solar Cells. *ACS Photonics* **5**, 2094–2099 (2018).

157. Tersoff, J. Theory of semiconductor heterojunctions: The role of quantum dipoles. in 218–221 (Springer, Dordrecht, 1988). doi:10.1007/978-94-009-3073-5_22

158. Liu, H., Keuleyan, S. & Guyot-Sionnest, P. N- and p-type HgTe quantum dot films. *J. Phys. Chem. C* **116**, 1344–1349 (2012).

159. Lan, X. *et al.* Quantum dot solids showing state-resolved band-like transport. *Nat. Mater.* **19**, 323–329 (2020).

160. Itsuno, A. M., Phillips, J. D. & Velicu, S. Design and modeling of HgCdTe nBn detectors. in *Journal of Electronic Materials* **40**, 1624–1629 (Springer, 2011).

161. Williams, G. M. & De Wames, R. E. Numerical simulation of HgCdTe detector characteristics. *J. Electron. Mater.* **24**, 1239–1248 (1995).

162. Jóźwikowski, K. *et al.* The Numerical–Experimental Enhanced Analysis of HOT MCT

Barrier Infrared Detectors. *J. Electron. Mater.* **46**, 5471–5478 (2017).

163. Tang, X., Ackerman, M. M. & Guyot-Sionnest, P. Thermal Imaging with Plasmon Resonance Enhanced HgTe Colloidal Quantum Dot Photovoltaic Devices. *ACS Nano* **12**, 7362–7370 (2018).

164. Tang, X., Ackerman, M. M., Shen, G. & Guyot-Sionnest, P. Towards Infrared Electronic Eyes: Flexible Colloidal Quantum Dot Photovoltaic Detectors Enhanced by Resonant Cavity. *Small* **15**, 1804920 (2019).

165. Keuleyan, S., Kohler, J. & Guyot-Sionnest, P. Photoluminescence of mid-infrared HgTe colloidal quantum dots. *J. Phys. Chem. C* **118**, 2749–2753 (2014).

166. Guyot-Sionnest, P., Wehrenberg, B. & Yu, D. Intraband relaxation in CdSe nanocrystals and the strong influence of the surface ligands. *J. Chem. Phys.* **123**, 074709 (2005).

167. Han, P. & Bester, G. Carrier relaxation in colloidal nanocrystals: Bridging large electronic energy gaps by low-energy vibrations. *Phys. Rev. B - Condens. Matter Mater. Phys.* **91**, 085305 (2015).

168. Kovalenko, M. V., Scheele, M. & Talapinl, D. V. Colloidal nanocrystals with molecular metal chalcogenide surface ligands. *Science (80-.).* **324**, 1417–1420 (2009).

169. Hines, M. A. & Guyot-Sionnest, P. Synthesis and characterization of strongly luminescing ZnS-capped CdSe nanocrystals. *J. Phys. Chem.* **100**, 468–471 (1996).

170. Shen, G. & Guyot-Sionnest, P. HgTe/CdTe and HgSe/CdX (X = S, Se, and Te) Core/Shell Mid-Infrared Quantum Dots. *Chem. Mater.* **31**, 286–293 (2019).

171. Goubet, N. *et al.* Near- to Long-Wave-Infrared Mercury Chalcogenide Nanocrystals from Liquid Mercury. *J. Phys. Chem. C* (2020). doi:10.1021/acs.jpcc.0c01255

172. Deng, Z., Jeong, K. S. & Guyot-Sionnest, P. Colloidal quantum dots intraband photodetectors. *ACS Nano* **8**, 11707–11714 (2014).

173. Melnychuk, C. & Guyot-Sionnest, P. Auger Suppression in n-Type HgSe Colloidal Quantum Dots. *ACS Nano* **13**, 10512–10519 (2019).